Using Model-Based Analysis and Physiology-Informed Machine Learning for Precision Phenotyping in Heart Failure

by

Edith Jones

A dissertation submitted in partial fulfillment
of the requirements for the degree of
Doctor of Philosophy
(Molecular and Integrative Physiology)
in the University of Michigan
2022

Doctoral Committee:

Professor Daniel A. Beard, Chair
Associate Professor Diane C. Fingar
Associate Professor Scott L. Hummel
Professor Daniel E. Michele
Professor Santiago Schnell, University of Notre Dame

Edith Jones

jonesedi@umich.edu

ORCID iD: 0000-0002-4921-7978

Dedication

To my family, friends, past and present mentors to whom without your incredible love, encouragement and support this work would have never come to pass.

"If I have seen further, it is by standing on the shoulders of giants"

- Isaac Newton

Acknowledgements

I owe my deepest gratitude to the many people who helped me make this dissertation research possible. I begin by thanking my mentors Daniel Beard and Brian Carlson. I was incredibly blessed by their patience, care and true joy of conducting science shown every day. I owe the deepest gratitude to my thesis committee for your scientific as well as career insight while trying to figure out next career steps. I am incredibly thankful to every single member of the Beard Lab. Thank you for all the fond memories we created and providing a rich community for me to grow not only as a scientist but as a better human being. I owe many countless hours of instruction and experimental support at the bench to Fran Van Den Bergh. Thank you to my fellow Beard lab graduate students, Rachel and Nicole, for your friendship and all those taco adventures. Thank you to Ben Rendall for your instruction in the scientific process from a peer-to-peer perspective, for sharing openly about your academic journey and for encouraging me to keep going. Thank you to our amazing FCVC Summer Undergraduate Research Fellows, Kiley Hassevoort and Abigail Liebetreu, for your scientific curiosity and incredible hard work. Thanks to you we were able to explore potential clinical applications of the work developed in this thesis.

I would also like to thank the Molecular & Integrative Physiology department with its vibrant and caring community, from administrators to faculty and students. I could not have asked for a better academic home to pursue my PhD. Thank you to three extraordinary women in science, Sue Moenter, Christin Carter-Su and Susan Brooks Herzog, for always taking time to provide unique mentorship to those coming behind you!

Thank you so much to my Grace Ann Arbor family for welcoming me to your church and providing a home away from home. My GradCru family, provided me with so much support and encouragement for engaging with my faith journey while pursuing my PhD. My deepest thanks go to Sandra Jones (a.k.a. mom), Carla Williamson, Carol Jordan, Paula Smith and Amy Kimball, extraordinary women outside of academia, who in different seasons through grad school encouraged and challenged me into greater maturity both with my faith and in engaging with my graduate work.

I owe the deepest gratitude to my mom and dad for all the love and care they poured to my sister and me while growing up. Thank you so much for always encouraging us to keep learning and exploring, and for providing their daughters with an incredible well rounded bilingual education. Thanks to you I was able to engage with my PhD work and write this dissertation in my second language! Thank you so much to my sister Carolina for your words of affirmation and the fearlessness and courage you showed in finishing your degree despite the challenges faced through the COVID-19 pandemic. You inspire and challenge me to care and love those inside and outside my natural pathways. Thank you to my abuelitas Alma and Maria, for being incredibly strong women that have loved your children and grandchildren in an amazing way. Your life brings joy to our lives, and I could not have made it this far without your laughter, food, and prayers (in equal amounts). Thank you to my suegro and suegra, Scott and Julie Kiyabu, for your prayers and support helping with moving logistics as two newlyweds were trying to finish their PhDs, move apartments, figure out career steps for two scientists and move to another state.

Finally, I would like to thank my husband and best friend, Steven. He has been a fundamental pillar of emotional and spiritual support, as well as a great scientific partner. Our discussions about scientific computing and machine learning approaches were instrumental to the

development of this work. I came to the University of Michigan only seeking an academic degree but now I am leaving full of incredible friends and a family. I could ask for no greater gift than this.

Table of Contents

List of Tables

List of Figures

Abstract

A model-based approach was developed to elucidate etiological differences between and within patient groups representing the two dominant heart failure diagnoses: heart failure with reduced (HFrEF) and preserved (HFpEF) ejection fraction. A closed-loop model of the cardiovascular system informed by patient-specific transthoracic echocardiography (TTE) and right heart catheterization (RHC) data was used to identify key parameters representing cardiovascular mechanics and hemodynamics. Model simulations were tuned to match RHC and TTE pressure, volume, and cardiac output measurements in each patient. The underlying physiological model parameters were compared to model-based norms and between HFrEF and HFpEF diagnoses. Our results confirm the main mechanistic parameter driving HFrEF is reduced left ventricular contractility, whereas HFpEF exhibits a more heterogeneous phenotype. To determine subgroups within the HFpEF diagnosis, we conducted a principal component analysis on the optimized parameters, which combined with machine learning techniques including *k*-means and hierarchical clustering methods reveal (i) a group of HFrEF-like HFpEF patients that share characteristics with HFrEF, (ii) a HFpEF group that exhibit classical characteristics of patients with diastolic dysfunction, and (iii) a group of HFpEF patients that share characteristics of both types of dysfunction. These subgroups cannot be distinguished from the clinical data alone. However, reanalyzing the clinical data of each of these newly determined subgroups reveals that elevated systolic and diastolic LV volumes seen in both HFrEF and the HFrEF-like HFpEF may be used to identify this patient population. Similar HFpEF groupings have been identified by other studies using extensive clinical measures (e.g., non-routine echocardiography and heart biopsies)

whereas our study analyzes data from standard clinical procedures, such as TTE and RHC. Hence, our methodology has great translational potential to be broadly accepted in the clinic. These results suggest that physiology-informed model-based analysis of standard clinical data in conjunction with unsupervised machine learning can distinguish subgroups of HFpEF as separate phenotypes. Moreover, this methodology has the potential to retrospectively assess patient selection in past HFpEF clinical studies, aid in the optimization of prospective HFpEF subgroup selection for future clinical trials and elucidate patient-specific treatment strategies for HFpEF.

Chapter 1 Introduction

1.1 Heart Failure: Definitions and Diagnoses

The heart pumps blood to meet the metabolic demands of the body by circulating blood through the lungs and the systemic periphery. Oxygen delivered via the blood is a crucial substrate for oxidative ATP synthesis in the tissues of the body. The heart has two main pumping chambers, the left, and right ventricles. Blood ejected from the right ventricle (RV) is delivered to the pulmonary circulation where it unloads carbon dioxide and takes up oxygen. Oxygenated blood returned from the lung to the heart is ejected from the left ventricle (LV) to the systemic circulation. Maximal cardiac output (CO)—the maximum rate of blood pumping—occurs at maximal voluntary exercise (maximum whole-body oxygen consumption, VO_2max). Under physiologic conditions, the recruitable reserves of CO and cardiac power (a measure that integrates pressure and flow in the cardiovascular system, and thus, another measure of cardiac pumping) are close to four to five times the resting basal level. Heart failure (HF) is suspected when the heart is unable to pump to match physiologic CO and recruitable cardiac power reserves. The most classically accepted definition of HF was developed by Lily et al. stating that:

"Heart failure is present when the heart is unable to pump blood forward at a sufficient rate to meet the metabolic demands of the body or is able to do so only if cardiac filling pressures are abnormally high (Lilly LS, 2016)."

This classical understanding of HF has focused on cardiac dysfunction alone. Yet, definitions of HF focusing on the whole-body impacts of the disease are beginning to emerge. For

example, a recent definition emphasizes diminished reserve cardiac power and impaired exercise capacity as the defining features of HF(Beard *et al.*, 2021).

1.1.1 Causes of HF

The loss of cardiac pumping function in HF is associated with cardiac structural adaptations to a precipitating cause. Cardiac function may be impaired due to acute causes (i.e., structural damage from cardiopulmonary bypass surgery, infection) or chronic cardiovascular diseases (i.e., structural adaptions due to hypertension or coronary artery disease (CAD)). For example, in the case of CAD, cholesterol plaque formation in the coronary artery, disrupts proper cardiac oxygen delivery, compromising bioenergetics and eventually leading to cardiac dysfunction (Shao *et al.*, 2020). Cardiac infarction, one of the end-stage manifestations of CAD leads to a high incidence of HF(Murphy *et al.*, 2020). Diseases causing cardiac structural remodeling such as dilated cardiomyopathy (DCM) and hypertrophic cardiomyopathy (HCM) can be triggered by compensating adaptations but can also be due to inherited genetic mutations (i.e., familial HCM and DCM) (Marian & Braunwald, 2017; Orphanou *et al.*, 2022). Challenging hormonal states such as hyperthyroidism and pregnancy, can increase CO and cardiac power demand and likewise trigger the development of HF(Bright *et al.*, 2021). While helpful at cardiac disease onset or in states of increased CO and cardiac power demand, in the long-term cardiac structural adaptive responses have negative consequences on the cardiac, pulmonary, and systemic circulation.

1.1.2 Compensatory Physiological Changes to Maintain CO in HF

Whether an acute or chronic event leads to HF, the classical understanding is that patients with HF have a decreased CO (Campia *et al.*, 2010). CO can be influenced by stroke volume (SV), the amount of blood ejected during the cardiac cycle, and heart rate (HR), the heartbeat frequency.

In summary, all cardiovascular compensatory adaptations (i.e., changes in vascular function, blood volume, and neurohumoral status) aim to increase HR and SV to maintain CO. In the long term, however, these adaptive mechanisms can backfire to produce the general signs and symptoms associated with HF (i.e., elevated systemic and pulmonary pressures that often lead to peripheral and pulmonary congestion).

Compensatory Sympathetic Cardiac Activation

Norepinephrine acts on cardiomyocyte β1-adrenergic receptors, thereby increasing HR and cardiac inotropy (contractility), resulting in sympathetic cardiac stimulation. Chronic sympathetic overstimulation of the heart exacerbates HF and has negative effects such as ventricular hypertrophy, enhanced arrhythmias, and activation of molecular/biochemical mechanisms leading to dysfunction (Richard E. Klabunde, 2015).

Compensatory Sympathetic Systemic Activation

At the systemic level, HF leads to compensatory activation of the sympathetic nervous system within the autonomic nervous system (ANS) activation of the renin-angiotensin system and increases vasopressin and atrial natriuretic peptide (ANP) release. α1-adrenergic receptors present in arterial and venous vessels are activated by the norepinephrine released from the sympathetic nerves innervating them increasing arterial/venous vasoconstriction (Pepper & Lee, 1999). The vasoconstriction helps maintain arterial pressure and increase venous pressure under conditions of low CO in HF. However, because aortic pressure increases in response to vasoconstriction, the 'load' the LV must push against to eject blood into the systemic circulation (afterload) also increases. Thus, over-activation of the sympathetic nervous system affecting the vasculature may have overall negative effects on the pumping function of an already failing heart. Because activation of the sympathetic nervous system also leads to vasoconstriction of smaller

arterioles, these compensatory mechanisms can negatively impact exercise by limiting muscle perfusion. Venous vasoconstriction causes more fluid to flow out of the venous compartment into efficient circulation, thereby increasing SV and cardiac preload (initial stretching of cardiomyocytes before contraction), however an increase in venous pressures can also lead to peripheral edema (Fudim et al., 2017). Increased sympathetic stimulation on renal β-adrenergic receptors stimulate renin release, which is one of the clinical HF biomarkers (Heidenreich *et al.*, 2022). Circulating renin on its turn stimulates angiotensin II production and aldosterone release. The overall effect of these circulating hormones is to increase blood volume by activating renal mechanisms of sodium and water retention, thus helping increase venous return to the heart and increase SV(Pepper & Lee, 1999). Angiotensin II also leads to vasoconstriction and increases systemic vascular resistance (SVR). These hormones can also lead to cardiac remodeling that occurs in HF (Richard E. Klabunde, 2015).

Maximizing venous return takes advantage of the intrinsic mechanical properties of the heart described by the Frank-Starling mechanism in which preload—the force that stretches the heart prior to contraction— is proportional ventricular filling. Increased ventricular filling leads to an increase in active tension and shortening developed by the muscle fibers in the cardiomyocytes, causing higher SV. A compensatory response to the high preload present in the atria and ventricles during HF is increased natriuretic peptide (NP) release. The heart and brain release NPs to lower arterial pressure, these act by decreasing blood volume and systemic vascular resistance. Atrial and ventricular dilation stimulates NP release. Neurohumoral stimuli also stimulate NP release in response to HF. There are two NPs: Atrial Natriuretic Peptide (ANP) and Brain Natriuretic Peptide (BNP). Atrial myocytes synthesize and release ANP. Other factors such as angiotensin II, endothelin, and sympathetic stimulation (activating β-adrenoreceptors)

precipitate ANP release. The brain and ventricular myocytes synthesize BNP's pre hormone form Pro-NPP, and its release is triggered by physiologic factors similar to ANP. Pro-NPP, is cleaved to BNP and N-terminal-proB-type natriuretic peptide (NT-proBNP). Both BNP and NT-proBNP are sensitive diagnostic markers for HF in the clinic (Heidenreich *et al.*, 2022).

1.1.3 HF Classification

The classical understanding of HF is that CO is decreased due to cardiac systolic or diastolic dysfunction. Ejection Fraction (EF) is the volumetric fraction of blood ejected from a chamber in the heart with each heartbeat. EF is calculated by dividing SV by EDV. For a healthy individual at rest, SV is ~70 mL and EF is ~65% in the LV (although volumes should be similar for the right ventricle (RV)). LVEF is a measure of the effectiveness of the heart's pumping action into the systemic circulation, and as early as the 1930s it was proposed as a useful metric to assess cardiac function (Nylin G, 1933). LVEF is now considered the most important metric in the classification of patients with HF, and most clinical trials select patients based on LVEF as their primary criterion (Yusuf *et al.*, 2003; Hoendermis *et al.*, 2015; Palau *et al.*, 2020; Nassif *et al.*, 2021). Clinicians have classified HF patients into two categories based on whether their LVEF is below or above 50% (Heidenreich *et al.*, 2022). If a patient's EF is ≤50% they are diagnosed with heart failure with reduced ejection fraction (HFrEF). In HFrEF, the reduction in EF is because of inefficient systolic contraction leading to an increased EDV and ESV. Thus, HFrEF patients are often described as having 'systolic' HF (Murphy *et al.*, 2020). If a patient has HF symptoms but their EF is ≥50%, they are diagnosed with heart failure with preserved ejection fraction (HFpEF). In HFpEF, EF is preserved out of the proportionally small ESV and EDV (although this is not always the case, some HFpEF patients can have higher than normal ventricular volumes). The classical assumption is these patients have low small ventricular volumes due to 'diastolic' HF

(Dunlay *et al.*, 2017). Exercise intolerance, impairment of recruitable oxygen reserves, and cardiac power are measurements that consider other contributing peripheral factors and are moving away from looking at the heart alone as the sole cause of HF (Beard *et al.*, 2021). Unlike EF, which focuses only on the systolic function of the heart, cardiac power aims to combine information from the afterload and chronotropic state of a patient by considering arterial pressure, flow, and HR, thus expressing the required energy transfer from the LV to the aorta (Fincke *et al.*, 2004). Although some of these measurements are beginning to make their way as biomarkers that correlate with the severity of HF and mortality rate, the current HF diagnosis remains based on EF.

1.2 Heart Failure with Reduced Ejection Fraction

1.2.1 Etiology and Pathophysiology

The burden of HF has increased worldwide, but particularly in the countries where the increased quality of life and expectancy has led to a large aging population struggling with cardiovascular disease as well as metabolic comorbidities (i.e., obesity, diabetes, CAD) that may contribute to the development of HF (Heidenreich *et al.*, 2022). It is now estimated that over 11 million people worldwide are diagnosed with HF with reduced ejection fraction (HFrEF) (Murphy *et al.*, 2020). HFrEF is characterized by progressive LV dilation. Thus, the classical understanding of HFrEF, is that patients in this category have 'systolic' HF, due to a loss of ventricular contractility that reduces their ability to pump blood to the systemic circulation during systole (Pinilla-Vera *et al.*, 2019). Because about half of HFrEF cases are of ischemic etiology, newly diagnosed patients need an evaluation for CAD, as patients with CAD are prone to myocardial infarction (which would damage cardiac capacity even more). Typical symptoms of HFrEF include difficulty breathing, fatigue, and ankle swelling (Murphy *et al.*, 2020).

In HFrEF, cardiac contractility of an intrinsically weak heart can be maximized by greater ventricular filling and the Frank-Starling mechanism. This increased filling of the ventricles may in part lead to the ventricular dilation observed in HFrEF. In HFrEF patients, the neurohumoral response to low CO, triggers a signaling cascade leading to increased venous and arterial vasoconstriction. Although helping to increase ventricular filling, abnormally high venous pressure will also lead to systemic edema and contribute to swelling of the extremities, particularly in the legs of HFrEF patients. Likewise, the renin-angiotensin system activation will lead to fluid retention and volume overload. In the beginning mechanisms increasing mean arterial pressure as well as venous constriction will help with preload. However as arterial pressure increases, the increased afterload can negatively impact the function of a heart already struggling with systolic dysfunction. The inability to push blood out from the LV to the systemic circulation will lead to a high ESV. High LV volumes and pressures will eventually lead to high volumes and pressure in the left atria (LA). Because of its relationship with pulmonary circulation, high pressure in the LA can lead to complications such as pulmonary edema and pulmonary hypertension. Ventricular and atrial distention will lead to the release of NPs which paradoxically starts to lower blood volume and ventricular filling counteracting some of these initial compensatory mechanisms. Overall, HFrEF is characterized by a heart dysfunction that typically leads to some initial compensatory adaptations, but these compensatory adaptations when overactivated or chronically stimulated lead to worsened cardiac function. For these same reasons effective treatments and therapies for HFrEF have been challenging.

1.2.2 Diagnosis of HFrEF

To diagnose HFrEF accurately, initial testing involves the measurement of echocardiography, NPs, electrocardiography, and chest x-ray. As mentioned earlier, HFrEF may

be associated with ischemic etiologies such as CAD. To test for the formation of obstructive plaque, clinicians may prescribe invasive coronary angiography. Likewise, for patients with a low probability of ischemic disease, a non-invasive test using computed tomography can be used instead (Murphy *et al.*, 2020).

Chest-X ray

When clinicians suspect HF, patients undergo chest X-rays. Clinicians will use it to look for routine radiographic features of HF, such as an enlarged heart. The presence of septal lines may indicate pulmonary venous congestion. Air gaps, opacities, and pleural effusions are hallmarks of pulmonary effusion and may suggest pulmonary edema (Chait *et al.*, 1972).

Echocardiography

Transthoracic echocardiography (TTE) is a non-invasive and widely available imaging technique able to visualize cardiac structures such as the ventricles and atria (Lang RM *et al.*, 2016). TTE images are particularly important for HF diagnosis as they are used to quantify LV volumes in systole and diastole and estimate a patient's EF, hence allowing the clinician to confirm the HFrEF diagnosis of an LVEF of 50% or less. The LV volumes are typically measured as either (i) a single diameter across the LV just below the mitral valve leaflet tips (Teichholz *et al.*, 1976) or (ii) tracings of the LV from apical two- and four-chamber views. Volumes derived from the two- and four-chamber views are calculated by the Method of Discs (MOD), also known as Simpson's Method, which is now the preferred method for the estimation of LV volumes. From TTE measurements, clinicians may obtain additional information, such as CO based on the calculated SV andthe patient's HR, the left ventricular out tract flow velocity time integral (LVOT VTI), and the cross-sectional aortic valve area for each patient (Lang RM *et al.*, 2016).

Cardiac Magnetic Resonance

Although not widely used in every patient, an excellent non-invasive method to visualize left and right ventricular volumes is cardiac magnetic resonance (CMR). In addition to assessing cardiac morphology, CMR can provide rich information on ventricular function, myocardial perfusion, tissue characteristics, flow quantification, and CAD (Russo *et al.*, 2020). A modification of CMR, Phosphorus-31 MRS (31P-MRS), is an imaging modality capable of measuring high-energy phosphate metabolism and can be used to characterize in vivo myocardial energy status in HF patients (Bakermans *et al.*, 2017).

Right Heart Catheterization

A right heart catheterization (RHC) is an invasive procedure in which a Swan-Ganz catheter is inserted through the jugular vein and measures the pressure at the tip of the catheter as it is advanced into the pulmonary artery, allowing for direct measurement of pressures in the heart. An RHC may be indicated in patients with worsening HF symptoms without a clear cause, before cardiac transplantation or insertion of a Left Ventricular Assist Device, and in post-infarction mechanical complications like a ventricular aneurysm. Specifically, RHC measures pressures in the right atria (RA), right ventricle (RV), pulmonary artery (PA), and the pulmonary capillary wedge pressure (PCWP). Normal RA pressures range between 0-7 mmHg, they are an indicator of RV volume status and preload. RA pressures are elevated when there is a disruption in forwarding cardiac flow or an increase in intravascular volume, such as in RV and valvular disease, pulmonary hypertension, HF, and cardiomyopathies. Normal RV pressures range from 15-25 mmHg and 3-12 mmHg in systole and diastole respectively. Because RV pressures are surrogates for PA pressure, high RV pressures are often elevated with diseases that elevate PA pressures.

Normal PA pressures are often reported in systole as 15-25 mmHg, 8-15 mmHg diastole, and mean values of 10-19 mmHg. PA pressures are elevated by acute conditions such as pulmonary edema and hypoxemia-induced pulmonary vasoconstriction, as well as in chronic diseases such as pulmonary hypertension (mean PAP > 20 mm Hg is an important diagnostic criterion for this disease). Normal PCWP is between 4-12 mmHg, is an important surrogate measurement for LA pressure and LV end-diastolic pressure (preload). PCWP increases in proportion to elevated preload when HF, cardiomyopathies, or valve disorders are present (Vanderbilt University Medical Center, 2020).

In addition to pressure information, indirect RHC calculations include CO, pulmonary vascular resistance (PVR), and cardiac power. CO is estimated by using the Fick or thermodilution methods. The Fick method measures venous and arterial O_2 saturation and often presumes a given whole body oxygen consumption (VO_2) based on weight, height, and sex. The accuracy of the Fick method hinges on correctly estimating VO_2, and it has been determined that it can vary by as much as 25% when compared to a direct measurement of $\dot{V}O_2$ (Narang *et al.*, 2014). During RHC, the thermodilution technique estimates CO by measuring the dispersion of a bolus injection of cold saline at the proximal end of the catheter and with a temperature sensor at the distal end of the catheter. PVR is an indicator of how much the pulmonary circulation "resists" CO, and it can be calculated from RHC measurements by subtracting the pulmonary arterial wedge pressure (PAWP) or LA pressure from the mean PAP (Chemla et al., 2015). Cardiac power is a novel hemodynamic measure of cardiac pumping incorporating pressure and flow and is calculated by multiplying the CO and mean arterial blood pressure. In recent studies, cardiac power was shown to be instrumental in the diagnosis of cardiogenic shock and chronic heart HF (Fincke *et al.*, 2004).

Laboratory Evaluation

Several laboratory evaluations are recommended for patients suspected of HF (Heidenreich *et al.*, 2022).Complete blood count and iron studies are amongst these evaluations to rule out anemia as a possible cause for symptoms (i.e., fatigue) (Said Hajouli & Dipesh Ludhwani, 2022). Urinalysis, serum electrolytes, blood urea, nitrogen, and serum creatinine are all indicators of kidney function, which as mentioned earlier is altered and often compromised during HF. Electrolytes and kidney function should be monitored after diagnosis because some of the therapeutics can cause additional abnormalities (Heidenreich *et al.*, 2022). Glucose, fasting lipid profile, liver function tests, and thyroid-stimulating hormone are also recommended to provide important information on patients' comorbidities (i.e., diabetes), suitability for and adverse effects of treatments, or potential causes of HF (Heidenreich *et al.*, 2022). Assays for BNP and NT-proBNP are frequently used to establish the presence and severity of HF and are equally reliable for diagnostic purposes (Taylor & Hobbs, 2010). NT-proBNP, <300 pg/mL and BNP <50 pg/mL values are used to rule out acute HF, while BNP <35 pg/mL or NT-proBNP <125 pg/mL values are used to rule out chronic HF in HFrEF patients (Murphy *et al.*, 2020).

1.2.3 Evidence-based Treatment of HFrEF

A number of drug- and device-based therapies have improved outcomes in HFrEF (Yancy *et al.*, 2006; Pinilla-Vera *et al.*, 2019). Pharmacological treatment of HFrEF is primarily aimed at inhibiting the chronic overactivation of compensatory pathways present in this type of HF that were described earlier, such as renin-angiotensin-aldosterone and the sympathetic nervous system (Murphy *et al.*, 2020).

β-Blockers: Bisoprolol, Metoprolol succinate, Carvedilol

As mentioned before in HF to sustain CO, the sympathetic nervous system releases a large amount of epinephrine and norepinephrine. When actuated by these hormones, β1-receptors trigger a signaling cascade by which phosphorylation of proteins involved in excitation-contraction takes place, the result in greater contractility, HR, diastolic distensibility, and relaxation. To adjust for this sympathetic hyperactivation response, β1-receptor density declines by 60% in cardiac tissue. Even though β1 receptors are downregulated in the failing heart, cardiomyocytes are still under the influence of toxic hyper-adrenergic stimulation. Drugs that block the action of norepinephrine and epinephrine on beta receptors are known as β-blockers. Several β-blockers for treatment of HFrEF are currently FDA approved including Bisoprolol, Metoprolol succinate, and Carvedilol (Anon, 1999*a*, Anon, 1999*b*; Packer *et al.*, 2001). β-blockers inhibit the hyper sympathetic state further, providing both a cardioprotective response and leading to an increased expression of β1 receptors. Moreover, βAR blockers have beneficial hemodynamic effects, decreasing cardiac work, afterload, and oxygen consumption. Multiple random controlled trials of β-blockers in HFrEF patients have revealed reduced hospital admissions, improved quality of life, slowed disease progression, and reduced mortality (Pinilla-Vera *et al.*, 2019).

Angiotensin-converting enzyme (ACE) inhibitors: Captopril, Ramipril, Enalapril, Lisinopril

As mentioned before the upregulation of the renin-angiotensin-aldosterone system results in not only fluid retention and peripheral arterial vasoconstriction but also adverse remodeling as seen in cardiomyocyte hypertrophy and interstitial fibrosis (Richard E. Klabunde, 2015). ACE inhibitors such as Captopril, Ramipril, Enalapril and Lisinopril are some of the main treatments for HFrEF (Murphy *et al.*, 2020). They act by blocking the conversion of angiotensin I to angiotensin II. This action prevents vasoconstriction and causes relaxation of the vasculature; thus,

they lower peripheral resistance and reduce the afterload on the failing myocardium(Pinilla-Vera *et al.*, 2019).

Angiotensin II Receptor Blockers (*ARBs): Candesartan, Losartan, Valsartan*

ARBs, like ACE inhibitors, reduce the effects of the overactive renin-angiotensin-aldosterone system in HF. ARBs such as Candesartan, Losartan and Valsartan were developed to overcome the deficiencies of ACE inhibitors. When ACE is inhibited, compensatory increases in renin and angiotensin I levels often overcomes the ACE inhibitory effect. Furthermore, accumulation of other ACE substrates such as bradykinin and other tachykinins, and circulation of angiotensin II not produced by ACE also reduce the effectiveness of ACE inhibitors in some patients (Barreras & Gurk-Turner, 2003).

Angiotensin receptor–neprilysin inhibitor: Sacubitril/Valsartan

Some drugs combinations target multiple overactive compensatory pathways in HFrEF. Sacubritil/Valsartan is a combination neprilysin inhibitor and angiotensin II receptor blocker. Valsartan counters the hypertensive effect of the hyperactive renin-angiotensin-aldosterone system as described above. Neprilysin is a neutral endopeptidase that degrades ANP and BNP. As mentioned earlier in this chapter NPs are responsible for regulating cardiovascular and renal homeostasis in response to atrial and ventricular distension. Because Neprilysin cleaves circulating NPs, its inhibition allows the anti-hypertensive effects of ANP and BNP to last longer. Thus, the combined drug counters the hypertensive response in HF through two independent mechanisms.

Mineralocorticoid receptor antagonists (MRA): Eplerenone, Spironolactone

MRAs are a class of diuretics that promote sodium and water excretion as well as potassium retention by competitively inhibiting mineralocorticoid receptors in the distal convoluted tubule (Sica, 2005). MRAs are primarily used to treat fluid buildup in HFrEF. Because of concerns of

adverse events such as hypotension, MRAs are often underused in treating treat HFrEF patients (Serenelli *et al.*, 2020).

Vasodilators: Hydralazine, Isosorbide dinitrate, Fixed-dose hydralazine/Isosorbide dinitrate

Combination therapy with nitrates and hydralazine in chronic HF was first developed to achieve the hemodynamic benefits of both preload and afterload reduction. Hypothesized mechanisms include stimulation of nitric oxide signaling in vascular smooth muscles that leads to vasodilation and reduction of oxidative stress by hydralazine; although these hypotheses have not been fully elucidated(Pinilla-Vera *et al.*, 2019).

Heart Rate Modulator: Ivabradine

An increase in HR caused by hyper sympathetic stimulation is one of the hallmarks of HF. Hence, reducing the increased HR has been considered as a therapeutic strategy. HR is modulated first in the pacemaker of the heart, the sinoatrial node, before the signal is transmitted to the atrioventricular node and the Purkinje fibers. Ivabridine selectively blocks the funny channel (If) current which is, responsible for the depolarization required to create the pacemaker activity in the sinoatrial node. Treatment with Ivabradine results in a slower HR without affecting blood pressure, myocardial contractility, or conduction (Pinilla-Vera *et al.*, 2019).

1.3 Heart Failure with Preserved Ejection Fraction

1.3.1 Etiology and Pathophysiology

HFpEF now represents more than half of HF cases, and its incidence is increasing with an aging population, and a high prevalence of associated risk factors (e.g., obesity, systemic hypertension, CAD, and diabetes) (Yancy *et al.*, 2006; Owan *et al.*, 2006; Hummel *et al.*, 2009; Little & Zile, 2012). Patients with HFpEF suffer poor quality of life and long-term outcomes. The classic HFpEF paradigm implicates LV diastolic dysfunction as the main driver of exercise

intolerance and HF progression (Zile *et al.*, 2004). Increased large arterial stiffness (Tartière-Kesri *et al.*, 2012), reduced ventricular systolic reserve (Shah *et al.*, 2015), chronotropic incompetence (insufficient heart rate for the degree of exercise) (Borlaug *et al.*, 2006, 2010), peripheral and coronary microcirculatory dysfunction (Maréchaux *et al.*, 2016; Lee *et al.*, 2016; Franssen *et al.*, 2016; Taqueti *et al.*, 2018) and venous volume redistribution (Fudim et al., 2017) also contribute to HFpEF to varying degrees. This heterogeneity underlies the failure of multiple treatment strategies to demonstrate sustained benefit in HFpEF. The scientific consensus is that improved phenotyping is needed to effectively target therapies and improve outcomes in this complex syndrome (Senni et al., 2014; Shah et al., 2016, 2020).

1.3.2 Diagnosis of HFpEF

Chest-X ray

As mentioned earlier, when HF is suspected, clinicians recommend intensive evaluation of the patient to determine the type of HF present and any comorbidities contributing to the disease. A chest X-ray showing elevation and lateral displacement of the LV border may indicate enlargement of the ventricular walls, such as a hypertrophic state associated with HFpEF. Such X-rays may look different from HFrEF hearts, in which LV systolic dysfunction ultimately results in increased volume and enlargement of all four cardiac chambers (Chait *et al.*, 1972).

M-mode and 2D Echocardiography

As mentioned earlier, TTE is the current standard for assessing LVEF, which is the main discriminator in differentiating patients with HFrEF and HFpEF. Therefore, all patients with features of HF and an LVEF equal to or greater than 50% are diagnosed with HFpEF.

Cardiac Magnetic Resonance

As stated, before while most of the research and patient diagnosis for HF has focused on assessing LV dysfunction as the dominant cause of HF, there is increasing recognition that the pulmonary circulation and RV may be of equal or even greater importance during exercise for HF patients. Thus, to direct patient-specific therapies addressing potential heterogeneity in HFpEF, there is a need for an imaging technique capable of accurately assessing both cardiac ventricles at rest and during exercise such as CMR (Russo *et al.*, 2020). Myocardial and interstitial fibrosis in patients with HFpEF can be assessed in vivo by means of T1 mapping and extracellular volume computation in CMR. These tools may be of clinical importance as they are beginning to be used as quantifiable markers of the extent and severity of diffuse interstitial fibrosis, which is believed to be a major contributor the impairment of cardiac relaxation and stiffness in HFpEF (Chamsi-Pasha *et al.*, 2020).

Right Heart Catheterization

HFpEF is classically characterized by diastolic dysfunction caused by impaired relaxation and stiffened myocardium. These structural changes are believed to be caused by increased arterial stiffness, which creates a greater afterload and places a greater burden on the LV. High pressures on the left side of the heart, particularly the LA can challenge the lung vasculature with pulmonary edema and hypertension. Therefore, RHC can provide rich information to assess whether patients have increased RV and PCWP stress, which may indicate the development of this remodeling (Guazzi, 2014). Patients with HFpEF may appear to maintain normal pressure at rest, however, individuals may exhibit impaired hemodynamics during exercise. Patients are generally considered to have HFpEF if they have PAP $\geq$ 25 mmHg and PCWP $\geq$ 15 mmHg at rest or PCWP$\geq$ 25 mmHg with exercise (Hoendermis *et al.*, 2015; Borlaug *et al.*, 2022).

Laboratory Evaluation

The same laboratory tests recommended for patients with HFrEF are also recommended for patients with HFpEF (i.e., blood counts, renal function, metabolic panel). In the United States, more than 80% of patients with HFpEF are overweight or obese. Because of mechanisms not fully understood, NP levels are much lower in obese than nonobese patients. Thus, for many HFpEF patients, their NP levels are below the standard diagnostic cut-off level for HF (Kitzman & Lam, 2017).

1.3.3 Evidence-based Treatment of HFpEF

Despite this large individual and public health burden, HFpEF lacks a framework for evidence-based pharmacotherapy (Yancy *et al.*, 2013). Long-term management of HFpEF focuses on (i) the treatment of any existing comorbidities, (ii) therapeutics that decrease LV diastolic pressures, and (iii) general symptom reduction. Several clinical trials in large cohorts of HFpEF patients have failed to demonstrate consistent benefits. The drugs used include Sildenafil (Guazzi *et al.*, 2011; Borlaug *et al.*, 2015; Hoendermis *et al.*, 2015; Liu *et al.*, 2017), Sacubitril/Valsartan (Solomon *et al.*, 2019), Losartan (Wachtell *et al.*, 2010), Candesartan (Yusuf *et al.*, 2003), Spironolactone (Edelmann *et al.*, 2013; Cohen *et al.*, 2020), and Isosorbide mononitrate (Redfield *et al.*, 2015). It has been suggested that selecting the correct HFpEF cohort is an important factor in treatment success (Borlaug *et al.*, 2015), but the wide range of HFpEF phenotypes at the mechanistic cardiovascular system level makes selecting these cohorts from upper-level clinical data difficult. Because HFpEF is a catch-all category for HF patients based mainly on EF estimates, the inability to have a standard treatment for these patients may be an indicator of the physiologic heterogeneity underlying HFpEF. Hence, identifying subgroups of HFpEF patients with similar cardiovascular etiologies is a crucial task required to target appropriate therapies for these patients.

1.4 Precision Phenotyping in HFpEF

1.4.1 Attempts at Finding HFpEF Subgroups Using Clinical Data and Machine Learning

Recent studies have used clinical outcomes to identify subgroups of patients diagnosed with HFpEF including quantitative echocardiography, plasma protein profiling, and RNA sequencing combined with unsupervised machine learning (ML) techniques (Kao *et al.*, 2015; Shah, 2019; Cohen *et al.*, 2020; Hahn *et al.*, 2021).

Kao et al. identified six HFpEF subgroups with significant differences in event-free survival by using latent class clustering analysis (a type of unsupervised ML) on eleven clinical features of HFpEF patients (Kao *et al.*, 2015). The six HFpEF subgroups identified by Kao et al. consisted of patients with a median age between 65-75 years and hinted at some sex-driven differences between the phenotypes with some of the subgroups consisting of either mostly men or women (Kao *et al.*, 2015). For example, subgroups Kao-I and Kao-V consist of male patients only. The main difference between the two is that Kao-I patients had higher alcohol use, renal dysfunction, and valvular disease while Kao-V patients show lower BMI, excess AF, and CAD when compared to other groups. Groups Kao- II, IV, and VI consist of mostly women. Kao-IV consists of female patients who have average rates of DM but show markers of metabolic comorbidities such as hyperlipidemia, obesity, as well as renal insufficiency. Kao-II and Kao-VI are two equally female-dominated subgroups. Both subgroups are characterized by renal dysfunction, valvular disease, and anemia. The main difference between them is that Kao-II patients have low rates of AF and Kao-VI patients are elderly women having low BMI and high rates of AF. Finally, Kao-III is a subgroup of heterogeneous sex with high rates of metabolic comorbidities, also displaying CAD, anemia, and worse renal function than other subgroups. Both Kao-III and Kao-VI subgroups had the worst levels of event-free survival when compared to other

groups (Kao *et al.*, 2015). Although no differences in the subgroups were found between the median baseline LVEF and the systemic blood pressure, the NT-proBNP median values ranged from 143 pg/mL (Kao-II) to 950 pg/mL (Kao-VI) (Kao *et al.*, 2015). The fact that the baseline LVEF was similar among all these diverse groups could be interpreted as an indicator that although helpful to diagnose HFrEF, LVEF is not very useful in diagnosing subgroups of HFpEF. While differences in clinical outcomes along with unsupervised ML were used by Kao et al. to identify subgroups of HFpEF, these outcomes are vaguely described as obese patients with diabetes or older individuals with a high prevalence of atrial fibrillation. Moreover, there were no detailed echocardiographic or biomarker data available in their subgroup descriptions (only LVEF and n-Terminal B-type natriuretic peptide) (Kao *et al.*, 2015).

In a second study, Shah et al. utilized quantitative echocardiography phenotyping with an unsupervised ML to identify three HFpEF subgroups with differing clinical and echocardiographic characteristics and outcomes (Shah et al., 2019): a group with natriuretic peptide deficiency syndrome; a group with extreme cardiometabolic syndrome; a group with right ventricular cardio-abdominal-renal syndrome.

A third study used plasma protein analysis combined with latent class clustering to identify three clinical phenotypes of HFpEF characterized by distinct echocardiographic parameters and large arterial stiffness (Cohen et al., 2020). The first group showed LV enlargement that was not surprisingly characterized by low LV wall thickness compared to other groups. It likewise had the lowest values of resistive and pulsatile arterial load as calculated by the systemic vascular resistance and total arterial compliance from clinical records. This group also displayed the lowest level of arterial stiffness as calculated by the carotid-femoral pulse wave velocity. A second group had a distinct pattern of clinical features characterized by a small LV with decreased LV mass,

enlarged left atria, and the highest resistive and pulsatile load, as well as increased arterial stiffness when compared to the other two groups. A third group showed LV hypertrophy with increased wall thickness and mass along with low resistance arteries but high pulsatile arterial load.

A fourth study analyzed RNA sequencing of RV septal endocardial biopsies on control, HFrEF, and HFpEF patients through unsupervised ML and identified three HFpEF transcriptome subgroups with distinctive pathways and clinical correlations (Hahn *et al.*, 2021). The first HFpEF transcriptome subgroup showed clustering of transcriptome changes close to HFrEF, the largest LV volumes, and showed the worst clinical outcomes combined with metabolic dysfunction. The second HFpEF transcriptome subgroup had a smaller heart and inflammatory and stromal features. Interestingly all the patients in this group were female and perhaps not surprising had the smallest heart size of all three groups. The third HFpEF transcriptome subgroup had a heterogeneous phenotype including pronounced HF symptoms and smaller hearts, but lower NT-proBNP levels.

1.4.2 Missing Link: Cardiovascular Hemodynamics, its Relationship With the Pulmonary and Systemic Vasculature, and the Uniqueness of each Patient within a Group

These studies show novel classifications of HFpEF subgroups based on clinical outcomes (Kao *et al.*, 2015), detailed clinical, laboratory, electrocardiogram (ECG), and echocardiographic data, phenotyping (S. J. Shah, 2019), plasma biomarker profiling (Cohen *et al.*, 2020) and transcriptomic analysis of endomyocardial biopsy obtained through RHC (Hahn *et al.*, 2021). Each of the studies point out clinical markers that may describe this novel HFpEF classifications (i.e., NT-proBNP marker, inflammatory signal differences between groups). However, the nature of cardiovascular hemodynamics, its relationship with the pulmonary and systemic vasculature, and the uniqueness of each patient within a group have not been addressed. While TTE and RHC provide detailed ventricular volume and pressure data for individual patients, the challenge of

integrating these measurements into a single representation of a patient's cardiovascular state is only made qualitatively in the clinic. One way to quantitatively reconcile what these clinical datasets describe is with a closed-loop computational model of the cardiovascular system which through modeling can derive quantitative estimates of the hemodynamics of the right and left sides of the heart and the systemic and pulmonary circulation. To combine these two sets of data, we must take into consideration that (i) the two datasets are not obtained simultaneously, (ii) they may include a combination of data points taken at specific instances, and (iii) time course data are often not available.

1.4.3 Attempts at Using Mathematical Models to Integrate Cardiovascular Hemodynamics in HFpEF

Recognizing that the characterization of HF patients using only LVEF is questionable, and that more mechanistically driven approaches are needed to understand HF, Wang et al. attempted to reconcile patient hemodynamics derived from CMR and catheter pressure measurements using a patient-specific finite element model of the LV myocardial wall (Wang *et al.*, 2018). Using this tool, they estimated LV diastolic myocardial stiffness and stress. Because HFpEF is classically thought to be caused by diastolic dysfunction, they hypothesized that LV diastolic myocardial stiffness and stress estimation would allow better characterization of HFpEF patients by producing more specific information about myocardial mechanical behavior than global chamber indices traditionally obtained from TTE in the clinic. Using modeling they estimated a wide range of diastolic myocardial stiffness across the HF patient groups. Likewise, myocardial stiffness was larger in the HFpEF groups compared to the control subjects (Wang *et al.*, 2018).

Acknowledging that estimation of subject-specific myocardial stiffness and contractility is difficult in current clinical practice, Rumindo et al. obtained stiffness and contractility indices

using a personalized inverse finite element modeling approach from standard CMR acquisitions. Their estimations were validated against relevant clinical metrics extracted from CMR data such as circumferential strain, wall thickness, and fractional thickening. Although this research was performed on healthy humans, their goal was that these estimates could be used as a reference when evaluating disease (Rumindo *et al.*, 2020).

In a later study, Wang et al. used model simulations that reproduced ECGs and mechanical phenotypes in healthy individuals and individuals at three distinct phases of ischemic cardiac events (which can lead to the development of HF). Using a sensitivity analysis, they calibrated their model's mechanical parameters "to achieve physiological peak pressure and EF" replicating the pathophysiology of these patients (Wang *et al.*, 2021). This study showed that subendocardial infarct caused very little disturbance to either the ECG or the pressure-volume characteristics of three post-ischemic states, highlighting the limitation of ECG and LVEF to reflect the full picture of the disease and the different stages of disease progression (Wang *et al.*, 2021). Another group used a computational model to integrate ventricular electromechanics and sensitivity analysis to test which parameters influence the biomechanical markers of HF including EF, end-systolic pressure, longitudinal fraction shortening, and wall thickening. After matching their model parameters to their biomechanical markers representing the mean of a healthy human, they ran simulations of the model to match the mean value for patients with DCM, CAD, ischemic heart disease, and HF (though they assume that HF patients are those only with EF below 40%). One of the limitations of this work is the lack of a patient-specific approach, as they match their model simulations to an average patient in each of the diseases, they are trying to represent. Another limitation of this study was the emphasis on modeling the heart and thus the influence of the

systemic and pulmonary circulations on these cardiovascular diseases was ignored (Levrero-Florencio *et al.*, 2020).

Collectively, these previous studies sought to reconcile pressure, volume, and ECG data in cardiovascular disease, paying close attention to the mechanical properties of the LV in control and HF states. Likewise, they all acknowledged the limitations of using LVEF as the ultimate diagnostic tool to distinguish between HF types. In these studies, the modeling the pathophysiology of HF was rarely done in a patient-specific manner, as averages of healthy controls and HF patients were constantly compared to each other without acknowledging the diversity of HF patients, and sometimes only considering those with an EF <40% as true HF. Moreover, although characterizing the mechanical properties of the LV is important in HF, the pulmonary and systemic circulations are rarely integrated into these models. To address this gap in these previous studies, we have developed a method to represent the cardiovascular state of both HFpEF and HFrEF patients to illustrate the underlying mechanistic differences between diagnosis of these two types of HF. Our overall goal was to improve the identification and diagnosis of subpopulations of patients with similar types of HFpEF that may in turn be responsive to mechanism targeted therapies.

1.5 Overview of this Thesis

Here, we aim to discern subgroups within the HFpEF cohort using mathematical modeling and an unsupervised ML approach. To this end, clustering analysis is performed on estimated model parameters identifying HFpEF subgroups that provide hemodynamic insight into functional differences between HFpEF subgroups. Others have attempted to classify HF patients using unsupervised ML on clinical data alone (Kao *et al.*, 2015; Shah, 2019; Cohen *et al.*, 2020; Hahn *et al.*, 2021) and clinical data inform cardiovascular modeling (Wang et al., 2018, 2021; Levrero-

Florencio et al., 2020; Rumindo et al., 2020) to our knowledge, ours is the first study that uses model-based analysis of clinical data and physiology-informed ML to determine sub classifications of HFpEF integrating the cardiac, systemic and pulmonary compartments in the cardiovascular system. This synergistic approach is in line with similar studies that combine mathematical and statistical techniques to predict physiologic function at the patient-specific level (e.g., the "digital twin" (Corral-Acero *et al.*, 2020). A workflow of the approach used in this study is shown in **Figure 1.1**.

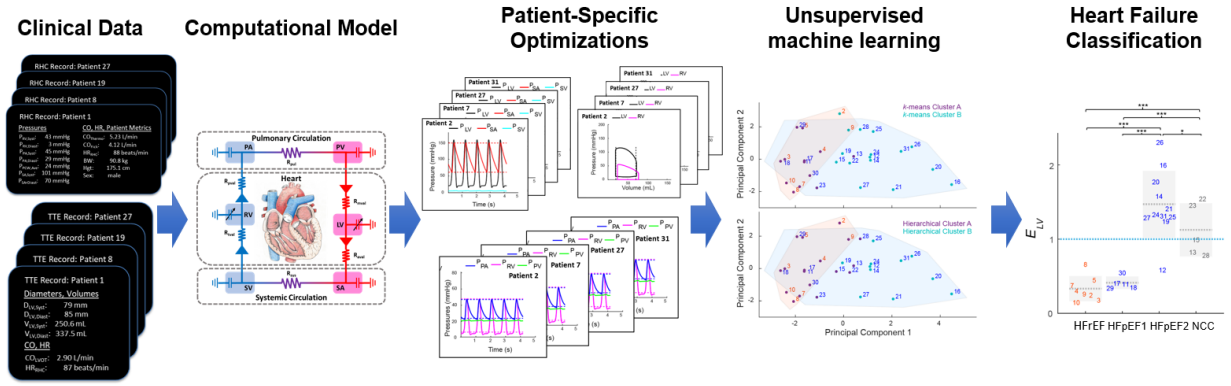

Figure 1.1 Methodology. This schematic shows the workflow analyzing clinical data from right heart catheterization (RHC) and transthoracic echocardiography (TTE) from patients with heart failure with preserved (HFpEF) and reduced (HFrEF) ejection fraction using a patient-specific cardiovascular systems model. A subset of model parameters is optimized to RHC and TTE data for each patient. These parameter values can then be used to observe differences between HFpEF and HFrEF patients and determine subgroups of HFpEF using unsupervised machine learning.

1.5.1 HFpEF Patient Phenotyping

In Chapter 2 of this paper, we develop a method to represent the cardiovascular status of patients with HFpEF and HFrEF and illustrate the underlying mechanistic differences between diagnoses of three distinct subgroups of HFpEF. In Chapter 3, we validate our physiology-based ML approach to HFpEF grouping versus transcriptomics-based grouping of HFpEF patients, and we retrospectively identify selected HFpEF subgroups in clinical trials of atrial shunt devices and drugs that may in future trials be more responsive to therapy.

1.5.2 Control of Myocardial Substrate Selection

Mechanistically, parallel work in our lab has shown that decreased cardiac function in HF is also characterized by a change in mitochondrial metabolism and metabolic fuel utilization (Lopez *et al.*, 2020). HF has also been shown in animal models and humans to alter calcium handling in cardiac muscle cells (Kwong *et al.*, 2015, 2018). In Chapter 4, we determine if and how [Ca^{2+}] affects the relative use of carbohydrates versus fatty acids *in vitro*, by measuring oxygen consumption and tricarboxylic acid (TCA) cycle intermediate concentrations in suspensions of cardiac mitochondria with different combinations of pyruvate and palmitoyl-L-carnitine in the media at various [Ca^{2+}] and ADP infusion rates. Stoichiometric analysis of the data reveals that when both fatty acid and carbohydrate substrates are available, fuel selection is sensitive to both [Ca^{2+}] and ATP synthesis rates.

Chapter 2 Phenotyping Heart Failure Using Model-based Analysis and Physiology-Informed Machine Learning

2.1 Acknowledgements

This chapter was published as an academic journal article in the Journal of Physiology: Jones E, Randall EB, Hummel SL, Cameron DM, Beard DA, Carlson BE. Phenotyping heart failure using model-based analysis and physiology-informed machine learning. J Physiol. 2021 Nov;599(22):4991-5013. doi: 10.1113/JP281845. Epub 2021 Oct 18. PMID: 34510457

The authors thank Sophie E.O. Carlson for the artwork used in **Figure 1.1** and **Figure 2.2** and Matthew C. Konerman, MD for discussions about the clinical utility of our results during the development of this project.

2.2 Abstract

To phenotype mechanistic differences between heart failure with reduced (HFrEF) and preserved (HFpEF) ejection fraction, a closed-loop model of the cardiovascular system coupled with patient-specific transthoracic echocardiography (TTE) and right heart catheterization (RHC) data was used to identify key parameters representing hemodynamics. Thirty-one patient records (10 HFrEF, 21 HFpEF) were obtained from the Cardiovascular Health Improvement Project database at the University of Michigan. Model simulations were tuned to match RHC and TTE pressure, volume, and cardiac output measurements in each patient. The underlying physiological model parameters were plotted against model-based norms and compared between HFrEF and HFpEF. Our results confirm the main mechanistic parameter driving HFrEF is reduced left

ventricular (LV) contractility, whereas HFpEF exhibits a heterogeneous phenotype. Conducting principal component analysis, *k*-means clustering, and hierarchical clustering on the optimized parameters reveal (i) a group of HFrEF-like HFpEF patients (HFpEF1), (ii) a classic HFpEF group (HFpEF2), and (iii) a group of HFpEF patients that do not consistently cluster (NCC). These subgroups cannot be distinguished from the clinical data alone. Increased LV active contractility ($p < 0.001$) and LV passive stiffness ($p < 0.001$) at rest are observed when comparing HFpEF2 to HFpEF1. Analyzing the clinical data of each subgroup reveals that elevated systolic and diastolic LV volumes seen in both HFrEF and HFpEF1may be used as a biomarker to identify HFrEF-like HFpEF patients. These results suggest that modelling of the cardiovascular system and optimizing to standard clinical data can designate subgroups of HFpEF as separate phenotypes, possibly elucidating patient-specific treatment strategies.

2.3 Introduction

Heart Failure with preserved ejection fraction (HFpEF) is diagnosed in patients with the hallmarks of heart failure (HF) and a left ventricular (LV) ejection fraction (EF) equal to or above 50%. HFpEF now represents more than half of HF cases, and its incidence is increasing with an aging population and a high prevalence of associated risk factors (e.g., obesity, systemic hypertension, coronary artery disease, and diabetes) (Yancy *et al.*, 2006; Owan *et al.*, 2006; Hummel *et al.*, 2009; Little & Zile, 2012). Patients with HFpEF suffer poor quality of life and long-term outcomes. Despite this substantial individual and public health burden, HFpEF lacks a framework for evidence-based pharmacotherapy (Yancy *et al.*, 2013). Long-term management of HFpEF focuses on (i) the treatment of any existing comorbidities, (ii) therapeutics that decrease the LV diastolic pressures, and (iii) general symptom reduction. Several clinical trials in large

cohorts of HFpEF patients have failed to demonstrate consistent benefits. The drugs used include Sildenafil (Guazzi *et al.*, 2011; Borlaug *et al.*, 2015; Hoendermis *et al.*, 2015; Liu *et al.*, 2017), Sacubitril/Valsartan (Solomon *et al.*, 2019), Losartan (Wachtell *et al.*, 2010), Candesartan (Yusuf *et al.*, 2003), Spironolactone (Edelmann *et al.*, 2013; Cohen *et al.*, 2020), and Isosorbide mononitrate (Redfield *et al.*, 2015).

HFpEF was previously termed "diastolic" HF with symptoms attributed to increased ventricular stiffness, impaired relaxation, impaired ventricular filling during diastole, and higher average pressures during the cardiac cycle. However, patients with HFpEF have dysfunction in multiple cardiovascular domains, some of which may become evident only during exercise (Dunlay *et al.*, 2017). It has been suggested that selecting the correct HFpEF cohort is an important factor in treatment success (Borlaug *et al.*, 2015), but the wide range of HFpEF phenotypes at the mechanistic cardiovascular systems level makes selecting these cohorts from upper-level clinical data difficult. Since HFpEF is a catch-all category for HF patients based mainly on EF estimates, the inability to have a standard treatment for these patients may be an indicator of the physiological heterogeneity underlying HFpEF. Therefore, identifying subgroups of HFpEF patients with similar cardiovascular etiologies is a crucial task required to target appropriate therapies for these patients. Patients presenting with HF and an EF below 50% are diagnosed with heart failure with reduced ejection fraction (HFrEF). The classical understanding of HFrEF, also known as "systolic" HF, is that loss of ventricular contractility causes reduced ability to pump blood to the systemic circulation during systole (Pinilla-Vera *et al.*, 2019). Unlike HFpEF, numerous medication and device-based therapies improve outcomes in HFrEF (Yancy *et al.*, 2017; Pinilla-Vera *et al.*, 2019)
.

To diagnose and monitor patients with HF, two clinical procedures are commonly used: transthoracic echocardiography (TTE) and right heart catheterization (RHC). TTE is noninvasive and widely available, and these images may be used to quantify LV volumes in systole and diastole to estimate a patient's EF. From TTE measurements, we may obtain additional information, such as cardiac output (CO) based on the heart rate (HR), the left ventricular out track flow velocity time integral (LVOT VTI) and the cross-sectional aortic valve area for each patient. RHC is used to measure right ventricular (RV) and pulmonary artery (PA) pressures during systole and diastole along with CO, HR, and pulmonary capillary wedge pressure (PCW). While TTE and RHC provide detailed ventricular volume and pressure data for individual patients, the challenge of integrating these measurements into a single representation of a patient's cardiovascular state is only made qualitatively in the clinic. One way to quantitatively reconcile what these clinical datasets describe about the hemodynamics of the right and left sides of the heart and the systemic and pulmonary circulation is with a closed-loop model of the cardiovascular system. To combine these two sets of data, we must take into consideration that (i) the two datasets are typically not obtained simultaneously, (ii) they may include a combination of data points taken at specific instances, and (iii) time course data are often not available.

In this retrospective study, we have developed a methodology to represent the cardiovascular state of both HFpEF and HFrEF patients to illustrate the underlying mechanistic differences between diagnoses and specifically within the diagnosis of HFpEF. Recent studies have determined subgroups of the HFpEF diagnosis using RNA sequencing (Hahn *et al.*, 2021), quantitative echocardiography (Shah, 2019), and plasma protein profiling (Cohen *et al.*, 2020) combined with unsupervised machine learning techniques.

Here, we aim to discern subgroups within the HFpEF cohort using a mathematical modeling and unsupervised machine learning approach. To this end, a clustering analysis is performed on estimated model parameters identifying HFpEF subgroups that provide hemodynamic insight into functional differences between HFpEF subgroups. Others have attempted to classify HF patients using clinical data to inform cardiovascular modeling (Wang *et al.*, 2018). To our knowledge, ours is the first study that uses model-based analysis of clinical data and physiology-informed machine learning to determine subclassifications of HFpEF. This synergistic approach is in line with similar studies that combine mathematical and statistical techniques to predict physiological function at the patient-specific level (e.g., the "digital twin" (Corral-Acero *et al.*, 2020)). A workflow of the approach used in this study is shown in. A workflow of the approach used in this study is shown in **Figure 1.1**.

2.4 Clinical Data

The Cardiovascular Health Improvement Project (CHIP) repository, supported by the Frankel Cardiovascular Center at the University of Michigan, was queried to extract clinical data from patients diagnosed with HFpEF or HFrEF. This retrospective data capture was approved by the Institutional Review Board at the University of Michigan, and informed consent was obtained for all subjects in the database. This research-ready biorepository of DNA, plasma, serum, and tissue samples includes de-identified electronic health records (EHRs) from consenting patients with HF, aortic disease, arrhythmia, and dyslipidemia. Through the CHIP office, a search was made to collect clinical data from HFpEF and HFrEF patients with both TTE and RHC measurements in their EHR. The criteria for determining whether a patient has HFpEF or HFrEF is a history of HF symptoms and an EF above 50% or below 50%, respectively. Patients with both

procedures within 90 days of each other were extracted from all HFpEF and HFrEF records in a time range from February 2016 through February 2019. With this query, 62 patient records (26 HFrEF and 36 HFpEF) were collected. Patient records missing the minimal number of measurements (see below) from RHC and TTE procedures eliminated 10 HFrEF and 13 HFpEF records, leaving 34 patient records (11 HFrEF and 23 HFpEF). Finally, one HFrEF and two HFpEF records that appeared to be outliers during the initial phase of our analysis were followed up in the patient record and found to have procedures or treatments that changed their original cardiovascular diagnosis (e.g., chemotherapy changing a patient from HFpEF to HFrEF). These three patients were omitted from our final analysis, leaving 31 patient records (10 HFrEF and 21 HFpEF).

2.4.1 RHC Data

During this invasive procedure, a Swan-Ganz catheter was inserted through the jugular vein and measured the pressure at the tip of the catheter as it advanced into the pulmonary artery. RHC CO was estimated by using the thermodilution or Fick methods. The thermodilution technique estimates CO by measuring dispersion of a cold saline bolus injected at the proximal end and then sensed at the distal end of the catheter. The Fick method measures venous and arterial O_2 saturation and often assumes a given whole body oxygen consumption ($\dot{V}O_2$) based on weight, height, and sex. The accuracy of the Fick method hinges on correctly estimating $\dot{V}O_2$, and it has been determined that it can vary by as much as 25% when compared to a direct measurement of $\dot{V}O_2$ (Narang *et al.*, 2014). Since all RHC records in this study used estimated $\dot{V}O_2$, we have chosen to use the thermodilution method as a consistent measure of RHC CO.

The selected RHC datasets came from reports that contained at least the following 13 clinically measured values: systolic and diastolic RV pressures, systolic and diastolic PA pressures, average PCW pressure, systolic and diastolic SA pressure, HR during the RHC, CO (thermodilution and Fick), body weight, height, and sex (**Table 2.1**). To ensure that the RHC measurements used are consistent, HR and systolic and diastolic systemic pressures were gathered from the RHC report only during catheter insertion. If multiple measurements were taken during this period, an average was computed of the values recorded.

2.4.2 TTE Data

The selected TTE data include at a minimum: measurements of LV volume in systole and diastole and HR during TTE. The LV volumes are measured as either (i) a single diameter across the LV just below the mitral valve leaflet tips or (ii) tracings of the LV from apical two- and four-chamber views (Lang RM *et al.*, 2016). The single diameter derived volumes assume the LV can be approximated as a truncated prolate spheroid with a nonlinear relationship between the diameter and length of the ventricle (Teichholz et al., 1976). Volumes derived from the two- and four-chamber views are calculated by the Method of Discs (MOD), also known as Simpson's method (Lang RM et al. 2016). Since MOD is preferred for the estimation of LV volumes over the single diameter estimation, all patient raw TTE images were reviewed by a cardiologist to: (i) Obtain a MOD estimate of LV volumes when the quality of the image allowed, (ii) Determine the HR, and (ii) Extract an LVOT VTI estimate of CO, when possible.

Table 2.1 Right heart catheterization (RHC) data, transthoracic echocardiogram (TTE) data, and patient biometrics.

	Patient	RHC Data									TTE Data				Patient Biometrics		
		P_{RV} Sys	P_{RV} Dias	P_{PA} Sys	P_{PA} Dias	$\bar{P}_{PCW}$	P_{SA} Sys	P_{SA} Dias	CO_{RHC}	HR_{RHC}	V_{LV} Sys	V_{LV} Dias	HR_{TTE}	CO_{TTE}	BW	Height	Sex
HFrEF	**1**	43	3	45	29	24	101	70	5.2	88	250.6	337.5	87	2.9	90.8	175.1	M
	2	65	9	69	24	26	113	81	3.6	84	116.3	169.3	100	3.1	90.3	167.8	M
	3	21	5	20	11	13	70	45	3.2	68	106.5	115	74	3.2	46.3	162.6	F
	4	50	7	42	26	24	109	60	3.7	66	87.9	147.5	76	4.1	91.9	157.2	F
	5	45	13	44	22	29	155	98	5.4	68	57.38	202.4	72	4.5	86.2	182.9	M
	6	28	1	30	11	11	81	50	3.9	60	231.9	303.3	68	2.1	56.7	162.6	F
	7	48	7	47	24	19	149	61	5.5	72	92.2	179.52	70	5.5	112.5	182.9	M
	8	25	4	26	13	8	96	66	5.6	69	35.8	99.1	84	3.1	78.4	158	F
	9	51	30	52	8	25	116	70	3	82	107	127.7	84	8.1	67.3	183	M
	10	41	6	43	22	22	83	60	3.4	78	153.2	162.4	98	3.3	98.1	177	M
	Mean	41.7	8.5	41.8	17	20.1	107.3	66.1	4.2	73.4	123.9	184.4	81.3	4	81.9	170.9	
	Median	44	6.5	43.5	17.5	23	105	63.7	3.8	70.2	106.8	165.9	80	3.3	88.3	171.5	
	SD	12.8	7.8	13.2	6.8	6.7	26.3	14.5	1	8.7	66.1	74.4	10.7	1.6	19	10	
HFpEF	**11**	46	10	44	20	19	159.5	65.5	6.1	58	99	210	67	5	109.3	158.7	F
	12	76	13	69	31	19	108	71.5	5.8	60	51.2	83	70	4.6	106.6	177.9	M
	13	53	8	54	24	28	158	64.5	6.84	76	44	107.2	74	4.7	107.5	160	F
	14	86	25	89	53	28	165.5	91.5	5.7	64	24.5	92.2	66	4.5	139.7	173	M
	15	56	9	53	31	27	146	72	6.1	65	34.9	112.5	70	5.4	101.2	165.1	F
	16	45	3	45	20	19	165	69	4.4	63	21.5	57.1	64	3.9	59.4	162.8	F
	17	66	6	66	31	29	111	58	3.5	66	65.7	135	69	4.8	136.2	168.3	M
	18	42	13	42	23	25	119	76	7.43	101	54.3	159.6	66	4.3	98	166.3	F
	19	65	17	65	33	78	164	91	5.67	68	31.9	100.9	73	3.2	125.7	157.3	F
	20	88	7	87	25	8	134	60	3.5	53	23.9	49.8	50	3.4	63	160	F
	21	37	2	37	18	18	123	63	3.37	67	20.1	58	67	4.6	68.1	171.4	M
	22	72	8	72	28	28	157.5	71.5	5.63	71	24.5	117.9	85	5.1	105.3	160	F
	23	31	5	33	15	14	136	57	4.5	59	22.1	146.7	67	4.9	62.4	163	F
	24	45	11	40	22	14	119	73	6.23	78	22.1	62.8	88	6.1	110.4	166	F
	25	104	13	104	39	37	143	82	3.67	75	24.6	96.4	88	4.2	78.9	169	M
	26	63	18	65	32	30	121.5	69.5	3.47	58	11.8	58.8	70	4.2	80.5	157	F
	27	56	0	53	21	13	105	55	2.9	53	19.9	70.9	55	3.6	60.2	154	M
	28	60	10	59	31	17	118	81	4.03	77	34.9	97.1	85	5.3	102.4	168	M
	29	73	12	73	19	29	104	60	7.27	65	69.8	147	64	4.9	106.7	175	M
	30	65	19	65	34	34	65	34	5.25	80	28.4	77.3	85	4.3	68.8	165	M
	31	50	9	49	24	26	156	81	7.53	85	27	70	81	6.7	89.4	159	F
	Mean	60.9	10.4	60.2	27.3	25.7	132.3	68.9	5.2	68.6	36	100.5	71.6	4.7	94.3	164.6	
	Median	60	10	59	25	26	134	69.5	5.6	66	27	96.4	70	4.6	101.2	165	
	SD	17.7	5.9	17.9	8.4	13.8	25.8	12.8	1.4	11.3	20.7	40	10.2	0.8	24.1	6.2	

HFrEF – heart failure with reduced ejection fraction. HFpEF – heart failure with preserved ejection fraction. P – pressure. V – volume. CO – cardiac output. HR – heart rate. BW – body weight. Sys – systole. Dias – diastole. Subscripts: LV – left ventricle. RV – right ventricle. PA – pulmonary arteries. PCW – pulmonary capillary wedge. SA – systemic arteries. Bar notation indicates an average pressure.

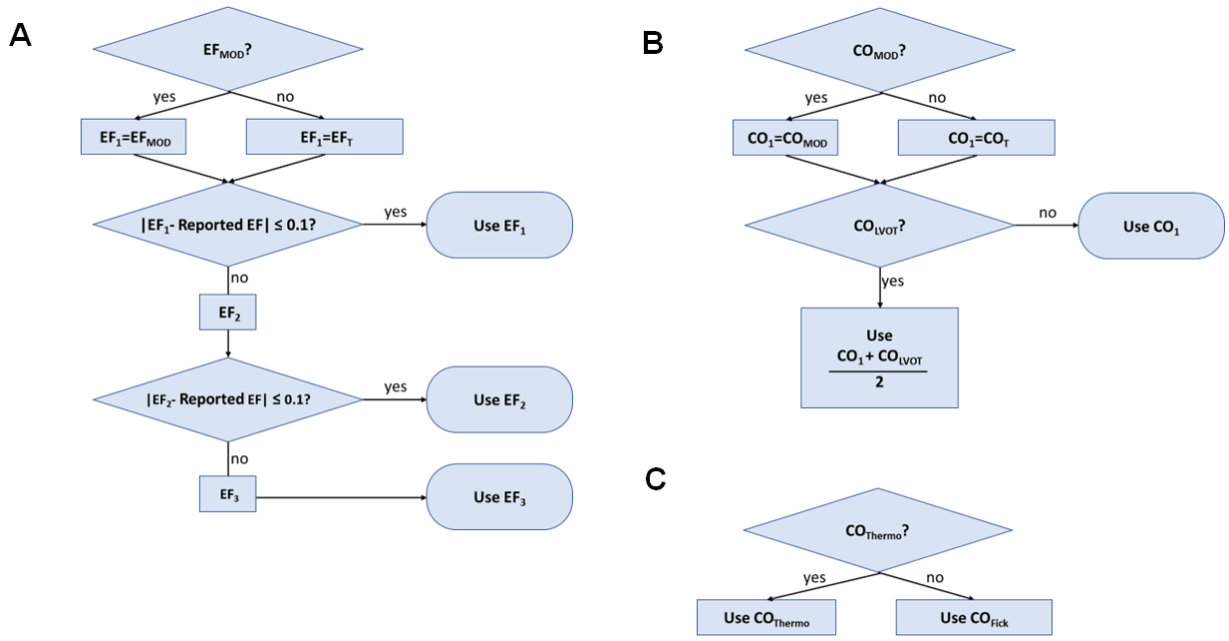

Figure 2.1 Decision trees. These trees are used to determine which calculation of ejection fraction (EF) and cardiac output (CO) should be used in the right heart catheterization (RHC) and transthoracic echocardiography (TTE) data. **A.** EF from TTE data. This decision tree is used to resolve discrepancies between the reported EF in TTE records and those calculated by Method of Discs (MOD) and Teichholz's formula (EF_T). The result is set to EF_1. EF_2 and EF_3 are calculated using **Equations** 2.1 **and** 2.2, respectively. **B**. CO from TTE data. An estimate of CO from left ventricular (LV) volumes in systole and diastole through the MOD (CO_{MOD}) is our first choice. If CO_{MOD} is not available, CO estimates are calculated from LV diameter data during systole and diastole using Teichholz's formula (CO_T). The result is set as CO_1. If a left ventricular out track flow velocity time integral (LVOT VTI) CO estimate (CO_{LVOT}) is also available, CO_{LVOT} is averaged with CO_1. **C.** CO from RHC data. CO determined via thermodilution (CO_{Thermo}) takes precedence over CO calculated using the Fick method (CO_{Fick}).

2.5 Clinical Data Inconsistency/Discrepancy

2.5.1 Ejection Fraction

All patients had a reported EF determined visually by a cardiologist. To quantitively determine the EF, Cameron revisited the TTE images to reassess LV volumes by MOD (EF_{MOD}) (Wyatt *et al.*, 1979). There are some patients where the two- and four-chamber images were not of high enough resolution to yield a MOD estimate. In these cases, the LV volumes and CO are calculated from a single diameter measured across the top of the LV using the Teichholz equation

(EF_T). (Teichholz *et al.*, 1976). If EF_{MOD} was able to be calculated, we assign this value as EF_1, and if not, $EF_1 = EF_T$. This method revealed discrepancies between the reported EF and EF_1. To address this discrepancy, we had a third evaluation performed by Hummel to determine whether EF_1 should be used. If the distance between the reported EF and EF_1 is less than 0.1, we use EF_1. Otherwise, we apply the rule

$$\mathrm{EF}_2 = \frac{\mathrm{SV}_{LVOT}}{V_{LV,diast}}, \tag{2.1}$$

where SV_{LVOT} is the stroke volume (SV) determined by LVOT VTI, and $V_{LV,diast}$ is the diastolic LV volume determined by MOD or Teichholz. If the distance between the reported EF and EF_2 is less than 0.1, we use EF_2 **Equation** 2.1. Otherwise, we apply the rule

$$\mathrm{EF}_3 = \frac{\mathrm{SV}_{LVOT}}{V_{LV,syst} + \mathrm{SV}_{LVOT}}, \tag{2.2}$$

where $V_{LV,syst}$ is the systolic LV volume determined by MOD or Teichholz. The decision tree for the reassessment of EF is shown in **Figure 2.1A** and **Table 2.2** lists the EF calculation used for each patient: EF from MOD (EF_{MOD}), EF from Teichholz's equation (EF_T) (Teichholz *et al.*, 1976), EF_2 calculated using **Equation** 2.1 and EF_3 calculated using **Equation** 2.2**.**

Table 2.2 Ejection Fraction (EF) calculation for each patient

Patient	Method	Patient	Method
HFrEF			
1	EF_{MOD}	6	EF_{MOD}
2	EF_{MOD}	7	EF_T
3	EF_{MOD}	8	EF_{MOD}
4	EF_2	9	EF_3
5	EF_2	10	EF_{MOD}
HFpEF			
11	EF_{MOD}	22	EF_T
12	EF_3	23	EF_3
13	EF_T	24	EF_{MOD}
14	EF_T	25	EF_{MOD}
15	EF_T	26	EF_{MOD}
16	EF_{MOD}	27	EF_{MOD}
17	EF_T	28	EF_T
18	EF_T	29	EF_T
19	EF_{MOD}	30	EF_{MOD}
20	EF_{MOD}	31	EF_{MOD}
21	EF_T		

EF_{MOD} - EF from Method of Discs (Wyatt *et al.*, 1979).
EF_T - EF from Teichholz's equation (Teichholz *et al.*, 1976).
EF_2 - **Equation** 2.1
EF_3 – **Equation** 2.2

2.5.2 Cardiac Output

Both TTE and RHC data can contain multiple estimates of CO. The TTE itself resulted in a possibility of three separate CO estimates:

(i) HR times the SV using MOD (CO_{MOD}),

(ii) HR times the SV using the Teichholz equation (CO_T), and

(iii) HR times LVOT VTI times the cross-sectional area of the outflow tract (CO_{LVOT}) (Lang RM *et al.*, 2016).

We have developed a systematic method to rank the quality of these measurements and determine a CO estimate to be used for parameter optimization, as shown by the decision tree

(**Figure 2.1B**). If CO_{MOD} is available, we assign this value as CO_1, and if not, $CO_1 = CO_T$. If CO_{LVOT} is available, we average CO_1 and CO_{LVOT}. Otherwise, CO_1 is taken as the TTE CO for the patient. For the RHC, there are two CO estimates:

(i) CO by thermodilution (CO_{Thermo}), and

(ii) CO calculated via the Fick method (CO_{Fick}).

If CO_{Thermo} is available, it is taken as the patient's CO from RHC. If not, CO_{Fick} is used (**Figure 2.1C**). **Table 2.1** shows the data used in this study screened with these decision criteria.

2.6 Mathematical Modeling Framework

The cardiovascular systems model is similar to that used in a previous study from our lab (Colunga *et al.*, 2020) and is based on the formulation developed by Smith et al. (Smith *et al.*, 2004). **Figure 2.2** shows the detailed cardiovascular model schematic including the 6 compartments represented by the model: left ventricle (LV), systemic arteries (SA), systemic veins (SV), right ventricle (RV), pulmonary arteries (PA), and pulmonary veins (PV). The model complexity was reduced significantly since the clinical data used for parameterization here do not have enough informational content to uniquely identify the parameters of the full Smith et al. model. In our previous reduced version of the model, ventricular-ventricular interaction and fluid inertance after each heart valve were omitted. Additionally in this study, the pericardial compartment was removed, and the zero pressure (or dead space) volumes in all vascular and ventricular compartments were set to zero.

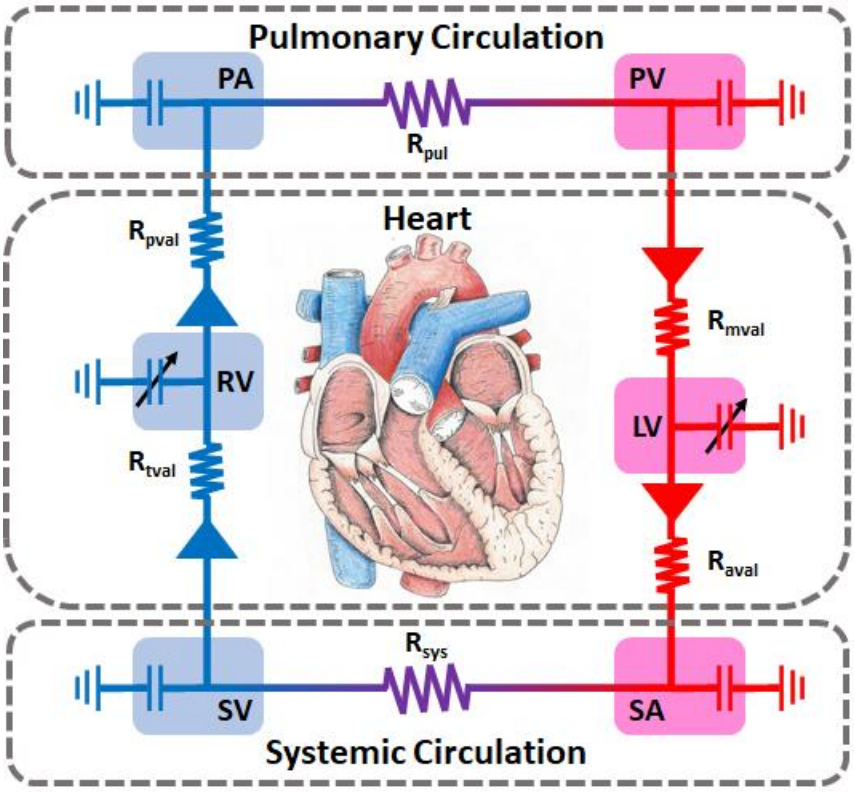

Figure 2.2 Model schematic. The cardiovascular system model is described using an electrical circuit analogy where pressure, volume, and flow correspond to voltage, charge, and current, respectively. There are 6 compartments (clockwise): left ventricle (LV), systemic arteries (SA), systemic veins (SV), right ventricle (RV), pulmonary arteries (PA), and pulmonary veins (PV). The model has a systemic (R_{sys}) and pulmonary (R_{pul}) resistance denoting the drop in pressure from the arterial to venous compartments. Heart valves are simulated as diodes (triangles) with an associated resistance: mitral valve (R_{mval}), aortic valve (R_{aval}), tricuspid valve (R_{tval}), and pulmonary valve (R_{pval}).

Overall, the model used here has 6 states (compartmental blood volumes are listed in **Equations (**2.20**) – (**2.25**)**) and 16 parameters each with a specific physiological interpretation (**Table 2.3**). Equations for the reduced cardiovascular system model used in this study are given below and model code without parameter optimization can be found at (Carlson & Jones, n.d.).

Table 2.3 Model parameters for patients at rest.

Symbol	Units	Description	Value	Lower bound	Upper bound	Fixed	Adjustable
Left Ventricle (LV)							
E_{LV}	mmHg mL^{-1}	LV active contractility	4.32	0.1	10		X
$P_{0,LV}$	mmHg	LV diastolic reference pressure	0.12	0.01	5	X	
λ_{LV}	mL^{-1}	LV passive stiffness	0.02	0.005	0.1		X
Right Ventricle (RV)							
E_{RV}	mmHg mL^{-1}	RV active contractility	0.70	0.05	5		X
$P_{0,RV}$	mmHg	RV diastolic reference pressure	0.22	0.01	5	X	
λ_{RV}	mL^{-1}	RV passive stiffness	0.02	0.005	0.1		X
Pulmonary arteries (PA) and veins (PV)							
E_{PA}	mmHg mL^{-1}	PA stiffness	0.26	0.05	5		X
E_{PV}	mmHg mL^{-1}	PV stiffness	0.01	0.0005	0.1		X
R_{pul}	mmHg s mL^{-1}	Pulmonary resistance	0.13	0.005	1		X
Systemic arteries (SA) and veins (SV)							
E_{SA}	mmHg mL^{-1}	SA stiffness	0.90	0.05	5		X
E_{SV}	mmHg mL^{-1}	SV stiffness	0.01	0.0001	0.1	X	
R_{sys}	mmHg s mL^{-1}	Systemic resistance	1.28	0.05	15		X
Heart valve resistances							
R_{mval}	mmHg s mL^{-1}	Mitral valve	0.016	0.005	0.5	X	
R_{aval}	mmHg s mL^{-1}	Aortic valve	0.018	0.005	0.5	X	
R_{tval}	mmHg s mL^{-1}	Tricuspid valve	0.024	0.005	0.5	X	
R_{pval}	mmHg s mL^{-1}	Pulmonary valve	0.006	0.0004	0.25	X	

2.6.1 Model Equations

The cardiovascular systems model used for this study is a reduced version of the Smith et al. model (Smith *et al.*, 2004) adapted from our previous study(Colunga *et al.*, 2020). This reduced version balances the degree of model complexity with the informational content of the clinical data. Further reduction was made by omitting the pericardium and all zero pressure volumes in each compartment were set to zero. The elastance function driving heart systole and diastole depend on a periodic τ, the time from the beginning of the current cardiac cycle, as

$$e_{\tau} = \exp\left\{-\mathrm{HR}\left(\tau - \frac{1}{2\mathrm{HR}}\right)^2\right\}. \quad (2.3)$$

LV and RV ventricular pressure from end-systolic (*es*) and end-diastolic (*ed*) pressure-volume relationships are

$$P_{es,LV} = E_{LV}\, V_{LV}, \tag{2.4}$$

$$P_{ed,LV} = P_{0,LV}\left(e^{\lambda_{LV} V_{LV}} - 1\right) \tag{2.5}$$

$$P_{LV} = e_{\tau} P_{es,LV} + (1 - e_{\tau}) P_{ed,LV}, \tag{2.6}$$

$$P_{es,RV} = E_{RV}\, V_{RV}, \tag{2.7}$$

$$P_{ed,RV} = P_{0,RV}\left(e^{\lambda_{RV} V_{RV}} - 1\right), and \tag{2.8}$$

$$P_{RV} = e_{\tau} P_{es,LV} + (1 - e_{\tau}) P_{ed,RV}, \tag{2.9}$$

where V_i is the compartment volume, E_i is a stiffness parameter, $P_{0,i}$ is a reference pressure, and λ_i reflects the passive stiffness. The systemic arterial (*SA*), systemic venous (*SV*), pulmonary arterial (*PA*), and pulmonary venous (*PV*) pressures are

$$P_{SA} = E_{SA} V_{SA}, \tag{2.10}$$

$$P_{SV} = E_{SV} V_{SV}, \tag{2.11}$$

$$P_{PA} = E_{PA} V_{PA}, \text{and} \tag{2.12}$$

$$P_{PV} = E_{PV} V_{PV}. \tag{2.13}$$

Blood flow is modeled using Ohm's law. Flow through the systemic (*sys*) and pulmonary (*pul*) circulations are

$$Q_{sys} = \frac{P_{SA} - P_{SV}}{R_{sys}}\ and \tag{2.14}$$

$$Q_{pul} \frac{= P_{PA} - P_{PV}}{R_{pul}}\ . \tag{2.15}$$

Flows through the heart valves mitral (*mval*), aortic (*aval*), tricuspid (*tval*), and pulmonary (*pval*) are treated as diodes to prevent backflow, that is,

$$Q_{mval} = \begin{cases} \dfrac{P_{PV} - P_{LV}}{R_{mval}} & if\ P_{PV} > P_{LV} \\ 0 & otherwise\ , \end{cases} \tag{2.16}$$

$$Q_{aval} = \begin{cases} \dfrac{P_{LV} - P_{SA}}{R_{aval}} & if\ P_{LV} > P_{SA} \\ 0 & otherwise\ , \end{cases} \tag{2.17}$$

$$Q_{tval} = \begin{cases} \dfrac{P_{SV} - P_{RV}}{R_{tval}} & if\ P_{SV} > P_{RV} \\ 0 & otherwise\ , \end{cases} \tag{2.18}$$

and

$$Q_{pval} = \begin{cases} \dfrac{P_{RV} - P_{PA}}{R_{pval}} & if\ P_{RV} > P_{PA} \\ 0 & otherwise\ . \end{cases} \tag{2.19}$$

This model conserves volume by formulating differential equations using Kirchoff's Law, that is,

$$\frac{\mathrm{d}V_{LV}}{\mathrm{d}t} = Q_{mval} - Q_{aval}, \tag{2.20}$$

$$\frac{dV_{SA}}{\mathrm{d}t} = Q_{aval} - Q_{sys}, \tag{2.21}$$

$$\frac{dV_{SV}}{\mathrm{d}t} = Q_{sys} - Q_{tval}, \tag{2.22}$$

$$\frac{dV_{RV}}{\mathrm{d}t} = Q_{tval} - Q_{pval}, \tag{2.23}$$

$$\frac{dV_{PA}}{\mathrm{d}t} = Q_{pval} - Q_{pul}, \tag{2.24}$$

$$\frac{dV_{PV}}{\mathrm{d}t} = Q_{pul} - Q_{mval}. \qquad (2.25)$$

2.6.2 Normal Cardiovascular Function Parameterization

Table 2.3 describes all model parameters and lists the nominal values that result in normal cardiovascular function. This set of parameters prescribes a patient with roughly 120/80 mmHg SA pressure, 20/9 mmHg PA pressure, 85 mL LV diastolic volume, 57 mL LV SV (for EF of 67%), and 4.6 L min^{-1} CO). These values vary from the original Smith model parameters because we have reduced their model and then adjusted the remaining parameters to produce cardiovascular function similar to the full Smith model. **Figure 2.3** shows the model predictions for normal cardiovascular function corresponding to the parameters listed in **Table 2.3**.

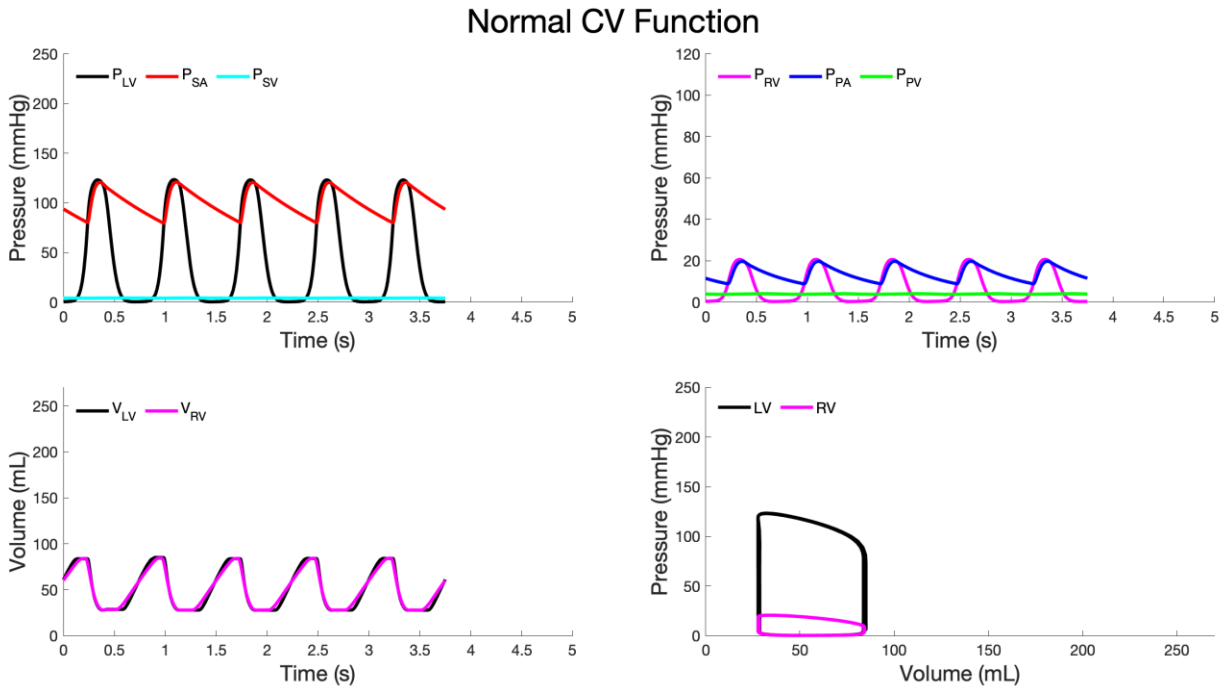

Figure 2.3 Simulation of normal cardiovascular function.

2.6.3 Nominal Parameters and Initial Conditions

Nominal estimates of all parameters are determined starting with the set of expressions from our previous study (Colunga *et al.*, 2020) as a guide. However, some estimated values used in the previous nominal parameter calculations can be replaced with data or calculated directly since TTE measurements are available. Therefore, a reformulation of some nominal parameter expressions has been made in this study:

- LV elastances were calculated from measured volume and estimated pressure in systole.
- LV diastolic stiffness was calculated from measured volume and estimated pressure in diastole.
- RV elastances were calculated from measured pressure and estimated volume in systole.
- RV diastolic stiffness was calculated from measured pressure and estimated volume in diastole.
- Systemic elastances were calculated from measured arterial pulse pressures, estimated venous pulse pressures, and estimated stressed volumes.
- Pulmonary elastances were calculated from estimated and measured pulse pressures and estimated stressed volumes.
- Systemic and pulmonary resistances were calculated from measured systemic and pulmonary average arterial pressures and estimated systolic venous pressure along with the measured RHC CO.

Resistances across the four valves were calculated in exactly the same way as in our previous study, and the ventricular end-diastolic reference pressures were set to normal values from Smith et al. More details on the exact expressions used for nominal calculations are shown below.

2.6.4 Calculation of Nominal Parameters

Nominal values for 14 of the 16 parameters in the model are specified for each patient using a combination of each patient's clinical data, the model equations, and values from the literature. The equations below are a summary of the nominal parameter calculation function from the code.

A. Estimating Patient-specific Model Pressures and Volumes from Clinical Measures

The following equations calculate estimates for pressures and volumes in systole and diastole from the clinical data listed in **Table 2.4**.

Table 2.4 Clinical measures used for calculation of nominal parameter values

Symbol	Description
$V_{LV,syst}$	LV systolic volume
$V_{LV,diast}$	LV diastolic volume
$P_{RV,syst}$	RV systolic pressure
$P_{RV,diast}$	RV diastolic pressure
$P_{SA,syst}$	SA systolic pressure
$P_{SA,diast}$	SA diastolic pressure
$P_{PCW,ave}$	Average PCW pressure
$P_{PA,syst}$	PA systolic pressure
$P_{PA,diast}$	PA diastolic pressure
$P_{SV,pp}$	SV pulse pressure
CO_{RHC}	Right heart catheter cardiac output

PCW- pulmonary capillary wedge.

The bar notation ($\bar{\cdot}$) indicates a nominal estimate whereas no bar indicates a clinical measure. RV compartment volume estimates are assumed to be 90% of the LV volumes in both systole (*syst*) and diastole (*diast*), that is,

$$\bar{V}_{RV,syst} = 0.90\, V_{LV,syst}, \text{and} \tag{2.26}$$

$$\bar{V}_{RV,diast} = 0.90\, V_{LV,diast}. \tag{2.27}$$

Pressure drop across the aortic and pulmonary valve is assumed to be ~2.5%. Also, pulse pressure (*pp*) in the pulmonary veins is assumed to be ~20% of the PA pulse pressure, whereas SV pulse pressure is ~5% of the SA pulse pressure. The following summarize the pressure estimates:

$$P_{LV,syst} = 1.025\, P_{SA,syst} \tag{2.28}$$

$$P_{LV,diast} = 0.975\, \bar{P}_{PV,diast} \tag{2.29}$$

$$\bar{P}_{PV,pp} = 0.20\left(P_{PA,syst} - P_{PA,diast}\right) \tag{2.30}$$

$$\bar{P}_{SV,pp} = 0.05\left(P_{SA,syst} - P_{SA,diast}\right) \tag{2.31}$$

$$\bar{P}_{PV,diast} = P_{PCW,ave} - \frac{1}{3}\bar{P}_{PV,pp} \tag{2.32}$$

$$P_{PA,ave} = \frac{1}{3}\, P_{PA,syst} + \frac{2}{3}\, P_{PA,diast} \tag{2.33}$$

$$P_{SA,ave} = \frac{1}{3}\, P_{SA,syst} + \frac{2}{3} P_{SA,diast} \tag{2.34}$$

$$\overline{P}_{RV,diast} = \begin{cases} \frac{1}{2}\overline{P}_{SV,pp}\ if\ P_{RV,diast} \le 0 \\ P_{SV,pp} \qquad\quad otherwise \end{cases} \tag{2.35}$$

$$\bar{P}_{SV,diast} = \begin{matrix} 1.025\, \overline{P}_{RV,diast}\ if\ P_{RV,diast} \le 0 \\ 1.025\, P_{RV,diast}\ P_{RV,diast} > 0 \end{matrix} \tag{2.36}$$

$$\bar{P}_{SV,syst} = \bar{P}_{SV,diast} + \bar{P}_{SV,pp} \tag{2.37}$$

$$\bar{P}_{PV,syst} = \begin{cases} P_{PCW,ave} + \frac{2}{3}\bar{P}_{PV,pp} \\ if\ 0.975\, P_{PA,syst} \ge \\ 0.4854\, P_{PA,syst} \qquad\qquad P_{PCW,ave} + \frac{2}{3}\bar{P}_{PV,pp} \\ if\ 0.975\, P_{PA,syst} < P_{PCW,ave} + \frac{2}{3}\bar{P}_{PV,pp} \end{cases} \tag{2.38}$$

For the nominal values of $\bar{V}_{PA,syst}$, $\bar{V}_{PV,syst}$, $\bar{V}_{SA,syst}$,see nominal/initial volume calculation in see in section below.

B. Calculating Nominal Parameters from Pressure and Volume Estimates

The LV and RV end-diastolic reference pressures ($P_{0,LV}$ = 0.1203 mmHg and $P_{0,RV}$ = 0.2157 mmHg) are set at nominal values so the ventricular end-diastolic stiffness exponents (λ_{LV} and λ_{RV}) can be estimated explicitly from the model equations, i.e.,

$$\bar{\lambda}_{LV} = \frac{ln\left(P_{LV,diast}/P_{0,LV}\right)}{V_{LV,diast}} \text{and} \tag{2.39}$$

$$\bar{\lambda}_{RV} = \begin{matrix} \frac{ln\left(\bar{P}_{RV,diast}/P_{0,RV}\right)}{\bar{V}_{RV,diast}} \; if \; P_{RV,diast} \leq 0 \\ \frac{ln\left(P_{RV,diast}/P_{0,RV}\right)}{\bar{V}_{RV,diast}} \; if \; P_{RV,diast} > 0 \end{matrix} \tag{2.40}$$

For the nominal RV passive stiffness (λ_{RV}), when the RV diastolic pressure ($P_{RV,diast}$) is nonpositive, a positive value is calculated from the estimate of the SV pulse pressure ($P_{SV,pp}$). When dealing with clinical data, some measurements are not consistent with each other. For example, the pulmonary arterial systolic pressure ($P_{PA,syst}$) is sometimes greater than the RV systolic pressure ($P_{RV,syst}$), likely due to the fact that these two measurements are made serially rather than simultaneously. In this case, computation of the nominal pulmonary valve resistance (R_{pval}) value is made differently than if $P_{RV,syst}$ is greater than $P_{PA,syst}$. For the nominal tricuspid valve resistance (R_{tval}), when the RV diastolic pressure ($P_{RV,diast}$) is nonpositive, a positive value is calculate from $P_{SV,pp}$. For the nominal pulmonary valve resistance (R_{pval}), when the measured $P_{PA,syst}$ is larger than $P_{RV,syst}$, a pressure drop of 2.5% across the pulmonary valve is assumed to generate a nonnegative estimate of RPV. All heart valve resistances are computed as

$$\bar{R}_{mval} = \frac{\bar{P}_{PV,diast} - \bar{P}_{LV,diast}}{CO_{RHC}} \tag{2.41}$$

$$\bar{R}_{aval} = \frac{\bar{P}_{LV,syst} - \bar{P}_{SA,syst}}{CO_{RHC}} \tag{2.42}$$

$$\bar{R}_{tval} = \begin{cases} \dfrac{\bar{P}_{SV,diast} - \bar{P}_{RV,diast}}{CO_{RHC}} \; if \; P_{RV,diast} \leq 0 \\ \dfrac{\bar{P}_{SV,diast} - \bar{P}_{RV,diast}}{CO_{RHC}} \; if \; P_{RV,diast} > 0 \end{cases} \tag{2.43}$$

$$\bar{R}_{pval} = \begin{cases} \dfrac{P_{RV,syst} - \bar{P}_{PA,syst}}{CO_{RHC}} \; if \; P_{PA,syst} \leq P_{RV,syst} \\ \dfrac{\bar{P}_{SV,diast} - \bar{P}_{RV,diast}}{CO_{RHC}} \; if \; P_{PA,diast} > P_{RV,syst} \end{cases} \tag{2.44}$$

For the nominal pulmonary resistance (R_{pul}), calculating *Rpul* from the clinical data led to three different scenarios. In most cases, adding 2/3 of the estimated PV pulse pressure ($PPV_{,pp}$) to the average pulmonary capillary wedge pressure ($PPCW_{,ave}$) resulted in a pressure that was smaller than average PA pressure ($PPA_{,ave}$). In some cases, this is not true, but this sum is still less than the PA systolic pressure ($PPA_{,syst}$), so we substitute $PPA_{,syst}$ for $PPA_{,ave}$. In a small number of cases, the $PPCW_{,ave}$ is actually much larger than the upstream $PPA_{,syst}$, which is not physiologically possible. In this case, we estimate the PV systolic pressure ($PPV_{,syst}$) from the average ratio of the two pressures from all other patients in our study. The nominal resistance values are calculated as

$$\bar{R}_{sys} = \frac{P_{SA,ave} - \bar{P}_{SV,syst}}{CO_{RHC}} \tag{2.45}$$

$$\bar{R}_{pul} = \begin{cases} \dfrac{P_{PA,ave} - \bar{P}_{PV,syst}}{CO_{RHC}} \\ if\ 0.975\ P_{PA,ave} \geq P_{PCW,ave} + \dfrac{2}{3}\ \bar{P}_{PV,pp} \\ \dfrac{P_{PA,syst} - \bar{P}_{PV,syst}}{CO_{RHC}} \\ if\ 0.975\ P_{PA,ave} < P_{PCW,ave} + \dfrac{2}{3}\ \bar{P}_{PV,pp} \end{cases} \quad (2.46)$$

All elastance parameters were approximated using the systolic pressure and stressed volume estimates as

$$E_{LV} = \frac{\bar{P}_{LV,syst}}{V_{LV,syst}} \quad (2.47)$$

$$E_{SA} = \frac{P_{SA,syst} - P_{SA,diast}}{\bar{V}_{SA,syst}} \quad (2.48)$$

$$\bar{E}_{SV} = \frac{\bar{P}_{SV,pp}}{\bar{V}_{SV,syst}} \quad (2.49)$$

$$\bar{E}_{RV} = \frac{P_{RV,syst}}{\bar{V}_{RV,syst}} \quad (2.50)$$

$$\bar{E}_{PA} = \frac{P_{PA,syst} - P_{PA,diast}}{\bar{V}_{PA,syst}} \quad (2.51)$$

$$\bar{E}_{PV} = \frac{P_{PV,pp}}{\bar{V}_{PV,syst}} \quad (2.52)$$

2.6.5 Calculation of Total Blood Volume

Total blood volume is calculated based on the height, weight, and sex of each patient as described in Colunga et al. (Colunga *et al.*, 2020), utilizing the expression originally developed by Nadler et al. (Nadler *et al.*, 1962). This total blood volume is comprised of stressed and unstressed volumes. The unstressed blood volume is the volume in each compartment at which the pressure is zero. The stressed volume is the difference between the total and unstressed volumes. The initial

distribution of stressed and unstressed blood volume among the six vascular compartments is based on the work by Beneken (Beneken & DeWit, 1967), in which a total stressed volume of 18.75% was assumed. In this study, we assumed 30% of the total blood volume is stressed volume (Colunga et al., 2020; Maas et al., 2012), so additional volume was recruited from the four systemic and pulmonary compartments based on the unstressed volume available in each compartment. Explicit details on determining patient-specific stressed volume for each model compartment can be found below and the model code (Carlson & Jones, n.d.).

A. Recalculation of Initial Volume Distributions

A recent theory with regards to HFpEF is that there is some dysfunction in the ability to adjust volume distribution in the cardiovascular system. Our model can take into consideration different percentages of total stressed volume which might vary across patients. Even though we have this option for the purpose of discriminating HFpEF phenotypes, we have fixed the total stressed volume at 30% of total blood volume. This still leaves us with the problem of how to estimate the initial volume distribution across compartments and to ensure the percentages of stressed volume in each compartment sum up to be 30% of total blood volume.

We start with the nominal values of stressed, unstressed, and total blood volume in each compartment from Beneken (Beneken & DeWit, 1967). The difference here is that Beneken's stressed volume distributions add up to be only 18.75%, which is now generally taken to be too low. In the code, we recalculate an initial stressed volume distribution to a 30% stressed volume that is appropriate. **Table 2.5** is a summary of blood volume distributions from Beneken.

Table 2.5 Blood volume distributions in mL adapted from Beneken (Beneken & DeWit, 1967)

Stressed		Unstressed		Total	
Left Atrium (LA)					
$V_{s,B,LA}$	50	$V_{u,B,LA}$	30	$V_{t,B,LA}$	80
Left Ventricle (LV)					
$V_{s,B,LV}$	125	$V_{u,B,LV}$	0	$V_{t,B,LV}$	125
Systemic arteries (SA)					
$V_{s,B,SA}$	160	$V_{u,B,SA}$	425	$V_{t,B,SA}$	585
Systemic veins (SV)					
$V_{s,B,SV}$	219	$V_{u,B,SV}$	2697	$V_{t,B,SV}$	2916
Right atrium (RA)					
$V_{s,B,RA}$	50	$V_{u,B,RA}$	30	$V_{t,B,RA}$	80
Right ventricle (RV)					
$V_{s,B,RV}$	125	$V_{u,B,RV}$	0	$V_{t,B,RV}$	125
Pulmonary arteries (PA)					
$V_{s,B,PA}$	69	$V_{u,B,PA}$	50	$V_{t,B,PA}$	119
Pulmonary veins (PV)					
$V_{s,B,PV}$	54	$V_{u,B,PV}$	460	$V_{t,B,PV}$	514
Totals					
$V_{s,B,tot}$	852	$V_{u,B,tot}$	3692	$V_{t,B,tot}$	4544

The total blood volume in Beneken is 4544 mL, which is different than the blood volume calculated for each patient. Therefore, we will estimate the percentages of stressed and unstressed volumes for different total stressed volume percentages with respect to the Beneken volumes and then use those percentages to calculate the initial volume distributions for the patient-specific total blood volume. We start by adjusting what volumes are stressed and unstressed in the heart. Beneken assumes 100% stressed volume in the ventricles and 60% stressed volume in the atria, which we change to 70% and 50% respectively. To adjust this, we calculate new volumes in the heart as

$$V^*_{s,B,LV} = 0.70\, V_{t,B,LV} \tag{2.53}$$

$$V^*_{s,B,RV} = 0.70 V_{t,B,RV} \tag{2.54}$$

We need to recruit volume over the Beneken values, and we assume that this recruited volume will come from only the systemic and pulmonary circulations and not from the heart. So, we take the Beneken stressed volumes and then subtract off the heart chamber stressed volumes as

$$V_{s,B,nh} = V_{s,B,tot} - V_{s,B,LV} - V_{s,B,RV}, \tag{2.55}$$

where the subscript *nh* denotes “non-heart".

To obtain a total stressed volume fraction of 30% for each patient, we have

$$V^*_{s,B,tot} = 0.30\, V_{t,B,tot}. \tag{2.56}$$

Then, we subtract off the new heart chamber stressed volumes as

$$V^*_{s,B,nh} = V^*_{s,B,tot} - V^*_{s,B,LV} - V^*_{s,B,RV}. \tag{2.57}$$

The difference between these stressed volumes is the amount of recruited volume over and above the Beneken stressed volumes, that is,

$$V_{s,R,tot} = V^*_{s,B,nh} - V_{s,B,nh}. \tag{2.58}$$

The recruited volume in each compartment is calculated based on the fraction of the unstressed volume in each compartment with respect to the total unstressed volume, $V_{u,B,tot}$, that is

$$V_{s,B,R,SA} = V_{s,R,tot}\left(V_{u,B,SA}/V_{u,B,tot}\right), \tag{2.59}$$

$$V_{s,B,R,SV} = V_{s,R,tot}\left(V_{u,B,SV}/V_{u,B,tot}\right), \tag{2.60}$$

$$V_{s,B,R,PA} = V_{s,R,tot}\left(V_{u,B,PA}/V_{u,B,tot}\right), and \tag{2.61}$$

$$V_{s,B,R,PV} = V_{s,R,tot}\left(V_{u,B,PV}/V_{u,B,tot}\right), \tag{2.62}$$

Adding these recruited volumes to the Beneken values will give the volumes with the desired 30% total stressed volume as

$$V^*_{s,B,SA} = V_{s,B,SA} + V_{s,B,R,SA}, \tag{2.63}$$

$$V^*_{s,B,SV} = V_{s,B,SV} + V_{s,B,R,SV}, \tag{2.64}$$

$$V^*_{s,B,PA} = V_{s,B,PA} + V_{s,B,R,PA}, and \tag{2.65}$$

$$V^*_{s,B,PV} = V_{s,B,PV} + V_{s,B,R,PV}. \tag{2.66}$$

Dividing these new volumes by the total compartment volumes from Beneken gives the fraction of stressed volume for each compartment, that is,

$$f_{VsB,SA} = V^*_{s,B,SA}/V_{t,B,SA}, \tag{2.67}$$

$$f_{VsB,SV} = V^*_{s,B,SV}/V_{t,B,SV}, \tag{2.68}$$

$$f_{VsB,PA} = V^*_{s,B,PA}/V_{t,B,PA}, \quad \text{and} \tag{2.69}$$

$$f_{VsB,PV} = V^*_{s,B,PV}/V_{t,B,PV}. \tag{2.70}$$

These fractions are used for the patient-specific total volume to get an initial stressed volume distribution across compartments assuming a 30% total stressed volume see **Table 2.6**.

Table 2.6 New blood volume distribution in mL with 30% volume.

Stressed		**Unstressed**		**Total**	
Left Atrium (LA)					
$V^*_{s,B,LA}$	40	$V^*_{u,B,LA}$	40	$V^*_{t,B,LA}$	80
Left Ventricle (LV)					
$V^*_{s,B,LV}$	88	$V^*_{u,B,LV}$	37	$V^*_{t,B,LV}$	125
Systemic arteries (SA)					
$V^*_{s,B,SA}$	230	$V^*_{u,B,SA}$	355	$V^*_{t,B,SA}$	585
Systemic veins (SV)					
$V^*_{s,B,SV}$	662	$V^*_{u,B,SV}$	2254	$V^*_{t,B,SV}$	2916
Right atrium (RA)					
$V^*_{s,B,RA}$	40	$V^*_{u,B,RA}$	40	$V^*_{t,B,RA}$	80
Right ventricle (RV)					
$V^*_{s,B,RV}$	88	$V^*_{u,B,RV}$	37	$V^*_{t,B,RV}$	125
Pulmonary arteries (PA)					
$V^*_{s,B,PA}$	77	$V^*_{u,B,PA}$	42	$V^*_{t,B,PA}$	119
Pulmonary veins (PV)					
$V^*_{s,B,PV}$	130	$V^*_{u,B,PV}$	384	$V^*_{t,B,PV}$	514
Totals					
$V^*_{s,B,tot}$	1355	$V^*_{u,B,tot}$	3189	$V^*_{t,B,tot}$	4544

In this study, the percent of stressed volume remains the same across all patients. However, regulation of stressed and unstressed volume is a current topic of discussion in the field of HF (Fallick et al., 2011; Fudim et al., 2017) Click or tap here to enter text.and the ability to change the ratio of stressed and unstressed volume can be explored in future studies.

2.6.6 Global Sensitivity Analysis

Since the inverse problem investigated here is ill posed, a sensitivity analysis is performed to assess the practical identifiability of the parameters, i.e., determine which of the parameters can be identified with the given clinical patient data. Due to the vast variation in parameter values across subjects, we conducted a global sensitivity analysis using Sobol' indices to explore the entire parameter space. Sobol' indices apportion the variance in the output to the effect of each parameter (Sobol′, 2001). In particular, we use total effect Sobol' indices to characterize the effect of both the parameter and parameter interactions on the residual variance (Randall E. B. *et al.*, 2021). All parameters were varied within their physiological bounds, listed in **Table 2.3**. The residual (**Equation** 2.83**)** was calculated by determining the least square error between simulations and RHC and TTE data in a similar fashion to that described in Colunga et al. (Colunga *et al.*, 2020). The Sobol' indices were calculated using Monte Carlo integration by computing $10^3(16+2) = 1.8\text{e}4$ model evaluations similar to the procedure described in Randall et al. (Randall E. B. *et al.*, 2021).

We then ranked the total effect Sobol' indices (**Figure 2.4**) to determine a set of influential parameters that substantially affect the variance of the residual, i.e., a subset of parameters that have an index above the threshold $\eta = 10^{-3}$. Parameters below the threshold were excluded from consideration for optimization and set to their nominal values. Though the parameters $P_{0,LV}$, $P_{0,RV}$,

and E_{SV} were above η, they are correlated to other parameters with a higher sensitivity and therefore cannot be determined explicitly (Colunga *et al.*, 2020). Hence, $P_{0,LV}$, and $P_{0,RV}$ were set to the values used in Colunga et al., and E_{SV} was calculated using **Equation** 2.49. Note that our previous study used only RHC data to determine model parameters. Since TTE data were included here, two additional model parameters could be identified: E_{LV} and E_{RV}. From the set of influential parameters, we obtained the subset

$$\theta = \lambda_{LV}, \lambda_{RV}, E_{LV}, E_{RV}, E_{SA}, E_{PA}, E_{PV},\ R_{sys}, R_{pul} \tag{2.71}$$

to optimize. This subset consists of parameters λ_{LV}, λ_{RV}, E_{LV}, and E_{RV}, which are used to describe cardiac function. All others are hemodynamic parameters that define cardiovascular function as a whole, which may be important for distinguishing particular subgroups of HFpEF. This methodology produced a subset of uncorrelated parameters that can be estimated for each patient. In particular, none of the parameters reached their physiological bounds when estimated, giving confidence that the parameter subset in **Equation** 2.71 is well prescribed to investigate the HF questions discussed here.

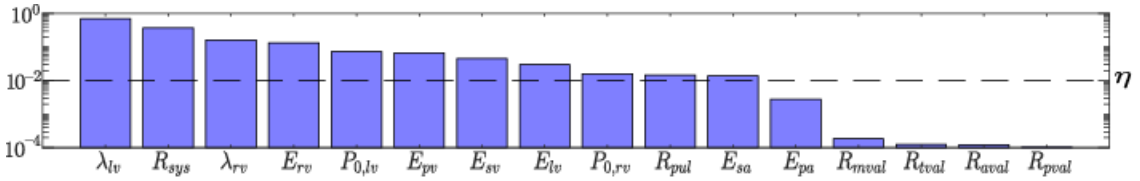

Figure 2.4 Global sensitivity analysis. Ranked total Sobol' indices for all 16 adjustable parameters with an index above the threshold $\eta = 10^{-2}$ were plotted with a log-scaled y-axis. This analysis shows that 12 parameters are influential to changes in the residual. From these parameters, we selected a subset of parameters to optimize, given in **Equation** 2.71.

A. Residual Equation Used for Sensitivity Analysis and Optimization

A residual function was used to assess parameter influence in our global sensitivity analysis and optimize model parameters to patient data. The change in this residual with changes in parameter values over a sampling of the entire parameter space is used to rank the sensitivity of each parameter with respect to each other. For optimization, a set of parameter values is found that minimizes the residual function producing a patient-specific model that most closely represents a given set of patient data. Two simulation runs are made to compute the residual: one at the RHC heart rate and the second at the TTE heart rate. The following equations show the eleven pressures, volumes, and cardiac output measures from these two simulations used to compute the eleven residuals between the simulation and clinical measures using an appropriate normalization for each residual:

$$P_{RV,syst}^{res} = \frac{\mid P_{RV,syst}^{sim} - P_{RV,syst}^{data} \mid}{P_{SA,syst}^{data}}, \tag{2.72}$$

$$P_{RV,diast}^{res} = \frac{\mid P_{RV,diast}^{sim} - P_{RV,diast}^{data} \mid}{P_{SA,syst}^{data}}, \tag{2.73}$$

$$P_{PA,syst}^{res} = \frac{\mid P_{PA,syst}^{sim} - P_{PA,syst}^{data} \mid}{P_{SA,syst}^{data}}, \tag{2.74}$$

$$P_{PA,diast}^{res} = \frac{\mid P_{PA,diast}^{sim} - P_{PA,diast}^{data} \mid}{P_{SA,syst}^{data}}, \tag{2.75}$$

$$P_{SA,syst}^{res} = \frac{\mid P_{SA,syst}^{sim} - P_{SA,syst}^{data} \mid}{P_{SA,syst}^{data}}, \tag{2.76}$$

$$P_{SA,diast}^{res} = \frac{\mid P_{SA,diast}^{sim} - P_{SA,diast}^{data} \mid}{P_{SA,syst}^{data}}, \tag{2.77}$$

$$P_{PCW,ave}^{res} = \frac{\mid P_{PCW,ave}^{sim} - P_{PCW,ave}^{data} \mid}{P_{SA,syst}^{data}}, \tag{2.78}$$

$$\mathrm{CO}_{\mathrm{RHC}}^{res} = \frac{\mid \mathrm{CO}_{\mathrm{RHC}}^{sim} - \mathrm{CO}_{\mathrm{RHC}}^{data} \mid}{\max\left(\mathrm{CO}_{\mathrm{RHC}}^{data}, \mathrm{CO}_{\mathrm{TTE}}^{data}\right)}, \tag{2.79}$$

$$V_{LV,syst}^{res} = \frac{\mid V_{LV,syst}^{sim} - V_{LV,syst}^{data} \mid}{V_{LV,syst}^{data}}, \tag{2.80}$$

$$V_{LV,diast}^{res} = \frac{\mid V_{LV,diast}^{sim} - V_{LV,diast}^{data} \mid}{V_{LV,syst}^{data}}, \tag{2.81}$$

$$\mathrm{CO}_{\mathrm{TTE}}^{res} = \frac{\mid \mathrm{CO}_{\mathrm{TTE}}^{sim} - \mathrm{CO}_{\mathrm{TTE}}^{data} \mid}{\max\left(\mathrm{CO}_{\mathrm{RHC}}^{data}, \mathrm{CO}_{\mathrm{TTE}}^{data}\right)}. \tag{2.82}$$

The residuals are then averaged with no additional weights as:

$$Res = \frac{\sum_{i=1}^{7} P_i^{res} + \sum_{j=1}^{2} \mathrm{CO}_j^{res} + \sum_{k=1}^{2} V_k^{res}}{11} \tag{2.83}$$

2.6.7 Optimization

For each patient, we estimate the adjustable parameters in **Equation** 2.71 by minimizing the least square error between the simulations and data for ten measurements: RV pressure in systole and diastole, PA pressure in systole and diastole, average PCW pressure, systemic artery pressure in systole and diastole, CO during RHC, LV volume in systole and diastole, and CO during TTE. Since the HR during RHC and TTE can be different, two separate simulations are run: one simulating the RHC and one simulating the TTE. However, both simulations are run with one set of parameter values with the assumption that the parameters representing cardiac function do not change appreciably across procedures for a single patient. Values of the clinical data are calculated over the cardiac cycle after the system has reached a steady state of pulsatile pressures

and flows. This is assured by allowing our simulations to run for 50 beats. Once this steady state is reached, the maximum and minimum values of the pressure and volume data of the last 5 beats are used to compute the total residual error. The PCW pressure and CO represent average values over the cardiac cycle; because of this, their values are averaged over the cardiac cycle before being compared to the TTE and RHC data. Estimates for the adjustable parameters are obtained using the genetic algorithm with a population size of 500 and a stall generation limit of 10 generations implemented in MATLAB (MathWorks Natick, Ma). All other specifications were set to their default MATLAB value. To check to see if the parameter space was explored adequately, we ran the optimization for each patient 10 times and observed a consistent residual across the best few runs. The run with the lowest cost was chosen for our final results. More details about MATLAB's implementation of the genetic algorithm can be found at mathworks.com.

2.7 Machine Learning

We utilized one classification and two different clustering techniques using the built-in MATLAB *k*-means and hierarchical clustering functions to group individuals within a population based on similar characteristics. In theory, patients within the same groups should share similar physiological characteristics. The clinical data and optimized parameter values were compiled into separate matrices where each row represents a given patient, and each column represents a clinical measure or optimized parameter value (**Table 2.1** and **Table 2.3**). Before any of the clustering methods are applied, each column is centered by subtracting the average of each column from each element in that column. Because our clinical data and optimized parameters had different units within their respective matrices, we normalized each clinical measure or parameter by its standard

deviation. To mitigate any bias in these analyses, no additional weighting is placed on any of the clinical measurements or optimized parameters.

2.7.1 Principal component analysis (PCA)

We performed a PCA (Jolliffe IT, 1986), which is simply a singular value decomposition identifying an orthogonal change of basis within the clinical data or optimized parameter spaces that retains the greatest variation across patients, independent of the level of dimension reduction selected. For the optimized parameter matrix P, the decomposition $P = USV^T$ produces unitary matrices U and V and diagonal matrix S, representing the portion of the total variation explained by each principal component. The PCA score, which gives the position in this rotated space that maximizes variation, is given by the product of U and S. We plot the two-dimensional space of the first two principal components describing more than 50% of the total variance. Subsequent principal components each accounted for less than 15% of the total variance and are not plotted for clarity. A convex hull was prescribed about the HFpEF and HFrEF groups. HFpEF patients are then assigned a group based on the following clustering methods.

2.7.2 k-means Clustering

k-means clustering creates k unsupervised clusters from the data. In this study, we chose to group the patients into two clusters, that is, two patients are randomly chosen as cluster centroids, and all other patients are grouped relative to their L_1-distance from each centroid. This method is dependent on the random initial cluster centroids selected, so we run this process 20 times and select the clustering result that has the smallest total cluster variance (Eisen *et al.*, 1998; Wilkin & Huang, 2008). **Figure 2.6B** shows the two k-means clusters of the clinical data superimposed on the PCA hulls.

2.7.3 Hierarchical Clustering

In this clustering method, each patient starts as a cluster, and then the two closest patients are grouped together. This process is repeated, grouping the two closest clusters together to reduce the total number of clusters by 1 until all the patients are in one cluster (Kraskov *et al.*, 2005). This method forms a hierarchical cluster tree known as a dendrogram that can then be truncated to produce the desired number of clusters. To do this in MATLAB, the linkage function is used and the Ward metric (Ward, 1963) is selected to group the two clusters together at each step that minimize the total in-cluster variation. Using the dendrogram, we partitioned our patients into two clusters by cutting the dendrogram halfway between the second-from-last and last linkages. **Figure 2.6C** superimposes the hierarchical clusters of the clinical data on the PCA hulls.

Our focus is to identify groups that cluster consistently among these methods, especially since they use different concepts to group the data. If two HFpEF patients share a PCA hull region, a k-means cluster, and a hierarchical cluster, they are included in the same group. Since our purpose here is to subdivide only the HFpEF patients all HFrEF patients are grouped according to their clinical diagnosis independent of whether they may cluster with HFpEF in one of the clustering methods used. The clusters with the most HFrEF patients are considered the most "HFrEF-like". Patients that switch between clusters for different methods are deemed not consistently clustered (NCC).

To classify the HFpEF patients that fall in the PCA overlap region, we rely on the clustering methods. If a HFpEF patient in the overlap region falls in the k-means and hierarchical clusters that contain a majority of the HFrEF patients, we classify them as HFrEF-like HFpEF and thus are part of HFpEF1. Conversely, if they fall in the k-means and hierarchical clusters that contain a

majority of HFpEF patients, we classify them as “pure” HFpEF and are part of HFpEF2. If they switch between clusters, they are classified as NCC.

2.8 Results

2.8.1 HF Subgroups Determined From Clinical Data

Our retrospective cardiovascular systems analysis consists of a cohort of 31 patient records (10 HFrEF and 21 HFpEF). First, we consider the clinical data explicitly from the RHC and TTE **(Figure 2.5)**. Statistically significant differences in the means of TTE derived measurements (p-value < 0.001) such as EF, systolic & diastolic LV volumes, and CO (p-value < 0.01) are found between HFrEF and HFpEF patients **(Figure 2.5A-D)**. Consistent with their systolic dysfunction phenotype, HFrEF patients have greater ventricular volumes than the HFpEF cohort, with patients 1 and 6 showing particularly extreme ventricular dilation **(Figure 2.5B** and **C)**. In the HFpEF cohort, pulmonary artery systolic and diastolic pressures as well as RV systolic pressures are significantly higher (p-value < 0.01) than the HFrEF cohort **(Figure 2.5E-G)**. Systolic arterial pressure is likewise significantly higher (p-value < 0.05) in the HFpEF cohort when compared to HFrEF patients (**Figure 2.5H)**.

To determine if novel subgroups of HF patients with similar cardiovascular etiologies could be discerned from clinical data alone, we perform a PCA along with two unsupervised clustering methods on the clinical data available from the RHC and TTE (**Figure 2.6**). All RHC and TTE patient data to which the model was optimized **(Table 2.1)** except EF, height, and weight were included in the PCA. Since EF was a major factor used to determine clinical diagnosis and LV diastolic and systolic volumes are already included in the PCA analysis, EF was excluded. In **Figure 2.6A**, PCA scores for the first and second principal components are plotted, and convex

hulls are drawn around each diagnosis. The first two principal components of our clinical data PCA describe 52% of the total variance. The convex hulls for HFrEF (orange) and HFpEF (blue) overlap, consisting of HFrEF patients 2, 4, 5, 7, and 9 and HFpEF patients 11, 24, and 18. As PCA only captures the greatest variance across all patients, the HFpEF patients in the overlap region required further analysis.

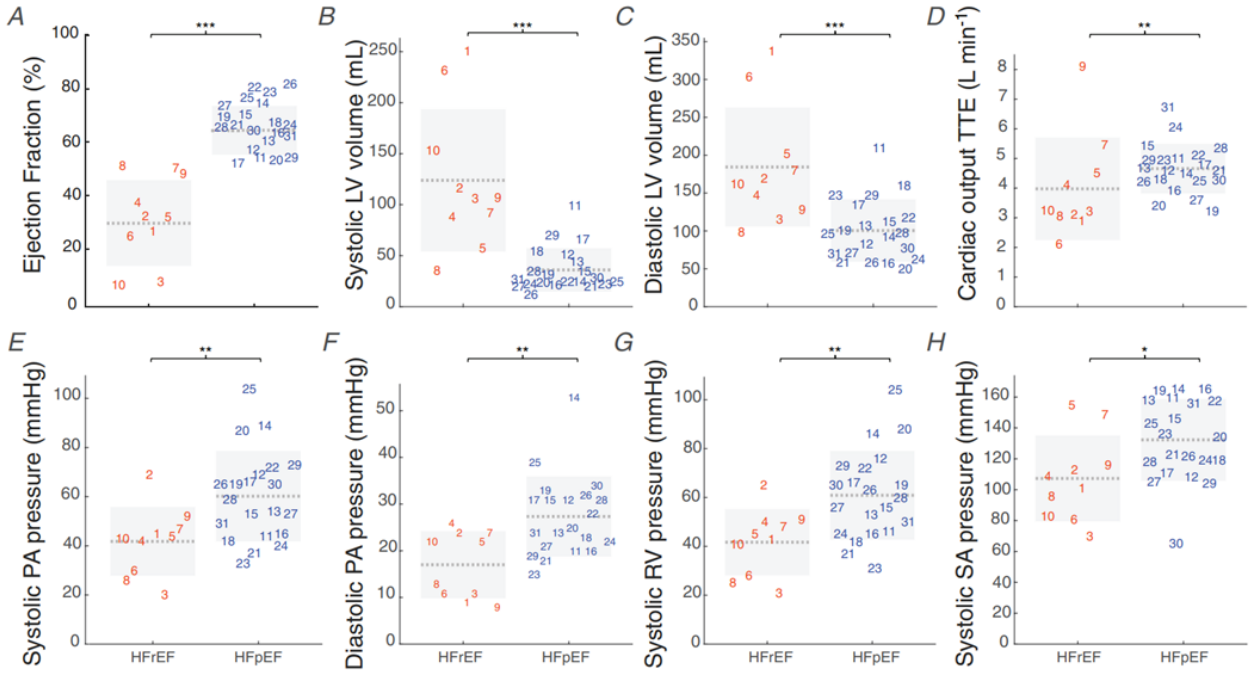

Figure 2.5 Box plots of clinical data with significant differences between heart failure patients based on their HFrEF and HFpEF diagnosis. A. Ejection fraction (%). B. Systolic left ventricular (LV) volume (mL). C. Diastolic LV volume (mL). D. Cardiac output (L min^{-1}) from the TTE data. E. Systolic pulmonary arterial (PA) pressure (mmHg). F. Diastolic PA pressure (mmHg). G. Systolic right ventricular (RV) pressure (mmHg). H. Systolic systemic arterial (SA) pressure (mmHg). The light gray dashed line denotes the group average, and the grey box contains one standard deviation above and below the mean of each clinical value (*p-value <0.05, **p-value <.01, ***p-value <.001).

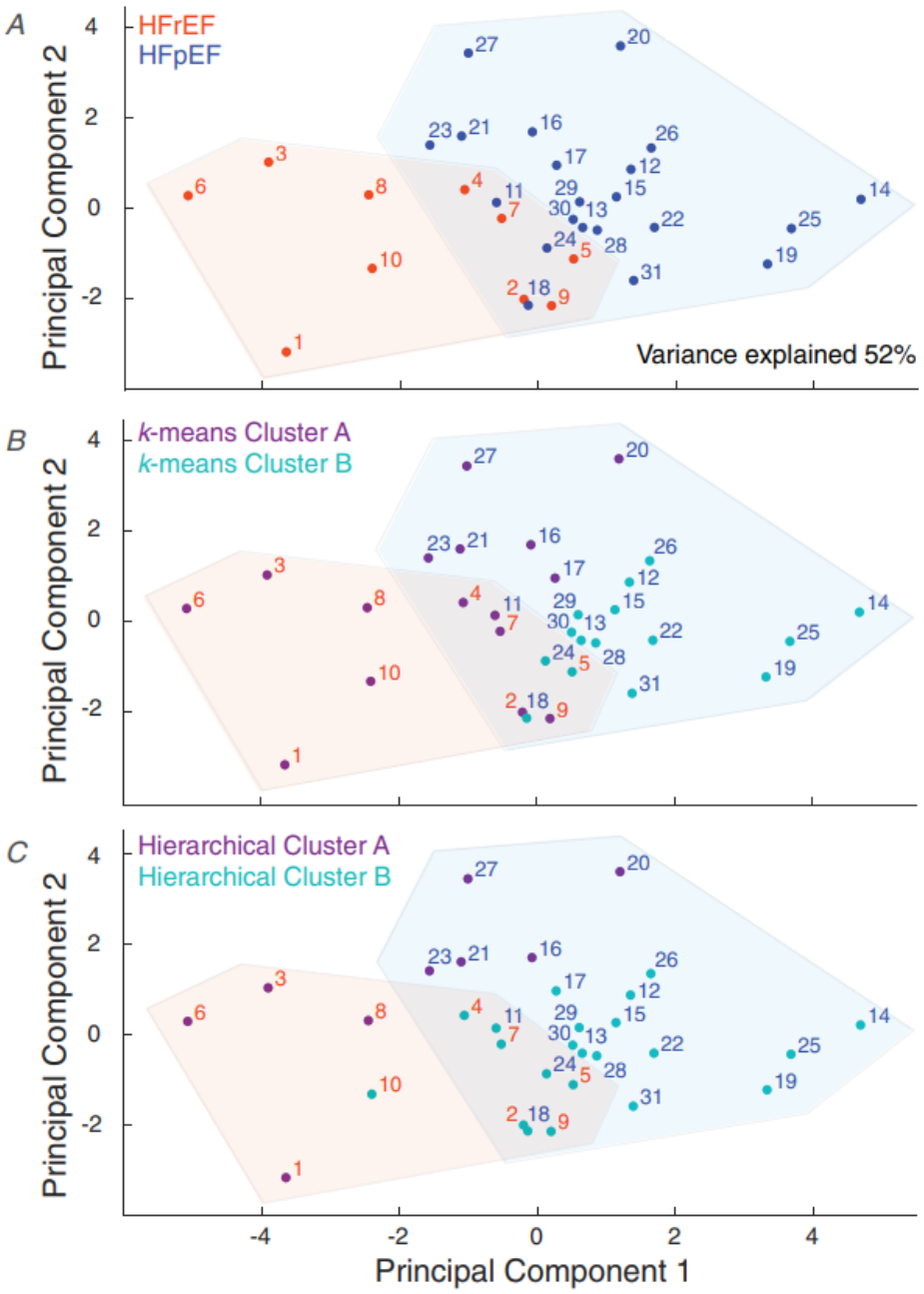

Figure 2.6 Clustering analysis of clinical data. **A.** Principal component analysis (PCA) of the clinical data. Convex hulls for the HFrEF (orange) and HFpEF (blue) patients are determined by individual patient diagnosis. **B.** *k*-means clustering of patient data superimposed on the PCA hulls where cluster A (purple) is more HFrEF-like and cluster B (teal) is more HFpEF-like. **C.** Hierarchical clustering of patient data superimposed on the PCA hulls where cluster A (purple) is more HFrEF-like and cluster B (teal) is more HFpEF-like.

To test if we could attribute the HFpEF patients that fall in the PCA overlap region into a distinct phenotype associated with the HFrEF or HFpEF clinical groups, we employ k-means and hierarchical clustering (**Figure 2.6B** and **C**). We superimpose the k-means clusters on the PCA convex hulls (**Figure 2.6B)**. Since all HFrEF patients except patient 5 fall into k-means cluster A, we designate cluster A as more HFrEF-like and, conversely, k-means cluster B as more HFpEF-like. We observe in the overlap region, HFpEF patient 11 is in k-means cluster A whereas patients 18 and 24 are k-means cluster B. Also, HFrEF patient 5 falls in k-means cluster B. Lastly, HFpEF patients 16, 17, 20, 21, 23, and 27 fall into k-means cluster A. In a similar fashion, hierarchical clustering results are superimposed on the PCA convex hull (**Figure 2.6C)**. Similarly, we specified hierarchical cluster A as more HFrEF-like and hierarchical cluster B as more HFpEF-like. Of particular interest is that all HFpEF patients in the overlap region now fall in hierarchical cluster B. Details of the patient designation based on the clinical measurement clustering analysis are given in **Table 2.7**. Among the clustering methods used here, **Table 2.8** denotes which patients consistently cluster in the following groups: "pure" HFrEF ($n = 10$) - patients that fall in the HFrEF PCA hull. "pure" HFpEF ($n = 13$) - patients that fall in the HFpEF PCA hull, k-means cluster B, and hierarchical cluster B. NCC ($n = 8$) - patients that do not consistently cluster. Note that this methodology shows no subgroups of HFpEF. Also, almost half of the HFpEF patients fall in the NCC designation.

HFrEF patients 1 and 6 show extreme ventricular dilation compared to other HFrEF patients in this cohort with large systolic and diastolic volumes (outliers in **Figure 2.5B** and **C)**. Therefore, these patients were excluded from further analysis.

Table 2.7 Clinical data cluster classification.

Patient	Hull Location	*k*-means Cluster	Hierarchical Cluster	Group
HFrEF				
1	HFrEF	A	A	HFrEF
2	HFrEF	A	B	HFrEF
3	HFrEF	A	A	HFrEF
4	HFrEF	A	B	HFrEF
5	HFrEF	B	B	HFrEF
6	HFrEF	A	A	HFrEF
7	HFrEF	A	B	HFrEF
8	HFrEF	A	A	HFrEF
9	HFrEF	A	B	HFrEF
10	HFrEF	A	B	HFrEF
HFpEF				
11	HFpEF	A	B	NCC
12	HFpEF	B	B	HFpEF
13	HFpEF	B	B	HFpEF
14	HFpEF	B	B	HFpEF
15	HFpEF	B	B	HFpEF
16	HFpEF	A	A	NCC
17	HFpEF	A	B	NCC
18	HFpEF	B	B	HFpEF
19	HFpEF	B	B	HFpEF
20	HFpEF	A	A	NCC
21	HFpEF	A	A	NCC
22	HFpEF	B	B	HFpEF
23	HFpEF	A	A	NCC
24	HFpEF	B	B	HFpEF
25	HFpEF	B	B	HFpEF
26	HFpEF	B	B	HFpEF
27	HFpEF	A	A	NCC
28	HFpEF	B	B	HFpEF
29	HFpEF	B	B	HFpEF
30	HFpEF	B	B	HFpEF
31	HFpEF	B	B	HFpEF

HFrEF – heart failure with reduced ejection fraction.
HFpEF – heart failure with preserved ejection fraction.
NCC - not consistently clustered.

Table 2.8 Patient classification from clustering results based on clinical data (left) and optimized parameters (right).

Clinical data			Optimized parameters			
HFrEF	**HFpEF**	**NCC**	**HFrEF**	**HFpEF1**	**HFpEF2**	**NCC**
1	12	11	2	11	12	13
2	13	16	3	17	14	15
3	14	17	4	18	16	22
4	15	18	5	29	19	23
5	19	20	7	30	20	28
6	22	21	8		21	
7	24	23	9		24	
8	25	27	10		25	
9	26				26	
10	28				27	
	29				31	
	30					
	31					

HFrEF – heart failure with reduced ejection fraction.
HFpEF – heart failure with preserved ejection fraction.
NCC – not consistently clustered.

2.8.2 HF Subgroups Determined From Optimized Parameter Values

To learn about the underlying physiological differences between our patient cohorts that cannot be determined from clinical data alone, patient clinical measurements are used to parameterize a simplified cardiovascular systems model. We conduct a global sensitivity analysis exploring the entire permissible parameter space and ranked the parameters due to their contribution to the residual. **Figure 2.4** displays the ranked total Sobol' indices for all 16 adjustable parameters. This analysis shows that 12 parameters are influential to the residual from which we selected a subset of 9 parameters to optimize **(Equation** 2.71**)**. Optimized parameter values for each patient are listed in **Table 2.9**.

Our model simulations predict that the HFpEF cohort has a much wider distribution of the parameter values than the HFrEF cohort. We perform the same methods applied to the clinical data

to the optimized parameter values to see if in the parameter space we could identify subgroups of HFpEF patients with similar cardiovascular etiologies **(Figure 2.6)**. The first two principal components of our optimized parameter PCA describe 59% of the total variance. Since the clinical data and parameter space are two entirely different representations of the patient population no conclusion should be drawn from the fact that both PCA analyses represent an equivalent total variance for the first two principal components.

The PCA scores of the optimized parameters show that HFpEF patients 11, 17, 18, 29 and 30 fall in the PCA overlap region **(Figure 2.7A)**. We conducted k-means (**Figure 2.7B**) and hierarchical (**Figure 2.7C**) clustering on the optimized parameters revealing a much different structure than clustering based on raw clinical data alone. In both clustering methods, the majority of the HFrEF patients fell into one cluster, which we designate as cluster A (all HFrEF patients except 2 and 9 are in k-means cluster A whereas all HFrEF patients are in hierarchical cluster A). Notably, all HFpEF patients in the overlap region also fall into cluster A for both methods. Therefore, we conclude that this is a distinct HFpEF subpopulation. Details about the hull location and clustering for each patient based on the optimized parameter values are shown in **Table 2.10**.

Table 2.8 shows that this independent analysis with PCA, k-means clustering, and hierarchical clustering on the optimized parameter values reveals that the 29 patients fall into distinct groups: HFrEF ($n = 8$) - patients that fall in the HFrEF PCA hull. HFpEF1 ($n = 5$) - HFpEF patients that fall in the PCA overlap region, k-means cluster A, and hierarchical cluster A. HFpEF2 ($n = 11$) - HFpEF patients that fall in the HFpEF PCA hull, k-means cluster B, and hierarchical cluster B. NCC ($n = 5$) - HFpEF patients that do not consistently cluster.

Table 2.9 Patient-specific optimized parameter values.

Patient		E_{LV}	λ_{LV}	E_{RV}	λ_{RV}	E_{PA}	E_{PV}	R_{pul}	E_{SA}	R_{sys}
HFrEF	**2**	1.09	0.04	4.09	0.07	2.18	0.09	0.24	0.93	1.53
	3	0.78	0.03	0.37	0.03	0.70	0.07	0.02	0.67	1.03
	4	1.33	0.04	2.49	0.05	0.40	0.06	0.14	1.09	1.21
	5	1.96	0.03	0.76	0.03	2.99	0.10	0.03	0.88	1.25
	7	1.63	0.03	0.37	0.02	0.46	0.02	0.11	1.49	1.05
	8	2.88	0.04	0.48	0.01	0.24	0.01	0.17	0.54	1.05
	9	1.15	0.04	1.14	0.05	2.61	0.09	0.19	1.84	1.92
	10	0.65	0.03	0.36	0.01	0.73	0.02	0.11	0.68	1.37
	Mean	1.44	0.04	1.26	0.03	1.29	0.06	0.13	1.02	1.30
	Median	1.24	0.04	0.62	0.03	0.72	0.07	0.13	0.91	1.23
	SD	0.68	0.00	1.27	0.02	1.04	0.03	0.07	0.42	0.29
HFpEF1	**11**	1.73	0.03	2.98	0.03	0.49	0.03	0.06	1.14	0.94
	17	1.77	0.04	1.39	0.02	2.12	0.02	0.08	0.97	1.04
	18	1.52	0.03	0.45	0.02	0.62	0.08	0.03	0.75	0.72
	29	1.49	0.04	1.57	0.03	2.74	0.09	0.11	0.71	0.85
	30	2.39	0.07	1.43	0.01	1.19	0.04	0.11	0.89	0.69
	Mean	1.78	0.04	1.56	0.02	1.43	0.05	0.08	0.89	0.85
	Median	1.73	0.04	1.43	0.02	1.19	0.04	0.08	0.89	0.85
	SD	0.32	0.02	0.81	0.01	0.87	0.03	0.03	0.15	0.13
HFpEF2	**12**	2.55	0.06	1.77	0.05	1.29	0.05	0.74	1.02	1.90
	14	6.84	0.06	1.31	0.03	0.65	0.10	0.59	1.36	1.50
	16	8.65	0.09	2.16	0.05	0.89	0.02	0.29	3.16	2.70
	19	5.38	0.06	1.09	0.03	1.11	0.10	0.05	1.34	1.39
	20	7.67	0.08	2.00	0.04	1.75	0.03	1.00	2.07	2.13
	21	6.11	0.09	1.01	0.03	0.73	0.02	0.17	2.01	2.11
	24	5.77	0.07	1.20	0.05	0.60	0.10	0.30	1.33	1.51
	25	5.63	0.07	3.13	0.05	2.18	0.10	0.29	1.38	1.39
	26	9.99	0.09	3.40	0.06	0.88	0.10	0.32	1.29	1.72
	27	5.60	0.06	2.21	0.01	0.77	0.01	0.45	1.15	1.67
	31	5.68	0.08	3.19	0.07	1.90	0.03	0.08	2.26	1.81
	Mean	6.35	0.07	2.04	0.04	1.16	0.06	0.39	1.67	1.80
	Median	5.77	0.07	2.00	0.05	0.89	0.05	0.30	1.36	1.72
	SD	1.85	0.01	0.84	0.02	0.52	0.04	0.27	0.61	0.38
NCC	**13**	3.58	0.05	0.07	0.10	0.91	0.04	0.11	1.97	1.18
	15	4.30	0.05	2.74	0.04	0.42	0.05	0.14	1.21	1.12
	22	6.69	0.05	3.26	0.04	0.89	0.04	0.15	1.36	1.02
	23	6.32	0.04	0.62	0.02	0.26	0.03	0.09	1.08	0.95
	28	3.40	0.06	4.48	0.06	0.74	0.10	0.44	0.86	1.34
	Mean	4.86	0.05	2.23	0.05	0.64	0.05	0.19	1.30	1.12
	Median	4.30	0.05	2.74	0.04	0.74	0.04	0.14	1.21	1.12
	SD	1.38	0.00	1.65	0.03	0.26	0.03	0.13	0.38	0.13

HFrEF – heart failure with reduced ejection fraction. HFpEF – heart failure with preserved ejection fraction. NCC – not consistently clustered.

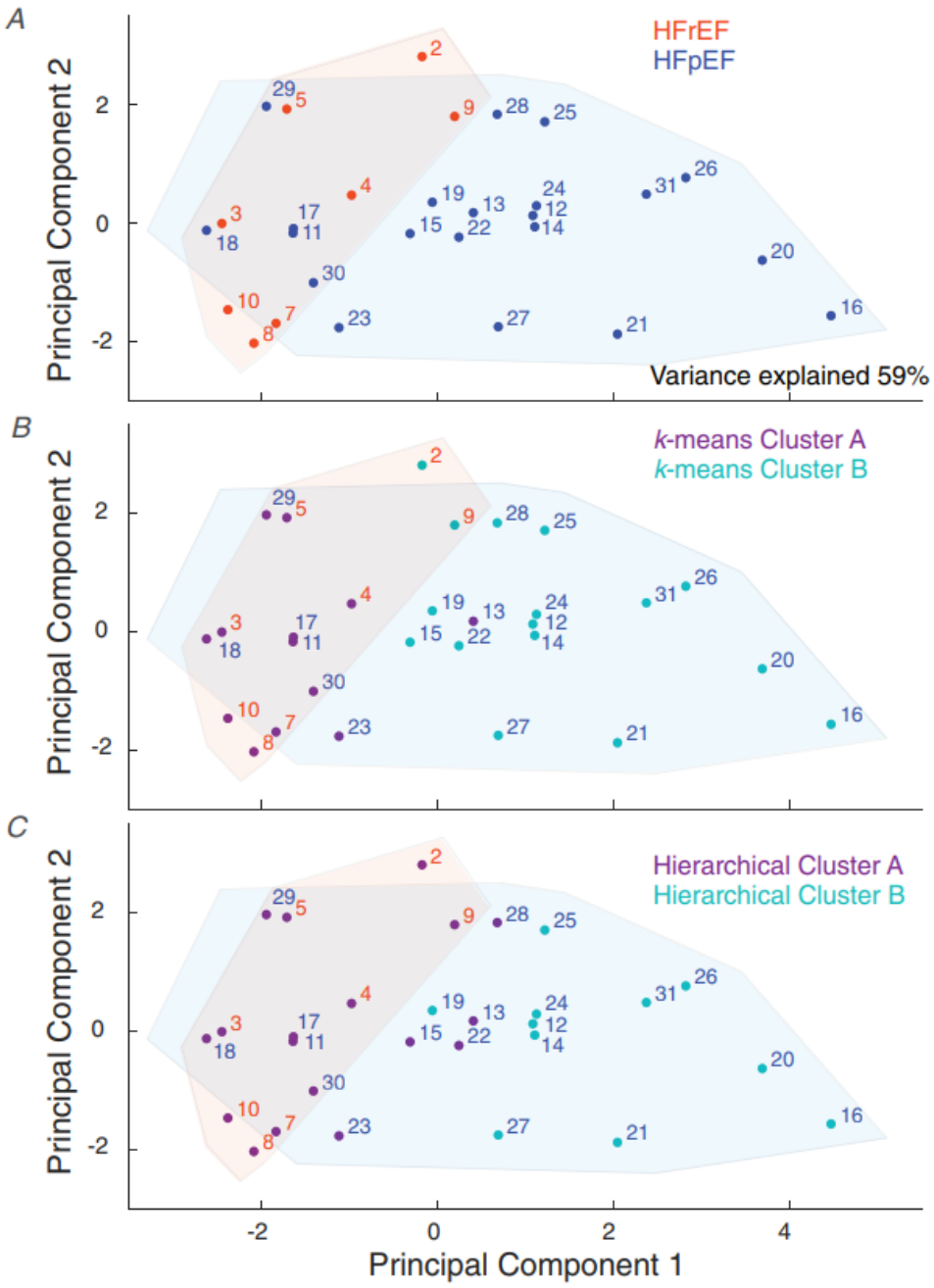

Figure 2.7 Clustering analysis of optimized model parameter values. This analysis determines three distinct groups of HFpEF patients. **A.** Principal component analysis (PCA) of the optimized model parameters. Convex hulls for the HFrEF (orange) and HFpEF (blue) patients are determined by individual patient diagnosis. **B.** *k*-means clustering of optimized parameter values superimposed on the PCA hulls where cluster A (purple) is more HFrEF-like and cluster B (teal) is more HFpEF-like. **C.** Hierarchical clustering of optimized parameter values superimposed on the PCA hulls where cluster A (purple) is more HFrEF-like and cluster B (teal) is more HFpEF-like.

Table 2.10 Optimized parameter cluster classification

Patient	Hull Location	*k*-means Cluster	Hierarchical Cluster	Group
HFrEF				
1	HFrEF	B	A	HFrEF
2	HFrEF	A	A	HFrEF
3	HFrEF	A	A	HFrEF
4	HFrEF	A	A	HFrEF
5	HFrEF	A	A	HFrEF
6	HFrEF	A	A	HFrEF
7	HFrEF	A	A	HFrEF
8	HFrEF	A	A	HFrEF
9	HFrEF	B	A	HFrEF
10	HFrEF	A	A	HFrEF
HFpEF				
11	HFrEF	A	A	HFpEF1
12	HFpEF	B	B	HFpEF2
13	HFpEF	A	A	NCC
14	HFpEF	B	B	HFpEF2
15	HFpEF	B	A	NCC
16	HFpEF	B	B	HFpEF2
17	HFrEF	A	A	HFpEF1
18	HFrEF	A	A	HFpEF1
19	HFpEF	B	B	HFpEF2
20	HFpEF	B	B	HFpEF2
21	HFpEF	B	B	HFpEF2
22	HFpEF	B	A	NCC
23	HFpEF	A	A	NCC
24	HFrEF	B	B	HFpEF2
25	HFpEF	B	B	HFpEF2
26	HFpEF	B	B	HFpEF2
27	HFpEF	B	B	HFpEF2
28	HFpEF	B	A	NCC
29	HFrEF	A	A	HFpEF1
30	HFrEF	A	A	HFpEF1
31	HFpEF	B	B	HFpEF2

HFrEF – heart failure with reduced ejection fraction. HFpEF – heart failure with preserved ejection fraction. NCC – not consistently clustered.

Since HFpEF1 shares most of the characteristics of the pure HFrEF group, we consider this group as more HFrEF-like, whereas HFpEF2 is "purely" HFpEF. All of the patients belonging to NCC are HFpEF patients.

2.8.3 Analysis of the Optimized Parameter Values From the 4 HF Subgroups

Figure 2.8 illustrates the patient-specific values of key model parameters representing LV active contractility (E_{LV}), LV passive stiffness (λ_{LV}), systemic arterial stiffness (E_{SA}), and systemic (R_{sys}) and pulmonary (R_{pul}) resistance when broken out into the parameter-based HFrEF and HFpEF groups. Parameter values that indicate normal cardiovascular function (listed in **Table 2.3**) are indicated by the dotted lines, and all parameter values are normalized to these values in **Figure 2.8**. When comparing E_{LV} **(Figure 2.8A)**, HFrEF and HFpEF1 tend to be below normal and HFpEF2 and NCC above normal. **(Table 2.11)**. When compared to both HFrEF and HFpEF1, HFpEF2 (p-value < 0.001) and NCC (p-value < 0.001) show significantly higher E_{LV}. No significant differences were found between HFrEF and HFpEF1, whereas HFpEF2 had a significantly higher E_{LV} when compared to NCC (p-value < 0.05).

When comparing λ_{LV} **(Figure 2.8B),** all groups have above normal levels when compared to normal **(Table 2.11)**. Although no significant differences were observed between HFrEF and HFpEF1, both groups have above normal values where λ_{LV} in HFpEF1 is double the normal value. HFpEF2 and NCC have a λ_{LV} almost triple the normal value **(Table 2.11)**. When compared to both HFrEF and HFpEF1, HFpEF2 shows significantly higher λ_{LV} (p-value < 0.001). NCC has higher λ_{LV} when compared to HFrEF (p-value < 0.001). HFpEF2 had a significantly higher λ_{LV} when compared to NCC (p-value < 0.01).

Looking at E_{SA} **(Figure 2.8C)**, both HFrEF and HFpEF1 are near normal whereas HFpEF2 and NCC are above normal **(Table 2.11)**. HFpEF2 shows significantly higher E_{SA} when compared to both HFrEF (p-value < 0.05) and HFpEF1 (p-value < 0.05). No significant differences were observed between HFrEF and HFpEF1. Likewise, no significant differences were observed between NCC and HFpEF2.

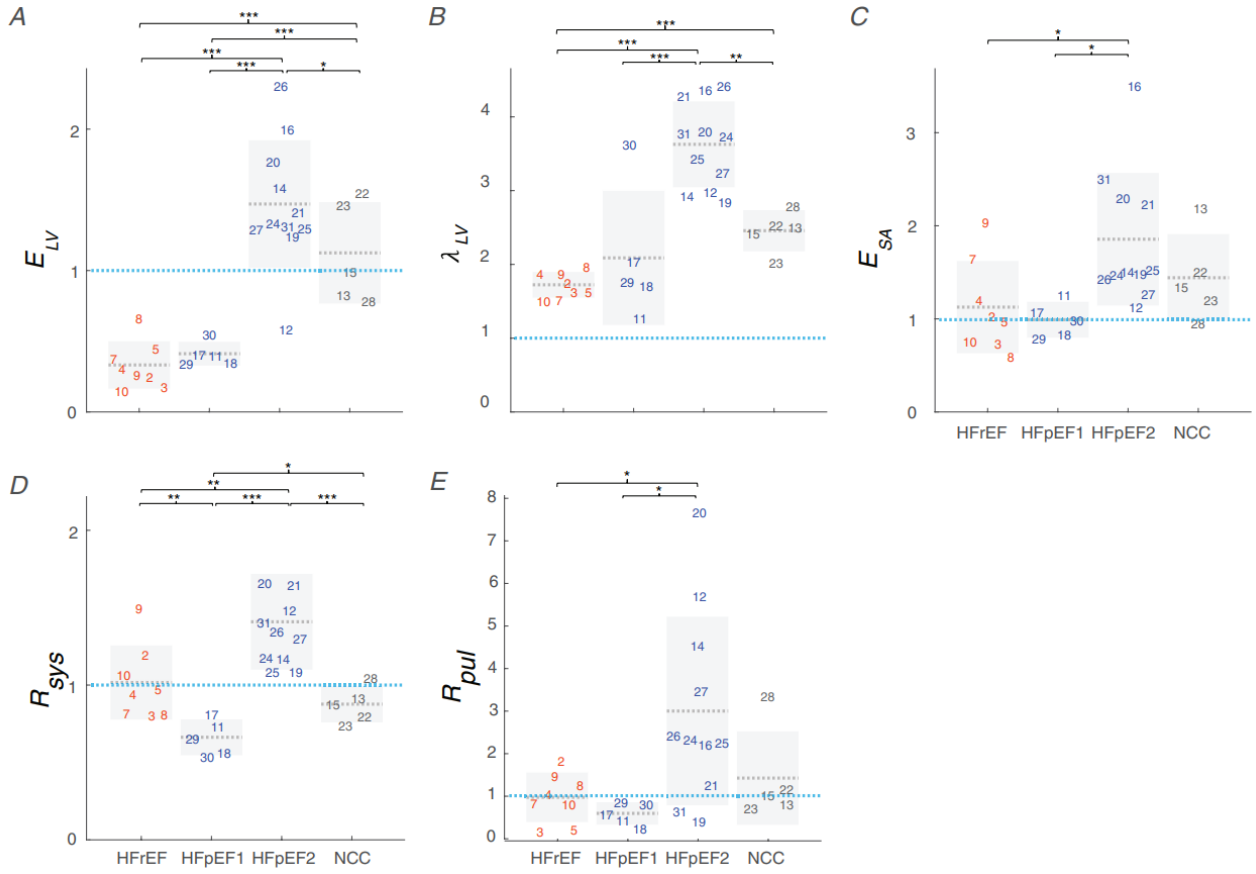

Figure 2.8 Box plots of the optimized parameter values with 4 heart failure groups. Analysis of the optimized parameters gives us an understanding of the mechanistic differences between the three HFpEF groups that cannot be seen by analyzing the clinical data alone. **A.** Left ventricular (LV) active contractility (E_{LV}, mmHg mL^{-1}). **B**. LV passive stiffness (λ_{LV}, mL^{-1}). **C**. Systemic arterial (SA) stiffness (E_{SA}, mmHg mL^{-1}). **D**. Systemic resistance (R_{sys}, mmHg s mL^{-1}). **E**. Pulmonary resistance (R_{pul}, mmHg s mL^{-1}). All values are plotted relative to the normal model values given in **Table 2.3**, indicated by the horizontal dashed blue line. The light gray dashed line denotes the average, and the gray box contains one standard deviation above and below the mean of each parameter value (*p-value <0.05, **p-value <0.01, ***p-value <0.001).

Table 2.11 Subgroup optimized parameter mean values compared to model-based norms listed in **Table 2.3**.

Subgroup	E_{LV}	λ_{LV}	E_{RV}	λ_{RV}	E_{PA}	E_{PV}	R_{pul}	E_{SA}	R_{sys}
HFrEF	0.3	1.7	1.8	1.7	5.0	5.7	1.0	1.1	1.0
HFpEF1	0.4	2.1	2.2	1.2	5.5	5.2	0.6	1.0	0.7
HFpEF2	1.5	3.6	2.9	2.1	4.5	5.9	3.0	1.9	1.4
NCC	1.1	2.5	3.2	2.6	2.5	5.0	1.4	1.4	0.9

HFrEF – heart failure with reduced ejection fraction.
HFpEF – heart failure with preserved ejection fraction.
NCC – not consistently clustered.

Strikingly, R_{sys} **(Figure 2.8D)** in both HFrEF and NCC are normal, whereas it is decreased in HFpEF1 and increased in HFpEF2 **(Table 2.11)**. This is the only parameter in which significant differences are observed between HFrEF and HFpEF1 (p-value < 0.01). HFpEF2 shows significantly higher R_{sys} when compared to HFrEF (p-value < 0.01), HFpEF1 (p-value < 0.001), and NCC (p-value < 0.001). NCC shows significantly higher R_{sys} when compared to HFpEF1 (p-value < 0.05).

Of note, R_{pul} is normal in HFrEF and reduced by almost half in HFpEF1 whereas it is increased in the HFpEF2 and NCC **(Table 2.11)**. HFpEF2 shows significantly higher levels of R_{pul} when compared to HFrEF (p-value < 0.05), and HFpEF1 (p-value < 0.05) **(Figure 2.8E)**. No significant differences were observed between HFrEF and HFpEF1. Likewise, no significant differences were observed between NCC and HFpEF2.

These results show that the main cardiac parameters influencing both HFrEF and HFpEF1 are reduced E_{LV} and slightly elevated λ_{LV} **(Figure 2.8A** and **B)**, indicating that systolic dysfunction is the primary driver for both patient cohorts. Consistent with the classical definition of HFpEF characterized by diastolic dysfunction, our simulations show that HFpEF2 has significantly increased λ_{LV} and E_{LV} at rest **(Figure 2.8A** and **B)**. When compared to model-based norms,

HFpEF2 and NCC show elevated E_{SA} and R_{pul} **(Figure 2.8C** and **Table 2.11)**, and HFpEF2 has an elevated R_{sys} **(Figure 2.8D).** Strikingly, HFpEF1 shows reduced levels of both R_{pul} and R_{sys}, whereas HFrEF patients show near normal levels of R_{sys}, R_{pul}, and E_{SA} **(Figure 2.8 C-E** and **Table 2.11)**.Taken together, these results stress that changes in the systemic and pulmonary vasculature coupled with changes in cardiac function paint a more complete picture of the cardiovascular state of HFpEF patients.

2.8.4 Analysis of the Clinical Data From the 4 HF Subgroups

Using the 4 HF subgroups, we reanalyze the patient RHC and TTE clinical data (**Figure 2.9**) between groups. The EF between the HF groups reveals very significant differences between all distinct HF subgroups (**Figure 2.9**). The EF in HFpEF1 is still significantly higher (p-value < 0.01) than that of the HFrEF cohort even though they are the most HFrEF-like. As expected, the EF in HFpEF2 and NCC are significantly higher (p-value < 0.001) than the HFrEF cohort. Of note, the different HFpEF groups have an EF above 50%, consistent with their HFpEF diagnosis yet significant differences amongst EF between HFpEF subgroups are observed. Although no significant differences were found between HFpEF2 and NCC, the HFpEF2 and NCC have a significantly higher EF (p-value < 0.05) than HFpEF1.

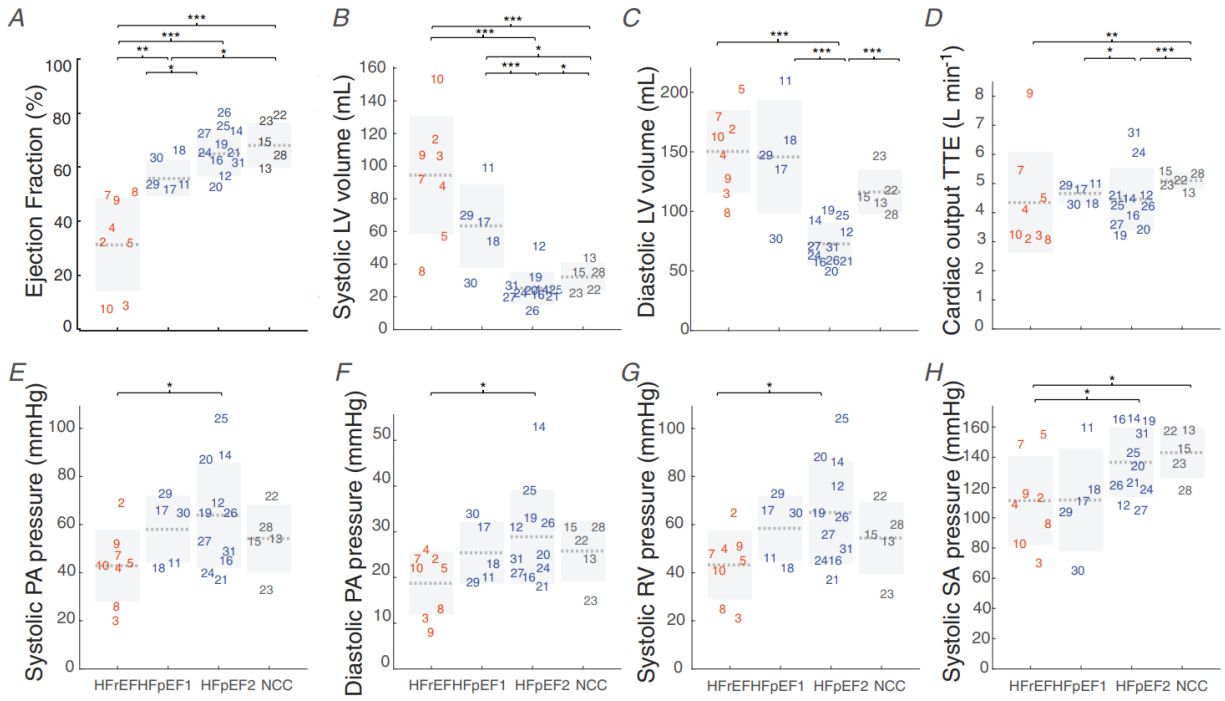

Figure 2.9 Box plots of the clinical data with 4 heart failure groups with significant differences between heart failure patients based on their HFrEF and HFpEF diagnosis. **A.** Ejection fraction (%). **B.** Systolic left ventricular (LV) volume (mL). **C.** Diastolic LV volume (mL). **D.** Cardiac output (L min^{-1}) from the TTE data. **E.** Systolic pulmonary arterial (PA) pressure (mmHg). **F.** Diastolic PA pressure (mmHg). **G.** Systolic right ventricular (RV) pressure (mmHg). **H.** Systolic systemic arterial (SA) pressure (mmHg). The light gray dashed line denotes the group average, and the grey box contains one standard deviation above and below the mean of each clinical value (*p-value <0.05, **p-value <.01, ***p-value <.001).

The HFrEF cohort displays significantly higher LV systolic volumes **(Figure 2.9)** when compared with HFpEF2 (p-value < 0.001) and NCC (p-value < 0.001) yet no significant difference is found between HFrEF and HFpEF1. Similar to HFrEF, HFpEF1 shows significantly higher LV systolic volumes than both HFpEF2 (p-value < 0.001) and NCC (p-value < 0.05). NCC shows significantly higher LV systolic volumes when compared to HFpEF2 (p-value < 0.05). LV diastolic volumes show similar results as the LV systolic volumes. No significant differences were found between HFrEF and HFpEF1 **(Figure 2.9).** Both HFrEF (p-value < 0.001) and HFpEF1 (p-value < 0.001) show significantly higher diastolic volumes when compared to HFpEF2. NCC has significantly larger diastolic volumes when compared to HFpEF2 (p-value < 0.001). Comparing

the TTE CO at rest between groups did not reveal significant differences between HFrEF and HFpEF1 (**Figure 2.9**). NCC has a significantly higher TTE CO at rest when compared to HFrEF (p-value < 0.01) and HFpEF2 (p-value < 0.001). HFpEF1 had significantly higher values when compared to HFpEF2 (p-value < 0.05.)

RHC pressure measurements revealed that HFpEF2 had significantly higher systolic and diastolic pulmonary arterial pressures when compared to HFrEF (p-value < 0.05.) (**Figure 2.9E** and **F**). Likewise, HFpEF2 shows higher systolic RV pressures when compared to HFrEF (p-value < 0.05) (**Figure 2.9G**). Systolic arterial pressure in both HFpEF1 and NCC is significantly higher when compared to HFrEF (p-value < 0.05) (**Figure 2.9H**).

Overall, analysis of the clinical data with 4 HF subgroups reveals that all patients have higher pressures at rest, with HFpEF2 showing significantly higher pressures when compared to HFrEF. The main distinguishing factor between groups are systolic and diastolic LV volumes where HFrEF and HFpEF1 both have ventricular volume overload, signifying that greater LV volumes could be used as a biomarker for HFrEF-like HFpEF patients.

2.9 Discussion

From this analysis of optimized parameter values representing patient-specific cardiovascular mechanics coupled with unsupervised machine learning techniques, we determine distinct HFpEF subgroups that share similar deep mechanistic phenotypes. These groups could not be determined from clinical data alone but reveal that large LV volumes could be used as a biomarker to indicate HFrEF-like HFpEF patients. Our methodology distinguishing HFpEF groups describes not only the functional details of the cardiovascular system for each population but also for each patient in the population. This approach not only considers mechanical function

and hemodynamics in the heart but also the pulmonary and systemic vasculature providing a deeper understanding of the cardiovascular state for each population and each patient.

2.9.1 Clustering of HFpEF Groups

While HFrEF is characterized by a well-defined phenotype, HFpEF is comprised from a large constellation of changes at the cardiovascular system level. We found that the HFpEF group presented here can be subdivided into 3 subgroups: HFpEF1 described as "HFrEF-like HFpEF", HEpEF2 as "consistent HFpEF", and NCC as "HFpEF patients that are not consistently clustered" (**Figure 2.7A-C)**. Using PCA and clustering techniques to analyze clinical data alone, the same HFpEF distinctions cannot be seen (**Figure 2.6A-C**), suggesting that key discriminators of HFpEF into distinct phenotypes reside at the mechanistic level revealed only by using our methodology. Simply looking at the underlying mechanistic parameters from our patient-specific modeling (**Figure 2.8** for groups HFpEF1, HFpEF2, and NCC), we see that the range of values for the HFpEF population is widely heterogeneous. After finding the 2-dimensional reduced space of parameters derived from the patient-specific tuned models that produces the largest variation across patients through PCA, we can see that there are some HFpEF patients that lie in the same region as the HFrEF patients (**Figure 2.7A).** Extracted physiological parameters, such as E_{LV} and λ_{LV}, are shown to play an important role in describing these distinct patient populations.

2.9.2 HFpEF1 as HFrEF-like HFpEF

In the HFrEF population, we observe elevated λ_{LV}, an observation in accordance with the increased diastolic myocardial stiffness reported in HFrEF patients (Wang *et al.*, 2018). This is coupled with a reduced E_{LV} at rest (**Figure 2.8A** and **B**). Our observations are consistent with the

current understanding of HFrEF, where systolic dysfunction is the main pathological characteristic describing this phenotype (Pinilla-Vera *et al.*, 2019).

In the heterogenous HFpEF population, we surprisingly found that HFpEF1 (HFrEF-like HFpEF) shares the same overall mechanistic parameter trends as the HFrEF group except with lower R_{pul} and R_{sys} (**Table 2.11**). Patients in the HFpEF1 group have significantly higher EF than HFrEF patients but a significantly lower EF than the other two HFpEF groups (**Figure 2.9A**). This could be explained by the fact that while both HFrEF and HFpEF1 show systolic and diastolic LV volume overload when compared to HFpEF2 and NCC (**Figure 2.9B** and **C**). These results suggest a possible biomarker in high LV volumes for HFpEF patients, identifying patients belonging to HFpEF1. Since they share such similar physiological characteristics with the HFrEF cohort, therapeutic strategies currently employed to alleviate systolic dysfunction in HFrEF patients might be employed in HFpEF1 patients. Likewise, our results indicate that both HFrEF and HFpEF1 patients would benefit from treatments that would improve LV contractility.

2.9.3 HFpEF2 and NCC

HFpEF2, the "pure" HFpEF group, has very high λ_{LV} coupled with increased in E_{LV} at rest (**Figure 2.8A** and **B, Table 2.11**). These patients have reduced ventricular filling during diastole, which leads to low systolic volumes (**Figure 2.9B** and **C**). This phenotype presents a particular challenge in situations such as exercise where the normal physiological response involves the recruitment of increased SV along with an increased HR requiring a rapid ventricular relaxation for proper filling. The elevated ventricular stiffness in this cohort could explain the increased levels of systolic and diastolic pulmonary artery pressure, systolic RV pressure, and systemic arterial pressure observed in the clinical data of these patients (**Figure 2.9E-H**). The combination of λ_{LV},

E_{SA}, and higher pressures in the pulmonary and systemic vasculature may account for the increased R_{sys} and R_{pul} also observed in this patient cohort (**Figure 2.8C-E**).

The NCC group was created out of the need to cluster patients that were distinct from HFrEF but did not fall clearly into HFpEF1 or HFpEF2. In falling between two more clearly defined groups, the NCC group may represent a "spectrum" of patients more than a clearly defined subgroup. Perhaps, this is a population of HFpEF undergoing remodeling and given time may decompensate to HFrEF-like HFpEF. Individuals from the NCC group clearly do not behave like individuals from HFrEF or HFpEF1, as they show high λ_{LV} coupled with elevated E_{LV} at rest (**Figure 2.8A** and **B, Table 2.11**). Despite this, NCC displays a milder phenotype than that of the "pure" HFpEF2 group. From the clinical data, NCC EF is the highest among the HFpEF groups, with a systolic LV volume similar to HFpEF2 but diastolic LV volumes similar to HFpEF1 (**Figure 2.9 A-C**).

2.9.4 Possible Clinical Presentation of HFpEF Subgroups

The distinct HFpEF populations found here are consistent with recent studies describing HFpEF as a disparate phenotype. In three of these studies, machine learning methods were used on a variety of clinical and experimental data (Shah, 2019; Cohen *et al.*, 2020; Hahn *et al.*, 2021). In one such study, analysis of RNA sequencing of RV septal endocardial biopsies on control, HFrEF, and HFpEF patients through unsupervised machine learning identified three HFpEF transcriptome subgroups with distinctive pathways and clinical correlations (Hahn *et al.*, 2021). These HFpEF subgroups include:

(Hahn-I)- A HFpEF group close to HFrEF showing the worst clinical outcomes when coupled with metabolic dysfunction.

(Hahn-II)- A HFpEF cohort with smaller hearts and inflammatory and matrix signatures.

(Hahn-III)- A heterogeneous phenotype with pronounced HF symptoms and smaller hearts but lower N-terminal-proB-type natriuretic peptide (NT-proBNP) levels.

Patients in Hahn-I had higher LV volumes, perhaps consistent with the ventricular volume overload we observe in both the HFrEF and HFpEF1 patients in our study. The transcriptome of HFpEF Hahn-I is potentially the closest to HFrEF. Patients in Hahn-II were all female and had the smallest LV size. The small LV size seen in these patients is in accordance with the very small LV volumes observed in our HFpEF2 patients, the only group in our study that has a majority of female patients. Likewise, our NCC group could belong to the heterogeneous Hahn-III.

In a second study, Shah et al. utilized quantitative echocardiography phenotyping with unsupervised machine learning to identify 3 HFpEF phenogroups with differing clinical and echocardiographic characteristics and outcomes (Shah, 2019):

(Shah-I)-A group with natriuretic peptide deficiency syndrome.

(Shah-II)-A group with extreme cardiometabolic syndrome.

(Shah-III)-A group with right ventricular cardio-abdomino-renal syndrome

One of the characteristics of Shah-II was that it had the most severely impaired cardiac relaxation compared to the other HFpEF groups. Our HFpEF2 group shows very high λ_{LV} and perhaps falls in this same category.

A third study used plasma protein profiling coupled with latent class clustering analysis was performed, identifying 3 HFpEF clinical phenotypes characterized by distinct echocardiographic parameters and large artery stiffness(Cohen *et al.*, 2020):

(Cohen-I)- A group with the least concentric LVs, largest LV cavities, lowest absolute and relative LV wall thickness, lowest LA volumes, lowest values of resistive arterial load (systemic

vascular resistance), pulsatile arterial load (total arterial compliance), and large artery stiffness (carotid-femoral pulse wave velocity).

(Cohen-II)- A group with a distinct pattern characterized by small concentric LVs with the lowest LV mass among the groups, the largest left atria, the lowest mitral annular tissue velocities, the stiffest large arteries, and the highest pulsatile and resistive arterial load.

(Cohen-III)- A group with a distinct pattern of concentric LV hypertrophy with the highest values of LV wall thickness, LV mass, and LV mass indexed for height; this phenogroup also exhibited relatively low values of resistive arterial load but high pulsatile arterial load indexed for body size (total arterial compliance index). In our study, when compared to the other HFpEF patients, HFpEF1 has the lowest R_{sys}. Hence, HFpEF1 matches Cohen-I. Similarly, HFpEF2 has the highest R_{sys} and E_{SA} and is similar to Cohen-II.

These studies show novel classifications of HFpEF subgroups based on transcriptomic analysis of endomyocardial biopsy obtained through RHC (Hahn *et al.*, 2021), a detailed clinical, laboratory, ECG, and echocardiographic data phenotyping (Shah, 2019), and plasma biomarker profiling(Cohen *et al.*, 2020) These studies point out clinical markers that may describe these novel HFpEF classifications (i.e., NT-proBNP marker, inflammatory signal differences between groups). However, the nature of cardiovascular hemodynamics, its relationship with the pulmonary and systemic vasculature, and the uniqueness of each patient within a group requires a deep phenotyping approach using clinical data to power cardiovascular model-informed machine learning to define HFpEF subgroups. The methodology presented here identifies similar groupings to these three studies using advanced clinical data and in one case endomyocardial biopsies. However, only routine clinical data is needed, making this methodology more amenable in the clinic once validated.

2.9.5 Role of the Systemic Vasculature in HF

The physiological parameters derived from our cardiovascular system model aligns with the understanding that HFrEF patients have reduced E_{LV}, slightly increased E_{SA}, and normal R_{pul} when compared to normal cardiovascular function (**Figure 2.8**). This alignment of the underlying mechanistic cardiovascular parameters of the model with the conventional wisdom concerning HFrEF suggests that the clinical data used here is sufficient to describe HFrEF. This also gives us confidence in the profile of the deep phenotypes of HFpEF that are revealed here. Our results reveal that that focusing purely on cardiac function may consistently capture the underlying dysfunction in HFrEF but is not a good approach for understanding HFpEF. For example, HFpEF2 patient 20 has increased R_{pul} and R_{sys}, exhibiting large deviations from normal function in the systemic and pulmonary vasculature. Likewise, NCC patient 28 shows increased λ_{LV} and R_{pul} but has similar E_{LV} and E_{SA} to HFrEF. In both patients, addressing the cause for increased resistances in the systemic and pulmonary vasculature may reduce the burden of the heart in HF.

2.9.6 Limitations

In this study, a general HFrEF group was used as the only reference patient population. This methodology determined five HFpEF1 (HFrEF-like HFpEF) patients. Though this is a small cohort of subjects, this accounts for 25% of the total HFpEF patients in our study. It is of interest to see if this percentage holds with a larger patient cohort in the future. Here, two clustering methods were selected that used different approaches, but we could have used other common unsupervised methods (e.g., mean-shift). The selection of *k*-means and hierarchical clustering in this study was made since these are robust and complementary approaches that can be applied to a wide variety of data sets. Applying a thorough clustering analysis with not just HFpEF and

HFrEF phenotypes but other clinical diagnoses such as pulmonary hypertension might provide greater clarity into the physiological differences between groups.

Based on the TTE systolic and diastolic volumes, HFrEF patients 1 and 6 have severe ventricular dilation. Our cardiovascular systems model was unable to account for these large volumes. Hence, making appropriate changes, such as recruiting different stressed volumes for each patient, decreasing ventricular elastance, or implementing a more detailed model, may capture the pathological complexity of these patients. Regardless of future directions taken, the physiological parameters derived from this simple cardiovascular system model can still be useful determinants for HF classification purposes beyond EF.

2.10 Conclusions

HFrEF and HFpEF have classically been defined based on ejection fraction. The HFrEF diagnosis itself is much more understood than HFpEF, which is largely heterogeneous. In accordance with other recent studies, we have determined 3 subgroups of HFpEF with our methodological deep phenotyping approach that uses cardiovascular model-informed machine learning: a HFrEF-like HFpEF group, a "pure" HFpEF group, and a group that exhibits characteristics of both. Moreover, our methodology reveals that potential biomarkers for identifying HFpEF-like HFrEF patients are elevated left ventricular systolic and diastolic volumes. However, these biomarker differences necessary to determine HFpEF subgroups could not be distinguished based on the clinical data alone. Ultimately, the combination of mathematical modeling analysis and machine learning techniques provides immense insight into the classifications of HF as a pathology.

Chapter 3 Application of Physiology Informed Machine Learning to Clinical Data Sets

3.1 Introduction

In the preliminary work described in Chapter 2, we have developed a mathematical model of the cardiovascular system in which mechanistic functional parameters were optimized to match individual patient's pressure, volume, and CO found in TTE and RHC clinical records. The unique parameters of each patient-specific model represent information not directly assessed clinically, such as unbiased estimates of LV passive stiffness and active contractility. Applying ML methods to patient-specific models, we identify three HFpEF subgroups with a distinct cardiovascular function: (Jones-I) a 'HFrEF-like HFpEF', (Jones-II) a 'classical HFpEF', and (Jones-III) patients that did not fall into a distinct cluster. In our follow-up work, we have defined these groups as systolic (SD), diastolic (DD), and mixed (MD) dysfunction HFpEF. Despite EF ≥ 50% across all HFpEF types, an unbiased analysis clustered SD HFpEF patients with HFrEF, whereas DD HFpEF patients had higher LV active contractility and passive stiffness. This chapter is a logical extension of our previous work in HFpEF phenotyping.

Here, we applied the functional phenotyping model described in Chapter 2 to the RHC and TTE data from a combined group of patients studied by Jones et al. (Jones *et al.*, 2021) and Hahn et al. (Hahn *et al.*, 2021). With our methodology, we also retrospectively analyzed clinical data from two HFpEF clinical trials: an interatrial shunt device (IASD) (Feldman *et al.*, 2018), and a pilot randomized intervention trial comparing the efficacy of trimetazidine (TMZ) (van de Bovenkamp *et al.*, 2020). Briefly, for all these studies, we applied unsupervised ML to the resulting

optimized parameters from our patient-specific simulations, creating HF groups. The first two principal components (PCs) describing >50% of the total variance of the patients in the defined HF groups, were used as input for supervised ML (support vector machine, SVM) where defined regions of a similar phenotype for patients were created for systolic, mixed, and diastolic dysfunction (SD, MD, and DD HFpEF, respectively). HFpEF patients that did not consistently cluster (NCC) were excluded from the supervised ML SVM algorithm. To predict NCC dysfunction phenotype, the first two PCs of the NCC HFpEF optimized parameters were superimposed on the SVM plot.

3.2 Precision Phenotyping of Cardiovascular Dysfunction in Heart Failure

3.2.1 Acknowledgements

This chapter section is being prepared for publication as an academic journal article at the Journal of the American Heart Association:

Jones, E.; Hahn, S.V.; Randall, E.B.; Hummel, S.; Cameron, D.; Beard, D.; Carlson, B.; "Precision Phenotyping of Cardiovascular Dysfunction in Heart Failure". *Manuscript in preparation.*

3.2.2 Introduction

HF patients are classified based on their LVEF. The pathophysiology of HFrEF, (LVEF ≤40%) and mildly reduced EF (HFmrEF, LVEF 41-49%) are well-studied and have several targeted therapies in clinical use and under development. In contrast, HFpEF (LVEF ≥50%) is a heterogeneous condition with fewer evidence-based treatments in which phenotyping has been advocated to target therapies (Shah et al., 2020).

We recently reported two potentially complementary approaches to subgroup HFpEF patients using unsupervised ML Jones et al. (Jones *et al.*, 2021) applied functional phenotyping to analyze data from TTE and RHC using a mathematical model of the cardiovascular system to derive patient-specific functional parameters, resulting in three HFpEF subgroups with distinct cardiovascular function: (Jones-I) a 'HFrEF-like HFpEF', (Jones-II) a 'classical HFpEF', and (Jones-III) patients that did not fall into a distinct cluster. While cardiac systolic dysfunction represents the primary cardiovascular defect in our analysis of HFrEF and the Jones-I patients, the other HFpEF patients were characterized by dysfunction in the heart and the entire vascular system. Hahn et al. (Hahn *et al.*, 2021) analyzed RNA sequencing data from RV septal endocardial biopsies on control, HFrEF and HFpEF patients, revealing three HFpEF transcriptome subgroups with distinct pathways and clinical correlations: (Hahn-I) A HFpEF group with larger hearts, more severe pulmonary hypertension, higher NPs, and a transcriptome most similar to HFrEF; (Hahn-II) an all-female HFpEF group with smaller hearts, lower NPs, and higher inflammatory and extracellular matrix gene expression; and (Hahn-III) a mixed phenotype. To determine if these approaches reveal complementary information, all patients from the original studies Jones et al. (8 HFrEF, 21 HFpEF) and Hahn et al. (41 HFpEF) were used for functional phenotyping as in Jones et al. (Jones et al., 2021).

3.2.3 Methodology

Clinical Data Used to Parameterize Cardiovascular System Model

For the Hahn et al. HFpEF (n=41) the general clinical data provided included: body weight, height, and sex. RHC data included PA and SA pressures (mmHg) at systole and diastole as well as average PCW. RV pressures were derived from PA pressures. Likewise, HR (beats/min), and

thermodilution CO (L/min) were also available from RHC records. TTE data included only the LV inner diameter at diastole (mm), which was used to estimate LV volume at systole and diastole with the Teicholz equation (Teichholz *et al.*, 1976). Thus, HR was assumed to be the same for RHC and TTE records. For the Jones et al. HFrEF (n=8) and HFpEF (n=21), the same general, RHC, and TTE clinical data available to inform the patient-specific model optimizations as in our previous work were used (Jones et al., 2021).

PCA

We performed a PCA for the visualization of the spread in the parameter space. Using two unsupervised clustering methods on our optimized model parameters, we determined if as in our previous work (Jones *et al.*, 2021), three distinct subgroups of HFpEF patients with similar cardiovascular etiologies are discerned from our model simulations. Since our purpose here is to subgroup HFpEF patients only, we grouped all HFrEF patients according to their clinical diagnosis and considered the clusters with the most HFrEF patients as the most "HFrEF-like." We also considered patients who switched between the clusters of different methods as not-consistently clustered (NCC). However, unlike our previous work, we assigned HFpEF patients to different subgroups based only on clustering rather than whether they belonged to the HFrEF, PCA overlap region. We chose this approach because we defined the PCA hulls for HFrEF and HFpEF by patients' diagnostic EF. The inadequacies of categorizing HF patients primarily by EF have been exposed previously (Beard *et al.*, 2021), and here, we would like to move towards functional phenotyping for HFpEF classification.

Unsupervised ML: k-means and Hierarchical Clustering

With an expanded data set of 70 HF patients and having previously found three distinct HFpEF groups (Jones *et al.*, 2021) in line with the work of others (Shah, 2019; Cohen *et al.*, 2020;

Hahn *et al.*, 2021), we chose to group the patients into three clusters with the aid of two unsupervised ML methods. For *k*-means clustering, the algorithm randomly chose three patients as cluster centroids and grouped all other patients relative to their L1-distance from each centroid. For hierarchical clustering, we partitioned our patients into three clusters by cutting the dendrogram halfway between the third-from-last, second-from-last and last linkages.

In both clustering methods, all the HFrEF patients fell into one cluster, which we designate as cluster A. We found that for both clustering methods, a subgroup of HFpEF patients always belonged to cluster A. Hence, this HFpEF subgroup was considered as 'HFrEF-like HFpEF' and was labeled as SD HFpEF. Our next HFpEF group consistently belonged to cluster C in both clustering methods and sat in the outermost region of the parameter space where only other HFpEF were present, thus we considered it as 'classical' HFpEF, and was labeled as DD HFpEF. For both clustering methods, we found a HFpEF group that always belonged to cluster B and is between the SD and DD HFpEF groups. Thus, we considered it had characteristics of both systolic and diastolic dysfunction and was labeled as MD HFpEF. We marked patients with HFpEF who were not consistently clustered in clusters A, B, and C in *k*-means and hierarchical clustering as NCC.

Supervised ML: Support Vector Machine Algorithm

A supervised ML algorithm trains data observation models to predict categories (i.e., classifications) (Cristianini & Ricci, 2008). In this study, the 'observations' in the data set are our HF patients, the features informing the supervised ML model are the first two PCs of the optimized parameter PCA and the predicted classes are the three types of HF dysfunction derived from our unsupervised ML approach (SD, MD, DD). The support vector machine (SVM) algorithm identifies "hyperplanes" that best separate the three classes of HF. Support vectors are the data points that lie closest to the hyperplane, and thus determine where the hyperplane lies. One of the

key features of SVM is that it often uses a 'kernel-trick' to map linear space to a non-linear space specified by the kernel. This 'kernel-trick' allows the hyperplane to take a non-linear shape (Cristianini & Ricci, 2008). For our study, we used the radial basis function as our kernel. In summary, to do this in MATLAB, we trained an SVM algorithm model for each of the three classes of HF to distinguish whether a given patient was or was not a member of that class of HF. Specifically, each model predicted a score corresponding to the probability that a given patient was a member of its class of HF. To predict the type of dysfunction NCC HFpEF patients might have, we superimposed their first two optimized parameter PCs on the created SVM plot.

3.2.4 Results

We first used RHC and TTE pressure and volume measurements as input to the phenotypic model. We then applied unsupervised ML to the resulting optimized parameters, creating HF groups. Our model simulations show that the combined Jones et al. and Hahn et al. HFpEF cohort (n=62) has a much wider distribution of the parameter values than the HFrEF cohort (n=8). The first two PCs of our optimized parameter PCA describe 64% of the total variance. For visualization purposes, we prescribed a convex hull for the HFpEF and HFrEF groups when plotting our PCA results, but we did not to include this criterion in HFpEF subgroup designation. However, we observed that a subset of combined HFpEF fell in PCA overlap region **(Figure 3.1A).** We then conducted *k*-means **(Figure 3.1B)** and hierarchical clustering (**Figure 3.1C)** on the optimized patient parameters. **Table 3.1** shows that this independent analysis with k-means and hierarchical clustering on the optimized parameter values reveals that the 70 patients fall into distinct groups as:

- HFrEF ($n = 8$) - patients diagnosed as HFrEF.

- SD ($n = 16$) - HFpEF patients that fall in, k-means and hierarchical cluster A.
- MD ($n = 11$) - HFpEF patients that fall in, k-means and hierarchical cluster B.
- DD ($n = 9$) - HFpEF patients that fall in k-means cluster and hierarchical cluster C.
- NCC ($n = 26$) - HFpEF patients that do not consistently cluster.

In our unsupervised ML, HFrEF and SD HFpEF always belong to cluster A, so we decided to combine HFrEF and SD HFpEF patients in the same 'SD' class, (*n*=24) for our supervised ML analysis. We used the first two PCs describing 64% of the total variance of the patients in the defined HF groups, as input for supervised ML (support vector machine, SVM). With the SVM algorithm, we defined regions of a similar phenotype for patients for systolic, mixed, and diastolic dysfunction (SD, MD, and DD HFpEF, respectively (**Figure 3.2A)**). We excluded HFpEF patients without consistent clustering (NCC, *n*=26) from the supervised ML SVM algorithm (**Figure 3.2B**). To predict the NCC dysfunctional phenotype, we overlaid the first two PCs of the NCC HFpEF optimized parameters on the SVM plot (**Figure 3.2D**).

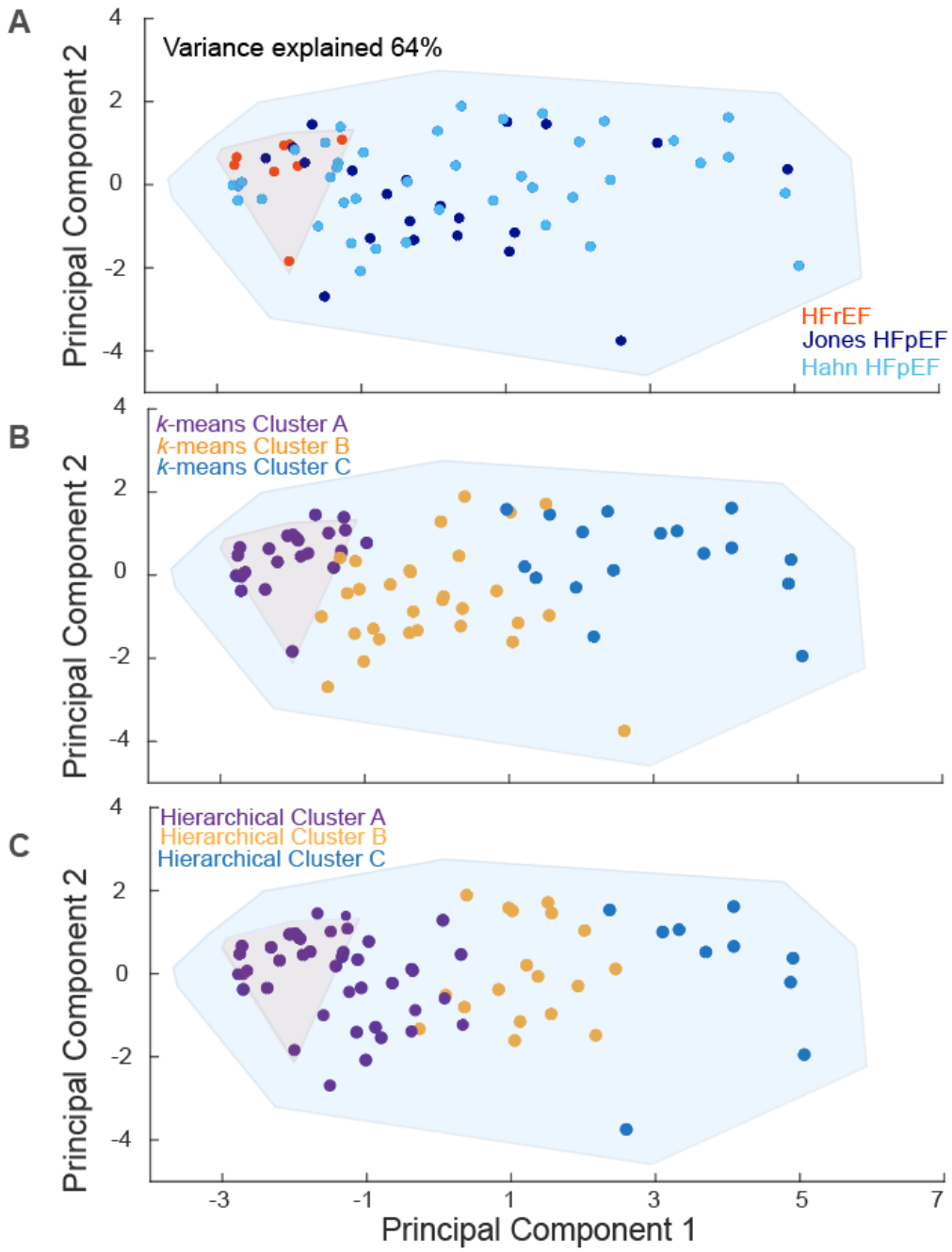

Figure 3.1 Clustering analysis of optimized model parameter values from Jones and Hahn combined HF datasets**.** This analysis determines three distinct groups of HFpEF patients. **A.** Principal component analysis (PCA) of the optimized model parameters. Reference convex hulls for the HFrEF (orange) and combined HFpEF (blue) patients are determined by individual patient diagnosis. HFpEF patients denoted by dark blue come from Jones et al. and HFpEF patients denoted in light blue come from Hahn et al. **B.** *k*-means clustering of optimized parameter values superimposed on the PCA hulls where cluster A (purple) is more HFrEF-like, cluster B is considered to have mixed dysfunction (yellow) and cluster C (blue) is more HFpEF-like. **C.** Hierarchical clustering of optimized parameter values superimposed on the PCA hulls where cluster A (purple) is more HFrEF-like, cluster cluster B (yellow) is considered to have mixed dysfunction and cluster C (blue) is more HFpEF-like.

Table 3.1 Jones and Hahn HF patient classification from combined clustering results based on optimized parameters.

HFrEF	SD	MD	DD	NCC
2	11	12	16	13
3	17	14	20	15
4	23	24	35	18
5	29	25	38	19
7	32	28	46	21
8	37	31	49	22
9	41	36	65	26
10	44	50	67	27
	48	54	69	30
	51	63		33
	53	68		34
	55			39
	56			40
	57			42
	60			43
	61			45
				47
				52
				58
				59
				62
				64
				66
				70
				71
				72

HFrEF – heart failure with reduced ejection fraction. SD-systolic dysfunction. MD-mixed dysfunction. DD-diastolic dysfunction. NCC – not consistently clustered.

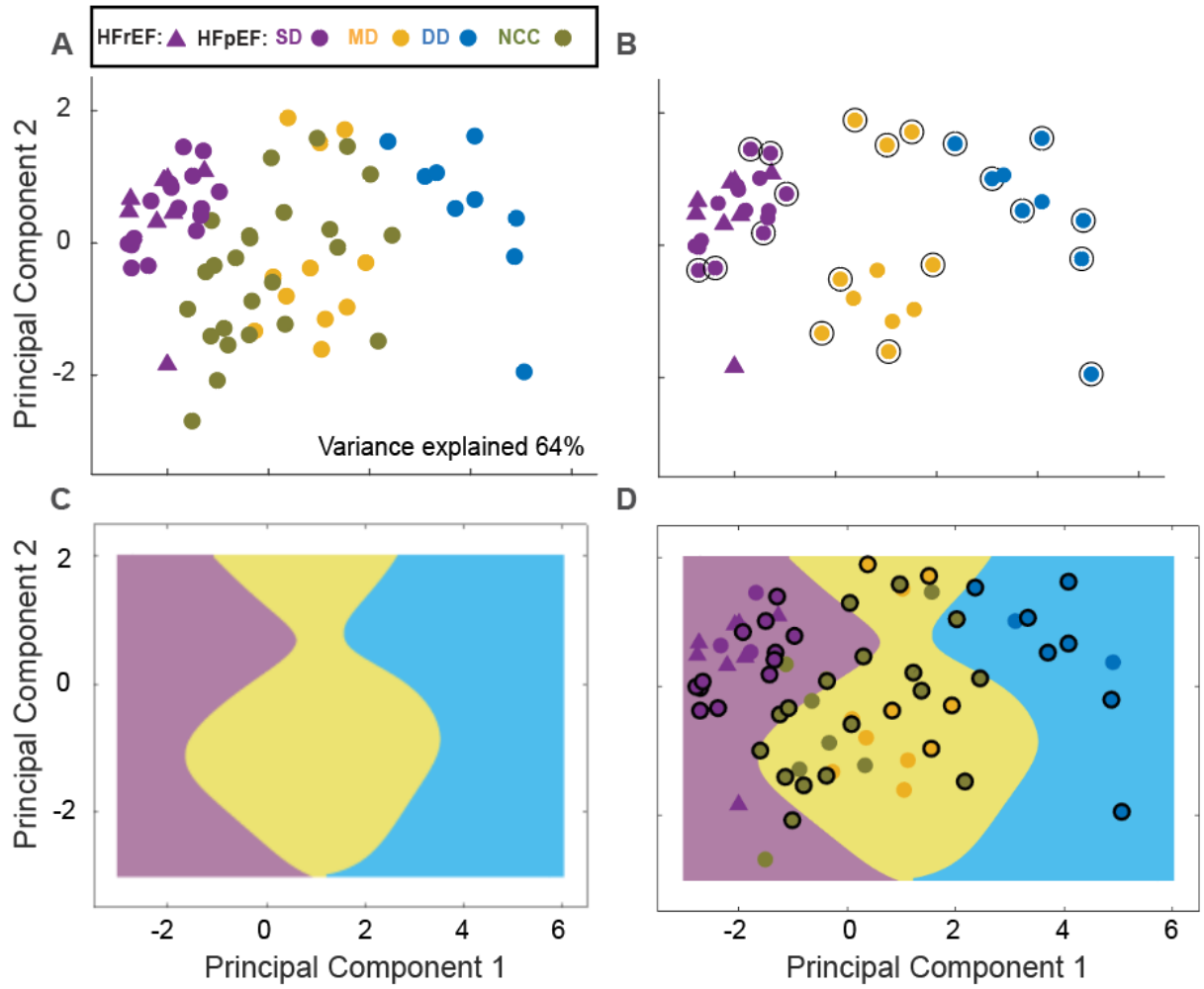

Figure 3.2 Defining regions of similar phenotype for HF patients based on systolic, mixed, and diastolic dysfunction. **A.** HF groups created by unsupervised ML on model parameters: systolic (purple), mixed (yellow), and diastolic (blue) dysfunction (SD, MD, and DD, respectively). HFpEF patients that did not consistently cluster (NCC, green). For reference HFrEF patients can be identified by triangles and HFpEF patients can be identified by circles. **B.** Identification of support vectors: NCC patients were removed, and a Support Vector Machine (SVM) classifier was trained with the patients in the SD, MD and DD groups. Support vectors (SV) are observations that occur on or beyond their estimated class boundaries (identified SVs withing groups are circled). **C.** HF dysfunction regions defined by SVM. **D.** NCC HFpEF patients were superimposed on the SVM plot to predict their HFpEF dysfunction phenotype. Dark thick border = Hahn patients.

Our results show that with our approach we classified 55% of Hahn-I patients as SD HFpEF, 50% of Hahn-II patients as DD HFpEF and 41% of Hahn-III patients overlapped with our MD HFpEF groups. Using a non-parametric permutation test (Dwivedi *et al.*, 2017) the random chance of this overlap between the two methods is extremely low (p-value= 0.006).

Consistent with Jones et al., the SD HFpEF group shares similar mechanistic parameter trends as HFrEF (**Figure 3.3A-F**). Both HFrEF and SD HFpEF show higher LV volumes when compared to DD and MD HFpEF (**Figure 3.3E, F** and **Figure 3.4B**). Hence, HFpEF patients with high LV volumes will cluster with HFrEF. We show that the DD HFpEF patients have an increased LV active contractility (E_{LV}) coupled with a high LV passive stiffness (λ_{LV}) in the baseline state, (**Figure 3.3 A, B**). These patients also have reduced LV filling during diastole, which leads to low systolic and diastolic volumes (**Figure 3.3E, F** and **Figure 3.4 D**). The combination of increased λ_{LV}, systemic (R_{sys}) and pulmonary resistances (R_{pul}) observed in this, (**Figure 3.3,A-D**) may account for the high pressures (not shown) also observed in this patient cohort. Strikingly, the DD HFpEF group we identified was 90% female, suggesting that there may be sex-driven mechanisms developing this phenotype requiring further analysis. MD HFpEF is a distinct group among the systolic and diastolic defined groups. Individuals from the MD HFpEF do not behave like individuals from SD HFpEF, as they show high λ_{LV} coupled with elevated E_{LV} at baseline (**Figure 3.3 A, B** and **Figure 3.4C**). Despite this, MD HFpEF patients display a phenotype that is closer to normal cardiovascular function than that of the DD HFpEF group (**Figure 3.3, C, D** and **Figure 3.4C**).

3.2.5 Conclusions

The overlap of functional phenotypic identification of SD-HFpEF and transcriptomic Hahn-I suggests that a subset of HFpEF has HFrEF-like systolic dysfunction and transcriptional remodeling. Overall, we interpreted the degree of overlap in each of the three distinct HFpEF groups to provide complementary information for transcriptomic and hemodynamic approaches. In conclusion, functional phenotyping identifies HF patients with systolic or diastolic dysfunction

and exposes the inadequacies of categorizing HF patients primarily by EF (Beard *et al.*, 2021), likewise, it informs us about the constellation of mechanisms in the pathophysiology of HFpEF, some of which may be targeted therapeutically.

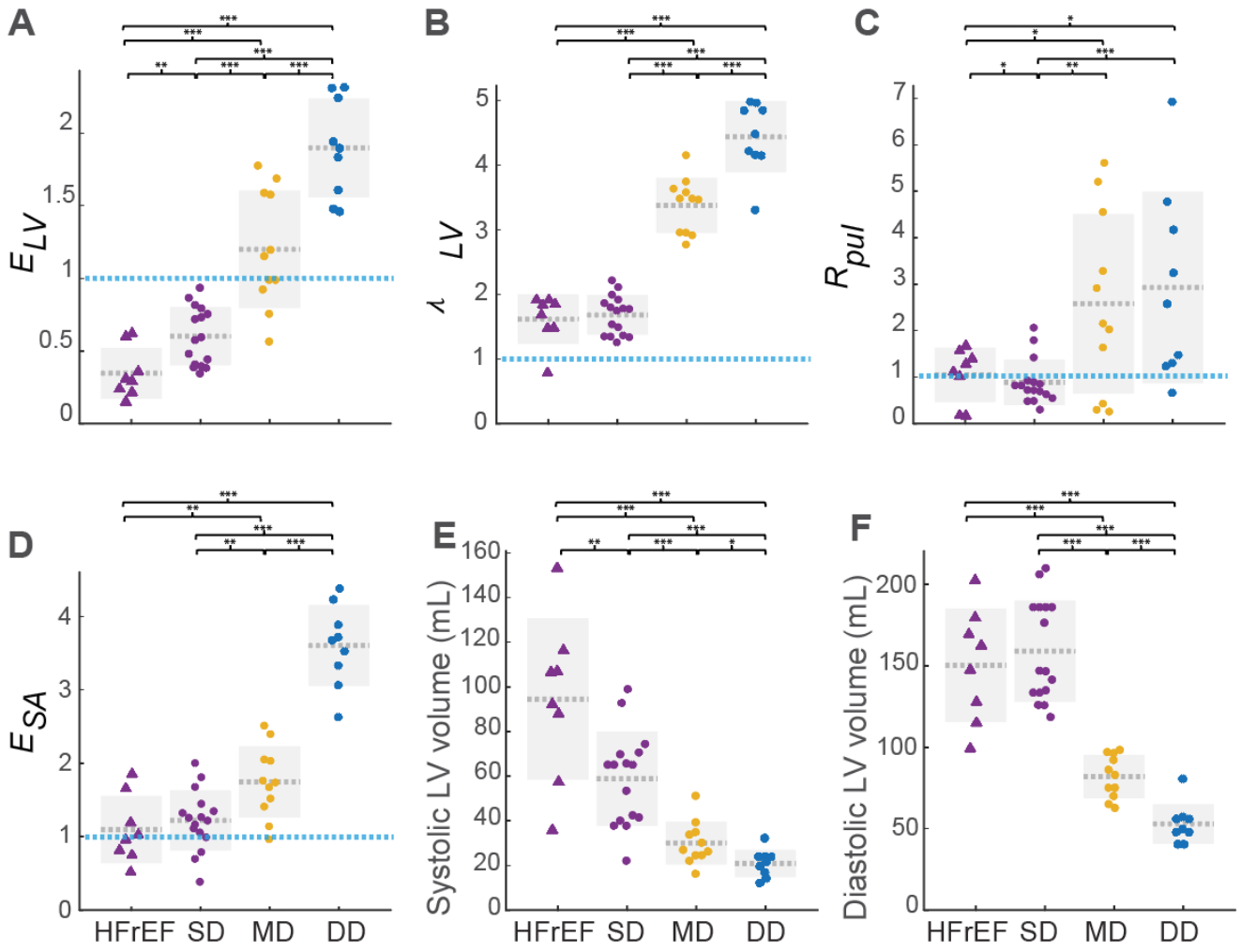

Figure 3.3 Box plots of the optimized parameter values with heart failure groups. Analysis of the optimized parameters gives us an understanding of the mechanistic differences between the three HFpEF groups that cannot be seen by analyzing the clinical data alone. **A.** LV active contractility (mmHg mL^{-1}). **B**. LV passive stiffness (mL^{-1}). **D**. Pulmonary resistance (mmHg s mL^{-1}) **D**. Arterial elastance (mmHg mL^{-1}). All parameter values are plotted relative to the normal model values (blue dashed lines). The light gray dashed line denotes the average, and the gray box contains one standard deviation above and below the mean of each parameter value. **E.** Systolic **F.** Diastolic LV volume (mL) (**p*-value <0.05, ***p*-value <0.01, ****p*-value <0.001).

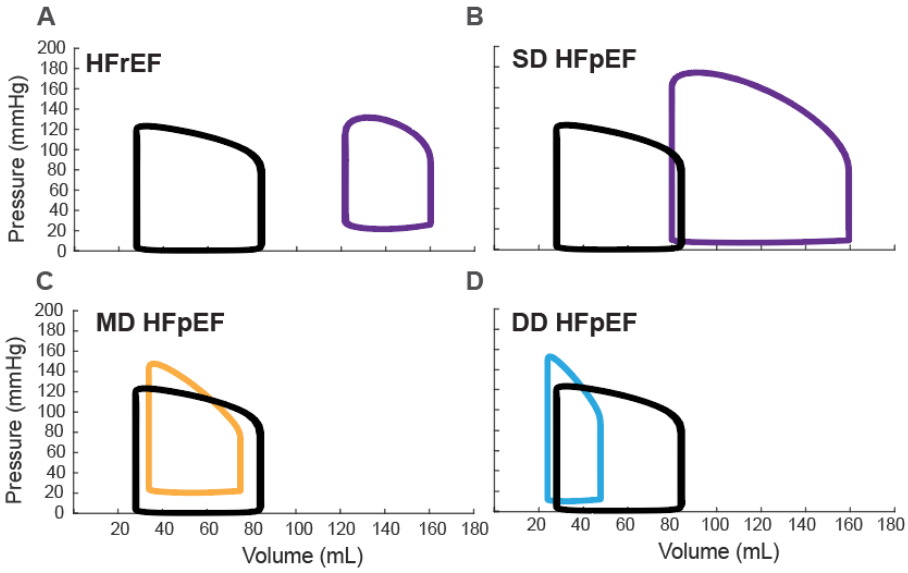

Figure 3.4 A-D Model predicted LV pressure-volume loops for representative HF patients. Black: Normal healthy patient LV PV loop.

3.1 Retrospective Analysis of IASD HFpEF Patient Selection for Clinical Trial

3.1.1 Acknowledgements

We would like to thank, Kiley Hassevoort, our 2020 FCVC Summer Undergraduate Research Fellow for generating preliminary data for this work.

3.1.2 Introduction

Pulmonary vasocongestion due to high pressures in the LA at rest and/or exercise is a common feature observed in HFpEF patients. An abnormally high PCW pressure measured through an invasive RHC, is one of the diagnostic indicators of this phenomenon. It has been hypothesized that treatments reducing PCW, particularly during exercise, will improve the quality of life in the heterogeneous HFpEF population. A suggested treatment for reducing elevated LA

pressure in patients with HFpEF unresponsive to standard therapy is an atrial shunt device (IASD®). This device is placed by a cardiologist invasively during a one-time procedure: through catheterization the shunt creates a passage between the high-pressure LA and lower pressure RA, allowing blood flow between the two. This passage aims at reducing pressure in the lungs and left side of the heart. Preliminary results indicate that IASD reduction of PCW, results in about a 25% increase in pulmonary blood flow and it is hypothesized these effects are responsible for the symptom reduction in HFpEF patients benefiting after IASD treatment (Obokata *et al.*, 2019). Yet, in the REDUCE LAP-HF II clinical trial, implantation of the IASD in patients with HFpEF had no effect on cardiovascular death or stroke events, HF symptoms, or quality of life status (Shah *et al.*, 2022). Dissecting, which HFpEF patients in this heterogeneous population would benefit from IASD treatment is a current challenge. To determine if we could find distinct cohorts of HFpEF subjects showing different degrees of cardiovascular dysfunction as well as different responses to the IASD, we applied the functional phenotyping model from Jones et al. (Jones *et al.*, 2021) in the context of this study.

3.1.3 Methodology

We analyzed the RHC and TTE data from a combined group of patients from Jones et al. (8 HFrEF, 20 HFpEF), Hahn et al. (41 HFpEF) and patients selected for a 6-month IASD trial (38 HFpEF)(Feldman *et al.*, 2018), prior to treatment at rest. The IASD HFpEF records had the minimum amount of clinical data by which we were able to parameterize our cardiovascular system computational model. From the IASD HFpEF cohort, RHC records we had access to contain the following pressures (mmHg): mean PA and PCW as well as systolic SA pressure. RHC records likewise had available CO (L/min) by thermodilution/Fick. From TTE recordings, only

the diastolic left ventricular 4-chamber volume (mL) was available. Likewise, only one HR was reported for both TTE and RHC (we thus assumed HR to be the same for both procedures). In general, patient height and weight data were available, but patient sex was missing. We therefore assumed that the sex of all patients was male (preliminary work showed that changing sex did not result in a significant change in nominal parameter calculations). For the IASD HFpEF cohort, these clinical data were sufficient to run our patient-specific patient simulations informing the following five mechanistic parameters: LV active contractility, LV passive stiffness, pulmonary vein stiffness as well as pulmonary and systemic resistance. We calculated the remaining parameters nominally for each patient, and we fixed the LV and RV diastolic reference pressure as in Jones et al. (Jones *et al.*, 2021). To compare all patient optimizations, HF patients from the Jones et al. (Jones *et al.*, 2021) and Hahn et al. (Hahn *et al.*, 2021)data sets where re-run with the same data as was available to us from the IASD HFpEF patients. Thus, all patients had optimized parameter simulations for the same 5 parameters as IASD HFpEF. See **Table 3.2** for an overview of parameter calculations.

We performed a PCA for the visualization of the spread in the parameter space. To test if three distinct subgroups of HFpEF patients with similar cardiovascular etiologies could be discerned from our model simulations, we clustered patients into three groups using two unsupervised clustering methods (*k*-means and hierarchical clustering) on our optimized model parameters. In both clustering methods, all the HFrEF patients fell into one cluster, which we designate as cluster A, thus all 'HFrEF-like' HFpEF patients falling into cluster A for both methods were labeled as SD HFpEF. Our next HFpEF group sat in the outermost region of the parameter space where only other HFpEF were present, consistently belonged to cluster C in both methods, and was considered to have the 'classical' HFpEF characteristics, thus it was labeled as DD

HFpEF. We observed a HFpEF group sitting between the SD and DD patients, consistently belonging to cluster B in both methods, thus we labeled it as MD HFpEF as it likely had characteristics of both systolic and diastolic dysfunction. We labeled HFpEF patients that did not consistently cluster among groups A, B and C in *k*-means and hierarchical clustering as NCC.

A HF patient from the Jones et al. group, was so dramatically distanced from all the other patients in the unsupervised ML (*k*-means and hierarchical clustering) that it became a cluster by itself. Because of this, we were faced with two choices: 1) increase the number of clusters used, 2) remove this patient and re-cluster. We decided to pursue the latter option, removing this outlier patient and re-clustering with unsupervised ML. When we do this, the Hanh et al. and Jones et al. HF patients fall in similar groupings as when they were analyzed by themselves (section 3.2), as well as when analyzed in combination with another HFpEF population selected for a clinical trial (section 3.3). Succeeding this, we performed SVM to predict the areas of HF dysfunction that NCC patients might belong to.

Table 3.2 Model parameters for patients at rest in IASD HFpEF data analysis.

Symbol	Units	Description	Fixed	Adjustable	Nominal
E_{LV}	mmHg mL^{-1}	LV active contractility		X	
$P_{0,LV}$	mmHg	LV diastolic reference pressure	X		X
λ_{LV}	mL^{-1}	LV passive stiffness		X	
E_{RV}	mmHg mL^{-1}	RV active contractility			X
$P_{0,RV}$	mmHg	RV diastolic reference pressure	X		
λ_{RV}	mL^{-1}	RV passive stiffness			X
E_{PA}	mmHg mL^{-1}	PA stiffness			X
E_{PV}	mmHg mL^{-1}	PV stiffness		X	
R_{pul}	mmHg s mL^{-1}	Pulmonary resistance		X	
E_{SA}	mmHg mL^{-1}	SA stiffness			X
E_{SV}	mmHg mL^{-1}	SV stiffness			X
R_{sys}	mmHg s mL^{-1}	Systemic resistance		X	
R_{mval}	mmHg s mL^{-1}	Mitral valve			X
R_{aval}	mmHg s mL^{-1}	Aortic valve			X
R_{tval}	mmHg s mL^{-1}	Tricuspid valve			X
R_{pval}	mmHg s mL^{-1}	Pulmonary valve			X

3.1.4 Results

Figure 3.5 shows a representative IASD patient. As in our previous work, our model simulations predicted that the combined HFpEF population (n = 99) had a wider distribution of parameter values than the HFrEF population. The first two principal components of our optimized parametric PCA describe 68% of the total variance in **Figure 3.6**. After performing unsupervised ML to create HF patient groupings and supervised ML (SVM) to generate HF dysfunctional regions, we found that IASD HFpEF patients were either SD HFpEF or MD HFpEF, **Figure 3.6**.

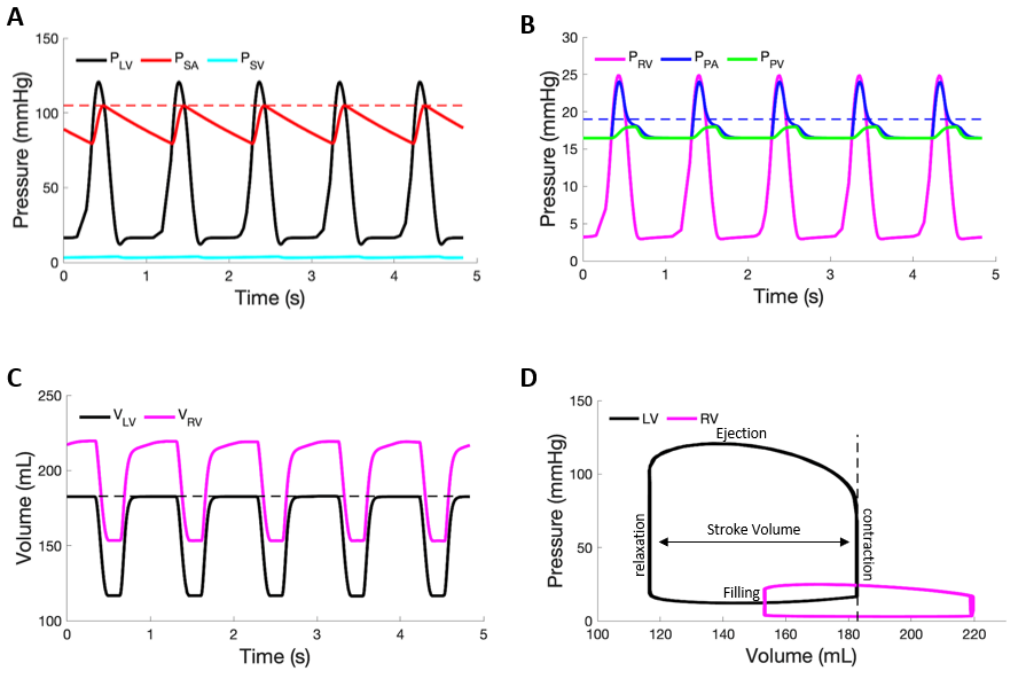

Figure 3.5 Model predictions for pressures and volumes of representative IASD patient. **A.** Pressure (mmHg) time courses for the left ventricle (P_{LV}, black), systemic arteries (P_{SA}, red), and systemic veins (P_{SV}, cyan). Data for the systolic systemic arterial pressure is plotted as horizontal dashed red lines. **B**. Pressure time courses for the right ventricle (P_{RV}, magenta), pulmonary arteries (P_{PA}, blue), and pulmonary veins (P_{PV}, green). Data for the pulmonary mean arterial pressure is plotted as horizontal dashed blue line. **C**. Volume (mL) time courses for the left (V_{LV}, black) and right (V_{RV}, magenta) ventricles. Data for the diastolic left ventricular volume is plotted as a horizontal dashed black line. **D**. Pressure-volume loops for the left (black) and right (magenta) ventricles. Data for the diastolic left ventricular volume is plotted as vertical dashed black lines.

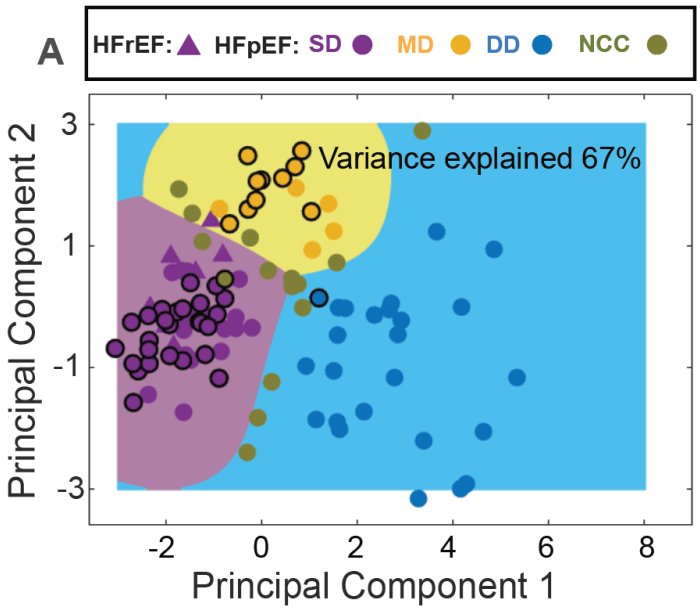

Figure 3.6 IASD HFpEF fall into regions of systolic and mixed dysfunction in optimized parameter space. HF groups created by unsupervised ML on model parameters: systolic (purple), mixed (yellow) and diastolic (blue) and dysfunction (SD, MD, and DD, respectively). HFpEF patients that did not consistently cluster (NCC). For reference HFrEF patients can be identified by triangles and HFpEF patients can be identified by circles. Circles with dark outline represent IASD HFpEF.

3.1.5 Conclusions

Differences in response to IASD treatment have been retrospectively identified in HFpEF subgroups during exercise, defined by systolic PA pressure, RA volume, and sex (Borlaug *et al.*, 2022). An exclusion criterion for the REDUCE LAP-HF II (Shah *et al.*, 2022) was pulmonary vascular disease (PVD), diagnosed by a resting pulmonary vascular resistance (PVR) greater than 3.5 Wood units. Recent studies have shown that many HFpEF patients display a latent PVD, only apparent during exercise. While reduction of LA pressure is one of the benefits expected after shunt implantation, one of its secondary effects is increased pulmonary blood flow. Increased pulmonary blood flow may lead to congestion and pulmonary edema in patients already struggling with PVD. Interestingly, the presence of latent PVD was associated with an adverse response to

the shunt, whereas patients without it displayed some benefits after shunt treatment (Borlaug *et al.*, 2022). The 38 IASD HFpEF patients we analyzed at least during rest fell into the SD and MD HFpEF categories. Total distance walked in 6 minutes and peak exercise 6 months after shunt treatment was not statistically different between groups, although the SD group had a better Minnesota Living with HF Questionnaire (MLHFQ) score 6-month post shunt compared to the MD group (data not shown). Interestingly increased pulmonary resistance, which may be an indicator of latent PVD, is a hallmark of our MD HFpEF as shown in the previous section **Figure 3.3C**.

Our model currently characterizes the cardiovascular physiology of patients at rest, yet as previously mentioned some of the pathophysiology characterizing HFpEF is mostly visible during exercise. Follow-up work may include adapting our model to be able to simulate exercise using the framework developed by Jesek et al. (Jezek et al., 2022).We hope that our tools will help HFpEF diagnosis as well as patient selection for clinical trials such as the IASD.

3.2 Retrospective Analysis of TMZ HFpEF Patient Selection for Clinical Trial

3.2.1 Acknowledgements

We would like to thank, Abigail Liebetreu, our 2021 FCVC Summer Undergraduate Research Fellow for generating preliminary data for this work.

3.2.2 Introduction

Finally, we retrospectively analyzed clinical data with our model-based analysis and physiology-informed precision phenotyping tool from a randomized trimetazidine (TMZ) trial consisting of 25 patients with stable HFpEF. In this cross-over study subjects were administered

TMZ (fatty acid β-oxidation inhibitor) or placebo "for two periods of 3 months separated by a 2-week washout period" (van de Bovenkamp *et al.*, 2020). The classical understanding of HFpEF is that this patient population struggles with stiff ventricles, that can't relax optimally during diastole. Diastolic relaxation is a very energy-demanding process, and it was hypothesized that TMZ by altering cardiac mitochondrial substrate selection would improve the cardiac bioenergetic status present in diastolic dysfunction. Subjects were assessed following placebo and TMZ treatment at rest and during exercise via RHC and phosphorus-31 magnetic resonance spectroscopy to assess myocardial energetics. Overall, this trial resulted in no significant differences in primary (PCW pressures) or secondary (myocardial energetic status) endpoints. To determine if we could find distinct cohorts of HFpEF subjects showing different degrees of cardiovascular dysfunction as well as different responses to TMZ treatment, we applied the functional phenotyping model from Jones et al. (Jones *et al.*, 2021) in the context of this study.

3.2.3 Methodology

We analyzed the RHC/TTE data from a combined group of patients from Jones et al. (8 HFrEF, 21 HFpEF), Hahn et al. (41 HFpEF), and the RHC/CMRI data from the TMZ trial patients prior to treatment at rest (25 HFpEF). As our previous work, our model simulations predicted that the combined HFpEF population (n=87) had a much wider distribution of the parameter values than the HFrEF cohort. After obtaining our patient specific optimizations, we then performed a PCA for the visualization of the spread in the parameter space. Using two unsupervised clustering methods (k-means and hierarchical clustering) on our optimized model parameters, we determined if like our previous work, three distinct subgroups of HFpEF patients with similar cardiovascular

etiologies could be discerned from our model simulations. Succeeding this, we performed SVM to predict the areas of HF dysfunction that NCC patients might belong to.

3.2.4 Results

By plotting the first two PCs of our optimized parameter PCA, we describe 59% of the total variance in the patient population (**Figure 3.7A**). Surprisingly, we found that the majority of HFpEF patients selected for TMZ clinical trials fell within the convex hull defined by HFrEF patients, or just outside it. All patients with HFpEF in the TMZ trial were divided into two categories: SD HFpEF (n=18) and NCC (n=7). Thus, in the context of this study, none of the HFpEF patients selected for the TMZ clinical trial showed the classic diastolic dysfunction phenotype with about 70% of the patients showing some form of systolic dysfunction and only 30% having some form of mixed dysfunction (at least during rest). **Figure 3.7A** also illustrates the singular value decomposition of patient parameters, and the subgroup clusters (labeled SD, MD, and DD) identified by our method.

70% of HFpEF patients selected for the TMZ trial belonged to the SD HFpEF group, and consistent with Jones et al.,(Jones *et al.*, 2021) with trends in mechanistic parameters similar to HFrEF (**Figure 3.8A-F**). Both HFrEF and SD HFpEF show higher LV volumes when compared to DD and MD HFpEF (**Figure 3.8 E, F**). Thus, high LV volumes suggest that patients with HFpEF will aggregate with HFrEF. The DD HFpEF patients are shown to have an increased LV active contractility (E_{LV}) coupled with a high LV passive stiffness (λ_{LV}) in the baseline state, (**Figure 3.8 A, B**).These patients also have reduced LV filling during diastole, which leads to low systolic and diastolic volumes (**Figure 3.8 E,F**). Thus, the DD group has the classic characteristics

associated with diastolic dysfunction in HFpEF, strikingly none of the HFpEF patients selected for the TMZ study are a part of the DD group.

3.2.5 Conclusions

Thus, although the numbers of subjects for this preliminary study are relatively low, these results suggest one of the reasons why patients selected for the TMZ study did not benefit from the treatment may have been due to a biased selection for patients with systolic dysfunction rather the classical diastolic dysfunction associated with HFpEF.

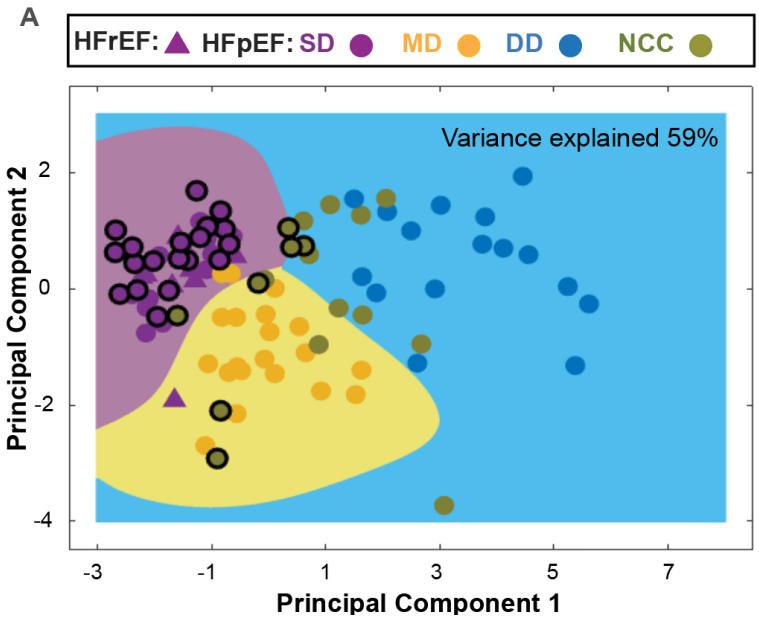

Figure 3.7 TMZ HFpEF fall into regions of systolic and mixed dysfunction in optimized parameter space. HF groups created by unsupervised ML on model parameters: systolic (purple), mixed (yellow) and diastolic (blue) and dysfunction (SD, MD, and DD, respectively). HFpEF patients that did not consistently cluster (NCC). For reference HFrEF patients can be identified by triangles and HFpEF patients can be identified by circles. Circles with dark outline represent TMZ HFpEF.

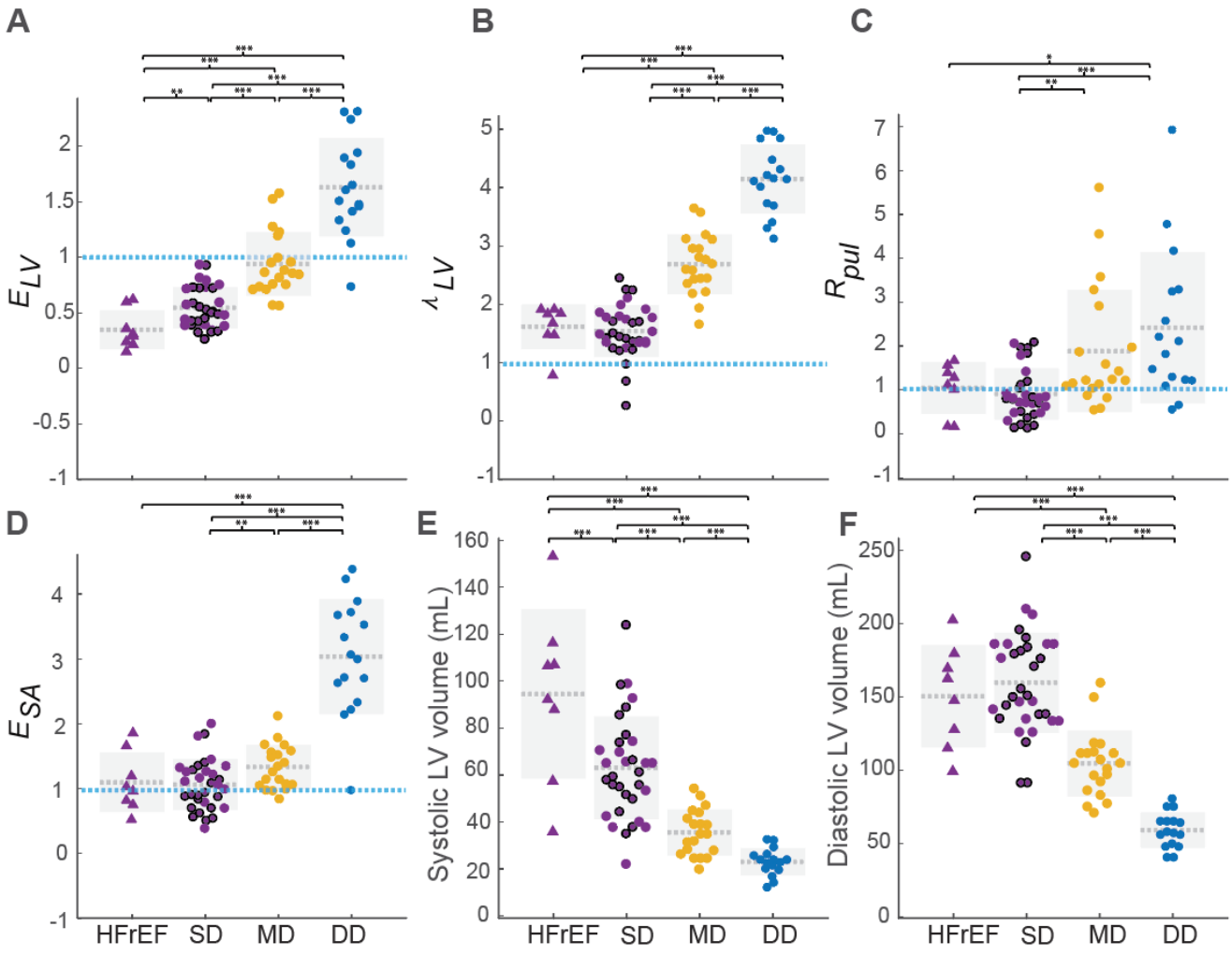

Figure 3.8 Box plots of the optimized parameter values of heart failure groups. Analysis of the optimized parameters gives us an understanding of the mechanistic differences between the three HFpEF groups that cannot be seen by analyzing the clinical data alone. **A.** LV active contractility (mmHg mL^{-1}). **B**. LV passive stiffness (mL^{-1}). **D**. Pulmonary resistance (mmHg s mL^{-1}) **D**. Arterial elastance (mmHg mL^{-1}). All parameter values are plotted relative to the normal model values (blue dashed lines). The light gray dashed line denotes the average, and the gray box contains one standard deviation above and below the mean of each parameter value. **E.** Systolic **F.** Diastolic LV volume (mL) (*p-value <0.05, **p-value <0.01, ***p-value <0.001). Dark border = TMZ HFpEF patients.

3.3 Conclusions for Application of our Methodology to Different HFpEF Data Sets

Taken together, these studies demonstrate that (i) computational models embedded with mechanistic knowledge of cardiovascular system dynamics yield key insights unavailable from ML-based analysis of raw data alone, identifying clusters of HF patients that display distinct patterns of pathophysiological function that are not apparent with EF alone. (ii) This functional phenotyping approach was validated based on RNA transcript analysis of myocardial biopsies from patients with HFpEF. (iii) This approach has the potential to identify HFpEF groups that respond differently to atrial shunt and TMZ therapy.

Chapter 4 Control of Mitochondria Fuel Selection by Calcium

4.1 Acknowledgments

This chapter is being prepared for re-submission to be published as an academic journal article.

Jones, E.; Kandel, S.; Dasika, S.; Nourabadi, N.; Dash, R.; Beard, D. "Control of Cardiac Mitochondrial Fuel Selection by Calcium" Preparing for re-submission *The Journal of Physiology*

4.2 Abstract

Calcium ion concentration modulates the function of several mitochondrial enzymes. Specifically, the kinetic operations of the decarboxylating dehydrogenases, pyruvate dehydrogenase, isocitrate dehydrogenase, and α-ketoglutarate dehydrogenase are all affected by [Ca^{2+}]. Previous studies have shown that despite its ability to affect the function of these dehydrogenases, [Ca^{2+}] does not substantially alter mitochondrial ATP synthesis in vitro under physiological substrate conditions. We hypothesize that, rather than contributing to respiratory control, [Ca^{2+}] plays a role in fuel selection. Specifically, cardiac mitochondria can use different primary carbon substrates (carbohydrates, fatty acids, and ketones) to synthesize ATP aerobically in the living cells. To determine if and how [Ca^{2+}] affects the relative use of carbohydrates versus fatty acids in vitro, we measured oxygen consumption and tricarboxylic acid (TCA) cycle intermediate concentrations in suspensions of cardiac mitochondria with different combinations of

pyruvate and palmitoyl-L-carnitine in the media at various [Ca^{2+}] and ADP infusion rates. Stoichiometric analysis of the data reveals that when both fatty acid and carbohydrate substrates are available, fuel selection is sensitive to both [Ca^{2+}] and ATP synthesis rate. When no Ca^{2+} is added under low ATP-demand conditions, β-oxidation provides roughly half of acetyl-CoA for the citrate synthase reaction with the rest coming from the pyruvate dehydrogenase reaction. Under low demand conditions with increasing [Ca^{2+}], the fuel utilization ratio shifts to increased fractional consumption of pyruvate with 83±10% of acetyl-CoA derived from pyruvate at the highest [Ca^{2+}] evaluated. Under high ATP demand conditions, approximately 80% of acetyl-CoA is derived from pyruvate, regardless of the Ca^{2+} level. Our results suggest that changes in work rate alone are enough to affect a switch to carbohydrate use, whereas in vivo the rate at which this switch happens may depend on mitochondrial calcium.

4.3 Introduction

The kinetic function of several key enzymes involved in energy metabolism is affected by calcium-dependent processes. These include cytosolic enzymes, such as phosphofructokinase (PFK), for which calcium-calmodulin dependent oligomerization of the enzyme affects catalytic activity (Marinho-Carvalho *et al.*, 2006, 2009) , as well as several dehydrogenases present in the mitochondrial matrix (Denton, 2009; Griffiths & Rutter, 2009; Williams *et al.*, 2015). Potentially important sites of Ca^{2+}-mediated stimulation of matrix dehydrogenases are illustrated in **Figure 4.1.**

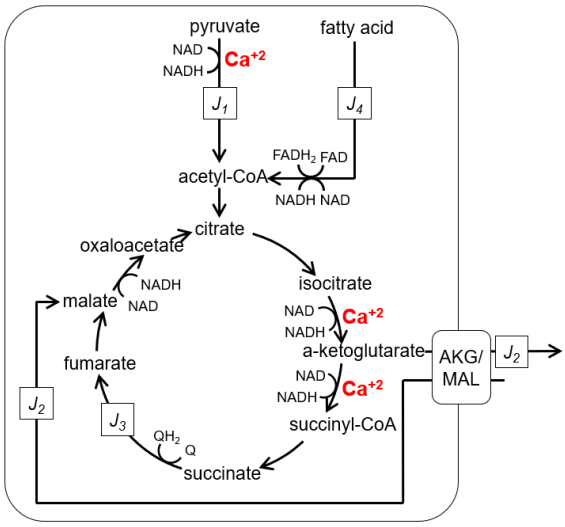

Figure 4.1 Quasi-steady-state TCA cycle fluxes. Definitions of steady-state fluxes used in the quasi-steady analysis of Eqs.(4.5-4.24) are illustrated. The major assumptions are that rates of change bulk concentrations of citrate, isocitrate, succinyl-CoA, succinate, fumarate, and oxaloacetate are much smaller in magnitude than rates of change of pyruvate, fatty acid, α-ketoglutarate, and malate.

It has been proposed that in the myocardium in vivo ATP, ADP, and inorganic phosphate (Pi) levels are maintained at essentially constant levels across different cardiac work rates because changes in ATP consumption rates are balanced by calcium-dependent changes in ATP production rate (Balaban, 2002; Williams *et al.*, 2015). This hypothesis that ATP supply is matched to ATP demand based on an open-loop control system (mediated via mitochondrial Ca^{2+}) lacking a closed-loop feedback control mechanism is broadly invoked(Balaban, 2002; Griffiths & Rutter, 2009). But this open-loop Ca^{2+} activation hypothesis has some critical shortcomings. The first concern is that open-loop control systems are inherently unstable to environmental changes/external perturbations. For open-loop stimulation (such as via Ca^{2+}) to be the sole mechanism controlling myocardial ATP production, the relationship between ATP utilization rate and the stimulatory signal (i.e., mitochondrial Ca^{2+}) would have to re-main exactly invariant under all physiological

conditions. Otherwise, since the heart turns over its total ATP pool several times per minute, even a slight mismatch between supply and demand would be disastrous.

Thus, some degree of closed-loop feedback control is needed to maintain cellular ATP concentration at different levels of ATP hydrolysis. It is impossible for the open-loop Ca^{2+} hypothesis—on its own—to explain respiratory control *in vivo*. The alternative to the open-loop Ca^{2+} hypothesis is that respiratory control is exerted by feedback of ATP hydrolysis products, which was introduced by Chance and Williams concluding that "ADP, and not the inorganic phosphate level, controls the respiration rate"(Chance & Williams, 2006). This conclusion was later supported by *in vivo* measurements on skeletal muscle in the 1980's in the Chance lab (Chance *et al.*, 1985, 1986). Numerous experimental and theoretical studies have supported the feedback hypothesis in the context of skeletal muscle (e.g., (Kushmerick *et al.*, 1992; Jeneson *et al.*, 1996, 2000; Kemp *et al.*, 2007)). Similarly, in the heart the concentrations of ATP hydrolysis products increase with ATP demand in the myocardium *in vivo* (Bache *et al.*, 1999; Gong *et al.*, 1999, 2003; Ochiai *et al.*, 2001; Zhang *et al.*, 2005; Wu *et al.*, 2008, 2009; Beard, 2011) in agreement with the feedback hypothesis and providing additional evidence against the open-loop Ca^{2+} hypothesis. Furthermore, our analyses suggest that a key difference between how oxidative ATP synthesis is controlled in skeletal versus cardiac muscle is that in the heart inorganic phosphate, and not ADP, controls the respiration rate(Wu *et al.*, 2007, 2008, 2009; Beard & Kushmerick, 2009; Wu & Beard, 2009; Beard, 2011).

The third shortcoming of the open-loop Ca^{2+} hypothesis is that, while Ca^{2+} can be shown to stimulate respiration *in vitro* under certain conditions, under physiological substrate conditions the effects of Ca^{2+} on oxidative ATP synthesis *in vitro* are miniscule to modest. Panov and Scaduto (Panov & Scaduto, 1996) showed that with pyruvate and acetyl-carnitine as substrates, Ca^{2+}

stimulates a maximal 3-8% increase in the apparent V_{max} and a 10-18% reduction in the apparent K_m for ADP for ATP synthesis. Wan et al. (Wan *et al.*, 1989) reported a similarly small effect of Ca^{2+} with pyruvate as the substrate. Vinnakota et al.(Vinnakota *et al.*, 2011, 2016) reported increases in the apparent V_{max} of oxidative phosphorylation of cardiac mitochondria of approximately 15-25% when external free [Ca^{2+}] was raised from 0 to 350 nM. These effects are small compared to the 400-500% increase in ATP synthesis associated with the transition from resting to maximal work in the heart *in vivo* (Wu *et al.*, 2008). While the open-loop Ca^{2+} mechanism may be at work *in vivo*, its role in stimulating ATP synthesis *in vivo* may be minor compared to other mechanisms that must be at work (Beard & Kushmerick, 2009) .

Yet there is growing evidence that normal mitochondrial calcium handling is required for normal cardiac mitochondrial metabolic function. Inducible functional knockouts of the cardiac mitochondrial calcium uniporter have demonstrated that inhibition of calcium uptake has an inhibitory effect on ATP production in acute stress responses (Kwong *et al.*, 2015; Luongo *et al.*, 2015). Furthermore, similar knockouts in skeletal muscle have been shown to cause a metabolic shift towards fatty acid oxidation (Kwong *et al.*, 2018).

If Ca^{2+} does not play a major role in matching the steady-state oxidative ATP synthesis rate to ATP demand in the heart *in vivo*, what might be the physiological function of the Ca^{2+} sensitivity of pyruvate dehydrogenase, isocitrate dehydrogenase, and α-ketoglutarate dehydrogenase? Based on the uniporter knockout studies, we hypothesize that Ca^{2+}-mediated effects on these enzymes are involved in substrate selection. Under resting conditions (in the fasted state), roughly 60% of acetyl-CoA supply to the tricarboxylic acid cycle (TCA) in the heart is derived from β-oxidation of fatty acids with the remaining 40% derived from carbohydrate sources (Lassers *et al.*, 1971). During exercise (i.e., high ATP demand), the ratio flips with the majority of

acetyl-CoA supplied from oxidation of carbohydrates (Lassers *et al.*, 1971; Gertz *et al.*, 1988). This phenomenon of increasing the relative contribution from carbohydrate oxidation with increasing ATP synthesis rate is recapitulated *in vitro* in isolated mitochondria from skeletal muscle (Kuzmiak-Glancy & Willis, 2014).

The goals of this study are to: (1.) determine if, similar to what is observed with skeletal muscle mitochondria, changes in ATP synthesis rate cause changes in fuel selection *in vitro* in suspensions of mammalian cardiac mitochondria; (2.) determine if changes in Ca^{2+} concentration cause changes in fuel selection *in vitro*; (3.) determine if and how work load and calcium independently and/or dependently influence mitochondrial substrate selection *in vitro*; and (4.) test the hypothesis that increases in mitochondrial Ca^{2+} contribute to a shift to using relatively more carbohydrate and relatively less fatty acid substrate to fuel oxidative ATP synthesis in cardiac mitochondria as ATP synthesis rate is increased. To achieve these goals, in suspensions of purified rat ventricular mitochondria and in the presence of carbohydrate, fatty acid, and mixed (carbohydrate + fatty acid) reducing substrates, we measured oxygen consumption and bulk metabolite concentration changes during a non-phosphorylating resting state (state 2, leak), where oxygen flux is maintained mainly to compensate for the proton leak at a high chemiosmotic potential, when ATP synthase is not active and, during active oxidative phosphorylation (state 3, OXPHOS) through ATP synthase stimulation by ADP addition. Data were analyzed using a quasi-steady-state mass balance approach to estimate TCA cycle fluxes and fractional fuel utilization under different calcium conditions and at different rates of ATP synthesis.

4.4 Methods

Oxygen consumption rate, and concentrations of several TCA cycle metabolites were measured in suspensions of purified rat ventricular mitochondria in the leak state (with substrate present but with no ADP available as a substrate for oxidative phosphorylation), and under conditions of steady ADP infusion to establish a steady rate of ATP production. These data were used to estimate steady-state substrate oxidation and TCA cycle fluxes under different substrate conditions, different Ca^{2+} concentrations, and different rates of oxidative ATP synthesis.

4.4.1 Isolation of Mitochondria

Cardiac mitochondria were isolated from Male Wistar rats of 300–400 g using protocols that were approved by the Animal Care Committee of the University of Michigan. The rats were anesthetized with an intraperitoneal injection of appropriate amount of ketamine mixed with dexmed followed by heparin. After the rat was in the deep plane of anesthesia, hearts were excised, aortas cannulated, and hearts perfused with ice-cold cardioplegia buffer (containing 25 mM KCl, 100 mM NaCl, 10 mM Dextrose, 25 mM MOPS, 1 mM EGTA) for a 5-minute period. The ventricles of the excised heart were then immediately placed in ice-cold isolation buffer containing 200 mM mannitol, 60 mM sucrose, 5 mM KH_2PO_4, 5 mM MOPS, 1 mM EGTA, and 0.1% BSA. The ventricles were minced with fine scissors for 3 min in a small beaker containing 300 μL of ice-cold isolation buffer to prevent drying of tissue. When the ventricle pieces were about 1 mm^3, 10 mL of isolation buffer without BSA containing 3 units mL^{-1} protease were added to the minced tissue. The solution of minced tissue and isolation buffer without BSA and protease was then transferred to a Potter Elvehjem tissue grinder to be manually homogenized for a maximum of 3 min. After 3 min, 30 mL of ice-cold isolation buffer with BSA and 20 μL of the protease inhibitor

cocktail #3 (VWR cat# 80053-854) were added to the homogenate to a final volume of 40 mL and centrifuged twice at 8000 g for 10 min at 4°C to remove the protease. The supernatant was discarded, and the pellet was resuspended in the isolation buffer to 25 mL and centrifuged at 700 g for 10 min. The pellet was then removed, and the supernatant enriched with mitochondria was spun at 8000 g for 10 min. The pellet, representing the mitochondrial-enriched fraction, was resuspended in 0.2 mL of isolation buffer. To determine the content of intact mitochondria, citrate synthase (CS) activity was assessed as a quantitative marker of the mitochondrial matrix. The enzymatic activity of citrate synthase was assayed following the protocol of Eigentler et al. (Eigentler & et al., 2015).

4.4.2 Respiratory Control Index

The functional integrity of the mitochondria was determined by means of the respiratory control index defined as the maximum rate of oxygen consumption in state-3 oxidative phosphorylation (OXPHOS) divided by the state-2 (leak) state oxygen consumption rate. Both maximal OXPHOS and leak states were assessed with 5 mM pyruvate and 1 mM malate as substrates at 37° C. The OXPHOS state was assessed with ADP added at initial concentration of 500 μM. Oxygen consumption was determined at 37° C using a high-resolution respirometer (Oxygraph-2K, OROBOROS Instruments Gmbh, Innsbruck, Austria). Mitochondria preparations with respiratory control index greater than 8 were considered of acceptable quality for our experiment.

4.4.3 Steady ATP Synthesis Experiments

Purified mitochondria were resuspended in the respiration buffer (90 mM KCl, 1 mM EDTA, 5 mM KH_2PO_4, 50 mM MOPS, 0.1% BSA pH 7.4). The experiments were conducted with

three different substrate combinations: pyruvate + malate (PM), palmitoyl carnitine (PC) + malate, and pyruvate + PC + malate (MIX) with three different $CaCl_2$ concentrations, and two different ADP infusion rates at 37° C and 7.2 pH. The final substrate concentrations were malate (150 uM), pyruvate (350 μM), and PC (20 μM). Total calcium ($CaCl_2$) concentrations were 0, 300, and 400 μM.

4.4.4 Mitochondrial Extraction and Metabolite Assays

To measure the accumulation/utilization of several TCA cycle intermediates (pyruvate, α-ketoglutarate, malate) at various time points, samples were quenched at five different points for the PCM and PM substrate conditions and at seven different time points for the MIX substrate condition in the steady-state protocols (two during the leak state and three to five during the ADP-infusion OXPHOS state.) Samples were quenched adding 800 μL of the experimental sample to 560 μL of 0.6 M perchloric acid (PCA). The quenched samples were than centrifuged at 15,000 rpm for 5 min at 4° C. After the centrifugation, 1200 μL of the supernatant were collected in a different tube and adjusted the pH to between 6.2 and 7.4. The samples were then centrifuged once again for 5 min at 15000 rpm at 4° C and 1 mL of the supernatant of the centrifuged samples were collected to measure the concentration of the desired metabolites enzymatically.

For each of the 18 experimental conditions, samples were collected at 70 and 110 s during the leak state. For the low workload condition, three samples were collected at 200, 240, and 280 s for PM and PC substrates with two additional time points at 320 and 360 s for the MIX substrate conditions. For the high workload condition, samples were collected at 70 and 110 s during the leak state, three samples were collected at 180, 210, and 240 s with two additional time points at

270 and 300 s for the MIX substrate conditions. For each sample collection time, at least 4 (6 for MIX) replicates were obtained.

4.4.5 Metabolite Assays

Metabolite assays were adapted from the methods of Williamson and Corkey (Williamson & Corkey, 1979). For all measured metabolites, NADH-linked assays were used, where the oxidation/reduction of specific metabolites are linked changes in NADH monitored by changes in absorbance at 340 nm. Assays were run using neutralized extract in a final assay volume of 1 mL. Standard curves were obtained daily.

The AKG concentration was measured by coupling glutamate oxaloacetate transaminase (GOT, EC: 2.6.1.1) with malate dehydrogenase (MDH, EC: 1.1.1.37) and adding excess of aspartate (ASP) to the system and obtaining the difference between NADH concentration before and after adding ASP:

$$\mathrm{ASP} + \mathrm{AKG} + \mathrm{NADH} \rightleftharpoons \mathrm{GLU} + \mathrm{MAL} + \mathrm{NAD} \qquad (4.1)$$

Pyruvate (PYR) concentration was measured by adding lactate dehydrogenase (LDH, EC: 1.1.1.27) to catalyze PYR reduction and NADH oxidation and by computing the difference in NADH before and after adding LDH:

$$\mathrm{PYR} + \mathrm{NADH} \rightleftharpoons \mathrm{LAC} + \mathrm{NAD} \qquad (4.2)$$

The enzyme malate dehydrogenase (MDH, EC: 1.1.1.37) catalyzes the conversion of malate (MAL) to oxaloacetate (OAA). Coupling the reaction with glutamate oxaloacetate transaminase (GOT, EC: 2.6.1.1), Malate concentration was estimated by computing the difference between NADH concentration before and after adding GOT and MDH:

$$\mathrm{MAL} + \mathrm{NAD} \rightleftharpoons \mathrm{OAA} + \mathrm{NADH} \quad (4.3)$$

$$\mathrm{OAA} + \mathrm{Glut} \rightleftharpoons \mathrm{AKG} + \mathrm{ASP} \quad (4.4)$$

4.4.6 Quasi-steady State Flux Analysis

In total, oxygen consumption rate and metabolite intermediate concentrations were assayed under 27 different experimental conditions: (leak state + 2 OXPHOS states) × (3 Ca2+ conditions) × (3 substrate conditions). Under these different conditions, citrate, succinate, fumarate, and oxaloacetate remained below the limit of detection (< 15 μM) of the assays employed. Based on this observation, we constructed a reduced stoichiometric mass conservation model (**Figure 4.1**) in which the fluxes J_1 (rate of acetyl-CoA production from pyruvate dehydrogenase), J_2 (rate of α-ketoglutarate production), J_3 (rate of succinate dehydrogenase/complex II flux), and J_4 (rate of acetyl-CoA production from β-oxidation) are unknowns to be estimated based on the metabolite and oxygen flux data at each experimental condition. The flux J_3 is assumed to be equal to $J_1 + J_4 - J_2$ under steady-state conditions. Thus, under each steady-state condition, there are three unknown steady-state fluxes, J_1, J_2, and J_4 to be estimated from data on oxygen consumption rate and metabolite concentrations. We use the notation $J_1^{(2)}$, $J_2^{(2)}$, and $J_4^{(2)}$ to represent fluxes in the state-2 (leak) state, and $J_1^{(3)}$, $J_2^{(3)}$, and $J_4^{(3)}$ to represent fluxes in the state-3 (OXPHOS) state. In all states, the oxygen consumption flux is stoichiometrically equated to half of the rate of generation of electron donors (NADH, $FADH_2$, QH_2):

$$J_{O_2} = \frac{1}{2}(5J_1 + 6J_4 - 2J_2) \quad (4.5)$$

For the PM condition, $J_4 = 0$, and we have the following equations for the leak state:

$$J_{O2}^{(2)} = \frac{1}{2}\left(5J_1^{(2)} - 2J_2^{(2)}\right) \quad (4.6)$$

$$C_{PYR}(t) = C_{0,PYR} - J_1^{(2)}t \quad (4.7)$$

$$C_{AKG}(t) = C_{0,AKG} + J_2^{(2)}t \quad (4.8)$$

$$C_{MAL}(t) = C_{0,MAL} - J_2^{(2)}t, \quad t < T, \quad (4.9)$$

where $C_{PYR}(t)$, $C_{AKG}(t)$, and $C_{MAL}(t)$ are the concentrations of pyruvate and α-ketoglutarate, $C_{0,PYR}$ and $C_{0,AKG}$ are the initial concentrations, and T is the initial time of ADP infusion. These equations assume a linear consumption of pyruvate, linear production of α-ketoglutarate, and a constant rate of oxygen consumption.

The equations for the OXPHOS state, which is initiated at $t = T$, are

$$J_{O2}^{(3)} = \frac{1}{2}\left(5J_1^{(3)} - 2J_2^{(3)}\right) \quad (4.10)$$

$$C_{PYR}(t) = C_{0,PYR} - J_1^{(2)}T - J_1^{(3)}(t - T) \quad (4.11)$$

$$C_{AKG}(t) = C_{0,AKG} + J_2^{(2)}T + J_2^{(3)}(t - T) \quad (4.12)$$

$$C_{MAL}(t) = C_{0,MAL} - J_2^{(2)}T - J_2^{(3)}(t - T), \quad t \geq T. \quad (4.13)$$

These equations assume a piecewise linear time course of pyruvate, α-ketoglutarate, and malate, as illustrated in **Figure 4.3A**.

For experiments with PM substrate (at three different [Ca^{2+}] concentrations and two different ADP infusion rates for the OXPHOS state), Equations (1) and (2) are fit to experimental data on $C_{PYR}(t)$, $C_{AKG}(t)$, $J_{O2}^{(2)}$, and $J_{O2}^{(3)}$ to obtain estimates of unknowns $J_1^{(2)}$, $J_2^{(2)}$, $J_1^{(3)}$, $J_2^{(3)}$, $C_{0,PYR}$, $C_{0,MAL}$, and $C_{0,AKG}$. Even though we used initial pyruvate, α-ketoglutarate, and malate concentrations of 350, 0, and 150 μM in the experiments, respectively, we allow $C_{0,PYR}$, $C_{0,MAL}$, and $C_{0,AKG}$ to be estimated in order to account for experimental variability and contamination in sample prep.

For PCM substrate, the equations are:

$$J_{O2}^{(2)} = \frac{1}{2}\left(6J_4^{(2)} - 2J_2^{(2)}\right) \tag{4.14}$$

$$C_{AKG}(t) = C_{0,AKG} + J_2^{(2)}t \tag{4.15}$$

$$C_{MAL}(t) = C_{0,MAL} - J_2^{(2)}t, \quad t < T, \tag{4.16}$$

and

$$J_{O2}^{(3)} = \frac{1}{2}\left(6J_4^{(3)} - 2J_2^{(3)}\right) \tag{4.17}$$

$$C_{AKG}(t) = C_{0,AKG} + J_2^{(2)}T + J_2^{(3)}(t-T) \tag{4.18}$$

$$C_{MAL}(t) = C_{0,MAL} - J_2^{(2)}T - J_2^{(3)}(t-T), \quad t \geq T, \tag{4.19}$$

for unknowns $J_2^{(2)}, J_4^{(2)}, J_2^{(3)}, J_4^{(3)}$, $C_{0,MAL}$, and $C_{0,AKG}$.

With MIX substrate, the governing equations are:

$$J_{O2}^{(2)} = \frac{1}{2}\left(5J_1^{(2)} + 6J_4^{(2)} - 2J_2^{(2)}\right) \tag{4.20}$$

$$C_{PYR}(t) = C_{0,PYR} - J_1^{(2)}t \tag{4.21}$$

$$C_{AKG}(t) = C_{0,AKG} + J_2^{(2)}t \tag{4.22}$$

$$C_{MAL}(t) = C_{0,MAL} - J_2^{(2)}t, \quad t < T, \tag{4.23}$$

and

$$J_{O2}^{(3)} = \frac{1}{2}\left(5J_1^{(3)} + 6J_4^{(3)} - 2J_2^{(3)}\right) \tag{4.24}$$

$$C_{PYR}(t) = C_{0,PYR} - J_1^{(2)}T - J_1^{(3)}(t-T) \tag{4.25}$$

$$C_{AKG}(t) = C_{0,AKG} + J_2^{(2)}T + J_2^{(3)}(t-T) \tag{4.26}$$

$$C_{MAL}(t) = C_{0,MAL} - J_2^{(2)}T - J_2^{(3)}(t-T), \quad t \geq T, \tag{4.27}$$

for unknowns $J_1^{(2)}, J_2^{(2)}, J_4^{(2)}, J_1^{(3)}, J_2^{(3)}, J_4^{(3)}, C_{0,PYR}$, $C_{0,MAL}$, and $C_{0,AKG}$.

For each substrate and [Ca^{2+}] condition, the maximal likelihood estimates for the unknowns and for the covariances of the unknowns are obtained using the methods of Landaw and DiStefano (Landaw & DiStefano, 1984). The goodness of fit to the data and uncertainty in flux estimates are evaluated using Monte-Carlo sampling from the distributions associated with the maximally likely means and covariances for the estimated unknowns from the governing equations. For a given substrate and [Ca^{2+}] condition, an individual estimate of the unknown fluxes and initial conditions yields piecewise linear fits to the pyruvate and α-ketoglutarate data and pointwise estimates of J_{O2} for the leak state and the two OXPHOS states. By drawing 10,000 samples from the flux and initial condition distributions for each substrate and [Ca^{2+}] condition, we estimate the uncertainties in the estimates of the unknowns.

4.4.7 Leak current (J_L) Estimation

The contributions of leak current (J_L) to the overall oxidative flux were estimated for the various experimental conditions probed based on the flux estimates reported in **Table 4.2**.

Using the following equations, we estimated J_L as the difference between the total rate of charge pumping via the respiratory chain (J_R) and the rate of charge consumption for ATP synthesis (J_S).

Estimation of the Charge Pumping Rate via the Respiratory Chain (J_R)

To estimate J_R, the rate of electron donor generation NADH (J_{NADH}) and $FADH_2$ & QH_2 ($J_{FADH2\ \&\ QH2}$) associated with the flux estimates of electron donor generating enzymes involved in J_1 (rate of acetyl-CoA production from pyruvate dehydrogenase), J_4 (rate of acetyl-CoA production from β-oxidation) and J_3 (rate of succinate dehydrogenase/complex II flux), were

assumed to be equal to $J_1 + J_4 - J_2$ under steady state conditions and accounted for. Thus, the rate of NADH electron donor generation (J_{NADH}) is calculated as:

$$J_{NADH} = (4)J_1 + (4)J_4 - J_2 \quad (4.28)$$

From the stoichiometric assumption that each Complex I donor (NADH) generated is associated with 10 charges pumped across the inner membrane, J_{NADH} is equal to:

$$J_{NADH} = (40)J_1 + (40)J_4 - (10)J_2 \quad (4.29)$$

Likewise, the rate of $FADH_2$ & QH_2 ($J_{FADH2\ \&\ QH2}$) electron donor generation is calculated as:

$$J_{\mathrm{FADH2\ \&\ QH2}} = J_1 + (2)J_4 - J_2 \quad (4.30)$$

From the stoichiometric assumption that each Complex II donor ($FADH_2$ and QH_2) generated is associated with 6 charged pumped, $J_{FADH2\ \&\ QH2}$ is equal to:

$$J_{\mathrm{FADH2\ \&\ QH2}} = (6)J_1 + (12)J_4 - (6)J_2 \quad (4.31)$$

By adding the rate of electron donor generation of J_{NADH} (4.29) and $J_{FADH2\ \&\ QH2}$ (4.31), the rate of charge pumping via the respiratory chain (J_R) is:

$$J_R = (46)J_1 + (52)J_4 + (-16)J_2 \quad (4.32)$$

Estimation of the Charge Consumption Rate for ATP Synthesis (J_S)

To calculate the J_S, we must account for the rate of ATP synthesis (I) and the number of charges used to synthesize ATP. The rate of ATP synthesis (I) can be calculated by adding the ATP produced by 1) substrate level phosphorylation via de succinate dehydrogenase/complex II flux (J_3 assumed to be equal to $J_1 + J_4 - J_2$ under steady state conditions) and 2) oxidative phosphorylation in which each ATP generation assumes a stoichiometry of 8/3 for rate of charge consumption by ATPase (Nicholls *et al.*, 2013). Thus, the rate of ATP synthesis (I) is:

$$I = (J_1 + J_4 - J_2) + \left(\frac{8}{3}\right)(rate\ of\ charge\ consumption\ by\ ATPase) \quad (4.33)$$

Solving for the *rate of charge consumption by ATPase* gives us:

$$rate\ of\ charge\ consumption\ by\ ATPase = \left(\frac{8}{3}\right)(I - J_1 - J_4 + J_2) \quad (4.34)$$

Yet, to account for the total number of charges used to synthesize ATP, we must also account for the 1 charge transferred by the adenine nucleotide translocase (ANT).

Thus, rate of charge consumption for ATP synthesis (J_S) is:

$$J_S = \left(\frac{8}{3}\right)(I - J_1 - J_4 + J_2) + I \quad (4.35)$$

Which solved is:

$$J_S = \left(\frac{11}{3}\right) I - \left(\frac{8}{3}\right) J_1 - \left(\frac{8}{3}\right) J_4 + \left(\frac{8}{3}\right) J_2 \quad (4.36)$$

Leak Current (J_L) Calculation

The leak current (J_L) is estimated as the difference between the total rate of charge pumping via the respiratory chain (J_R) (4.32) and the rate of charge consumption for ATP synthesis (J_S) (4.36.):

$$J_L = \left(46 - \frac{8}{3}\right) J_1 + \left(52 - \frac{8}{3}\right) J_4 + \left(-16 + \frac{8}{3}\right) J_2 - \left(\frac{11}{3}\right) I \quad (4.37)$$

4.5 Results

4.5.1 Oxygen Consumption Rates

Figure 4.2A shows representative traces of oxygen consumption flux (J_{O2}) in the leak state (t < 120 s), during low-rate ADP infusion (I = 78.9 nmol ADP min^{-1} mL^{-1} during 120 s > t < 310 s) and after stopping ADP infusion (t > 310 s). In this and all other experiments, mitochondria

were added at 0.67 units of citrate synthase (U CS) activity to 2 mL of experimental buffer. Thus, expressing the ADP infusion rate (equal to ATP synthesis rate) relative to mitochondrial citrate synthase activity (I = 234 nmol min^{-1} $(U\ CS)^{-1}$) for the low ADP infusion rate case. Representative traces of J_{O2} are shown for three different substrate conditions: pyruvate and malate (PM) at initial concentrations of 350 μM and 150 μM, respectively; palmitoyl carnitine and malate (PCM) at initial concentrations of 20 μM and 150 μM, respectively; and pyruvate, palmitoyl carnitine, and malate (MIX) at initial concentrations of 350 μM, 20 μM, and 150 μM, respectively. Fig. 2B shows similar traces obtained in the leak state (t < 120 s) during high rate of ADP infusion (I = 356 nmol min^{-1} $(U\ CS)^{-1}$, 120 s > t < 125 s) and after stopping ADP infusion (t > 245 s). These two ADP infusion rates correspond to roughly 1/3 and 1/2 of the V_{max} of mitochondrial ATP synthesis *in vitro*.

Observations from N = 4-6 biological replicates of steady-state J_{O2} during ATP synthesis (OXPHOS state) and at three different total calcium ($CaCl_2$) concentrations of 0, 300, and 400 μM are summarized in **Figure 4.2 C, D**. As expected, J_{O2} tends to be higher when fatty the acid substrate (PCM) is oxidized compared to carbohydrate (PM). The estimated effective P/O ratios under the different calcium and substrate conditions are listed in **Table 4.1**. Here, the expected trend of lower P/O ratio with PCM compared to PM is observed. Estimated P/O ratios for the MIX substrate cases tend to fall between the values estimated for PM and for PCM, although this is not the case for every combination of ATP-synthesis/ADP-infusion rate and calcium level.

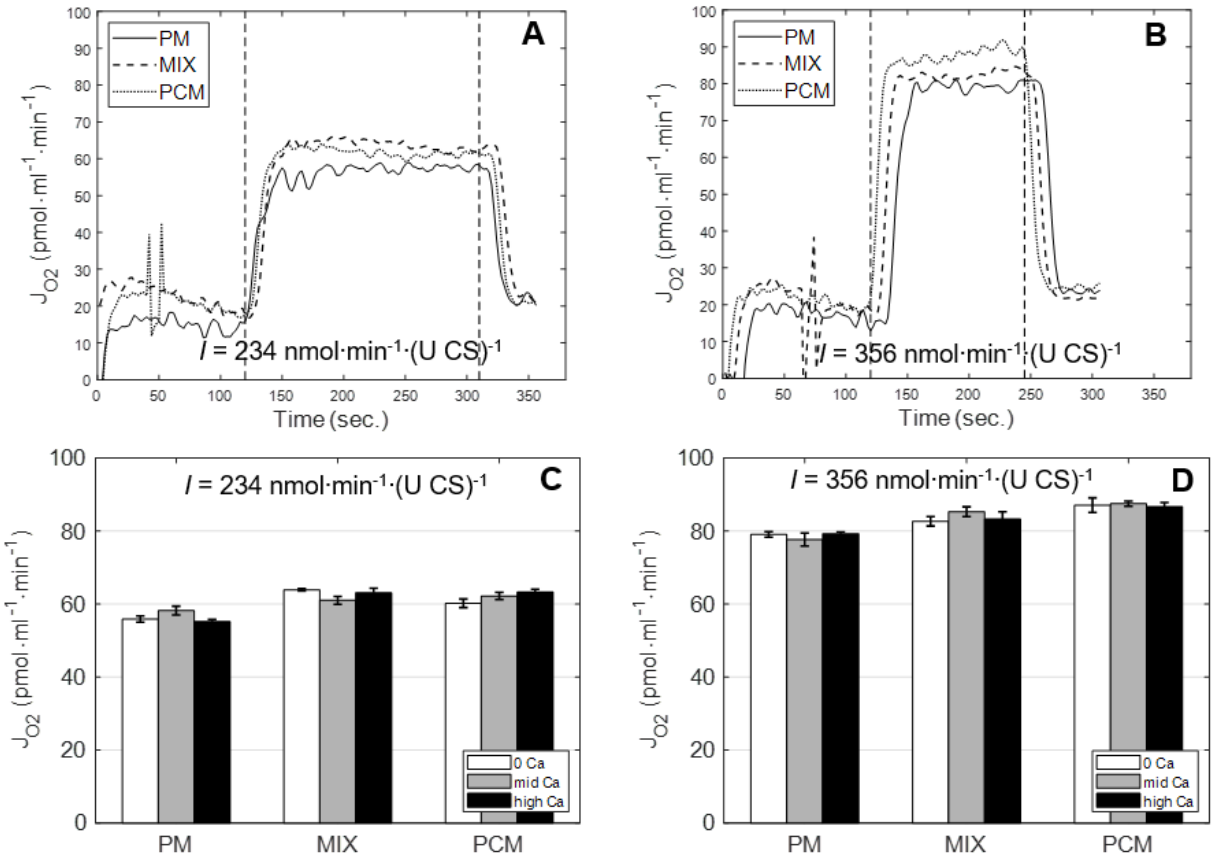

Figure 4.2 Oxygen fluxes measured by high-resolution respirometry. For all data mitochondria are suspended in a 2-ml Oroboros Oxygraph respirometry chamber at 0.337 U CS per ml. A. Time courses of oxygen consumption rate J_{O2} are shown for buffer total [Ca^{2+}] = 0, 300 and 400 μM (with 1 mM EGTA) and three different substrate conditions. Data for t < 0 correspond to the leak state. Infusion of ADP at I = 234 nmol min^{-1} $(UCS)^{-1}$ begins at t = 120 and ends at t = 310 sec. B. Time courses of J_{O2} are shown for [Ca^{2+}] = 0, 300 and 400 μM and the three different substrate conditions with ADP infusion rate I = 356 nmol min^{-1} $(UCS)^{-1}$. Infusion begins at t = 120 and ends at t = 245 sec. C. Data on OXPHOS state J_{O2} from N = 3 replicates are shown as Mean ± SEM for three Ca^{2+} concentrations and three different substrate conditions, and for low ATP demand (I = 234 nmol min^{-1} $(UCS)^{-1}$). D. Data on OXPHOS state J_{O2} from N = 3 replicates are shown as Mean ± SEM for three Ca^{2+} concentrations and three different substrate conditions, and for high ATP demand (I = 356 nmol min^{-1} $(UCS)^{-1}$). Abbreviations are PM: pyruvate + malate; MIX: pyruvate + palmitoyl-carnitine + malate; PCM: palmitoyl-carnitine + malate.

These measurements on their own do does not provide enough information to quantify the substrate oxidation and TCA cycle fluxes under the different experimental conditions. Additional data on metabolite concentrations were obtained that, combined with the oxygen flux data, allowed us to estimate quasi-steady-state fluxes.

Table 4.1 Summary of oxygen consumption data

		Leak state	OXPHOS I = 234 nmol min^{-1} $(UCS)^{-1}$		OXPHOS I = 356 nmol min^{-1} $(UCS)^{-1}$	
		J_{O2}	J_{O2}	P/O	J_{O2}	P/O
PM	$[Ca^{2+}] = 0$	16.6± 0.28	55.9± 0.85	2.09 ± 0.03	79.1 ± 0.76	2.25 ± 0.02
	$[Ca^{2+}] = 300$ μM	17.0± 0.71	58.2± 1.2	2.01 ± 0.04	77.7 ± 1.78	2.29 ± 0.05
	$[Ca^{2+}] = 400$ μM	16.1 ± 0.21	55.2 ± 0.58	2.11 ± 0.02	79.3± 0.45	2.24 ± 0.01
MIX	$[Ca^{2+}] = 0$	22.1 ± .83	63.9 ± 0.3	1.83 ± 0.01	82.7 ± 1.3	2.15 ± 0.03
	$[Ca^{2+}] = 300$ μM	20.9 ± .75	61.0 ± 1.08	1.90 ± 0.03	85.3 ± 1.35	2.09 ± 0.03
	$[Ca^{2+}] = 400$ μM	21.0 ± .006	63.1 ± 1.26	1.85 ± 0.04	83.3 ± 1.99	2.13 ± 0.05
PCM	$[Ca^{2+}] = 0$	21.0 ± 0.76	60.2 ± 1.17	1.94 ± 0.04	87.1± 1.99	2.04 ± 0.05
	$[Ca^{2+}] = 300$ μM	20.3 ± .37	62.2 ± .98	1.88 ± 0.03	87.5 ± .69	2.03 ± 0.16
	$[Ca^{2+}] = 400$ μM	21.1 ± .56	63.3 ± .77	1.84 ± 0.02	86.7 ± 1.14	2.05 ± 0.03

All fluxes reported in units of nmol min^{-1} $(UCS)^{-1}$.

4.5.2 Metabolite Concentrations

The purified mitochondria system was quenched and extracted for assay of intermediate concentrations at five different time points for the PCM and PM substrate conditions and at seven different time points for the MIX substrate condition, as indicated in the protocol detailed in the methods section of this chapter. For the low ADP infusion rate experiments (I = 234 nmol min^{-1} $(U\ CS)^{-1}$) measurements were made at 70 and 110 s following substrate addition (during the leak state) and at 200, 240, and 280 s for PM and PCM substrates with two additional time points at 320 and 360 s for the MIX substrate conditions during the low ADP-infusion OXPHOS state. For the high ADP infusion rate experiments (I = 356 nmol min^{-1} $(U\ CS)^{-1}$), measurements were made at time points 70 and 110 s following substrate addition for the leak state and at 180, 210, and 240 s with two additional time points at 270 and 300 s for the MIX substrate conditions during the

ADP-infusion OXPHOS state. Data on pyruvate, malate and α-ketoglutarate concentrations from the PYR, PC, and MIX substrate experiments are shown in Figs. 3, 4, and 5.

Figure 4.3A shows data obtained using pyruvate + malate (PM) as the substrate, at 0, 300, and 400 μM added $CaCl_2$, for both ADP infusion rates. In the experimental buffer containing 1 mM EGTA, theses total calcium concentrations are associated with approximately 0, 100, and 200 nM external free [Ca^{2+}]. Under these calcium conditions (I = 234 nmol min^{-1} (U CS)$^{-1}$), roughly 40 μM of pyruvate is consumed, and 25-50 μM of α-ketoglutarate is produced over the 200 s ADP infusion time period. Thus, the TCA cycle flux from citrate to α-ketoglutarate is greater than the α-ketoglutarate dehydrogenase flux. Much of the carbon entering the TCA cycle as citrate exits as α-ketoglutarate, rather than continuing to complete the cycle and resynthesize citrate from oxaloacetate. Instead, as has been observed previously, the exogenous malate consumed via malate dehydrogenase is the primary source of oxaloacetate for the citrate synthase reaction under these conditions(LaNoue *et al.*, 1970). A similar phenomenon is observed at the higher ADP infusion rate and under all Ca^{2+} concentrations.

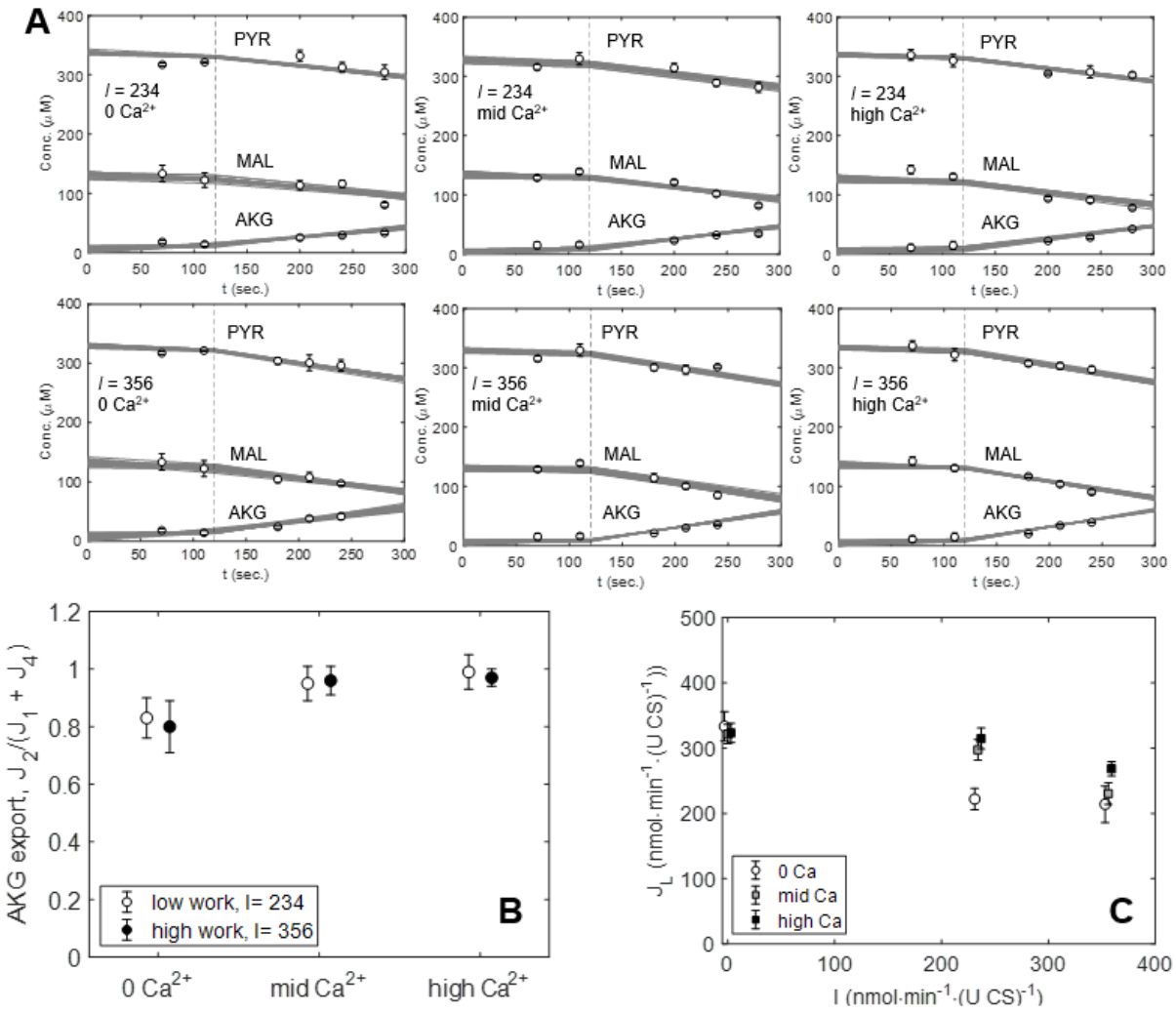

Figure 4.3 Time courses of pyruvate, malate and α-ketoglutarate during leak and OXPHOS states for PM (pyruvate + malate) substrate conditions. Straight lines are 25 Monte-Carlo samples representing uncertainty of fits of Eqs. (4.6, 4.7,4.8, 4.9, 4.10, 4.13,4.12, 4.11) to the concentration and J_{O2} data. A. Data and model fits are shown for the [Ca^{2+}] = 0, 300 μM and 400 μM conditions, with low ATP demand (I = 234 nmol min^{-1} $(UCS)^{-1}$) and high ATP demand (I = 356 nmol min^{-1} $(UCS)^{-1}$). B. Estimated α-ketoglutarate (J_2/J_1+J_4) export for the [Ca^{2+}] = 0, 300 μM and 400 μM conditions, with low ATP demand (I = 234 nmol min^{-1} $(UCS)^{-1}$) and high ATP demand (I = 356 nmol min^{-1} $(UCS)^{-1}$). C. Estimated leak current. The leak current J_L is plotted as a function of ATP demand. Estimates are obtained by combining data for all substrate conditions. (No substrate-dependent differences in J_L were detected.)

Under the palmitoyl-carnitine + malate (PCM) substrate conditions, no pyruvate consumption or production is observed (**Figure 4.4A**) with α-ketoglutarate production in the same range as observed under the other substrate conditions.

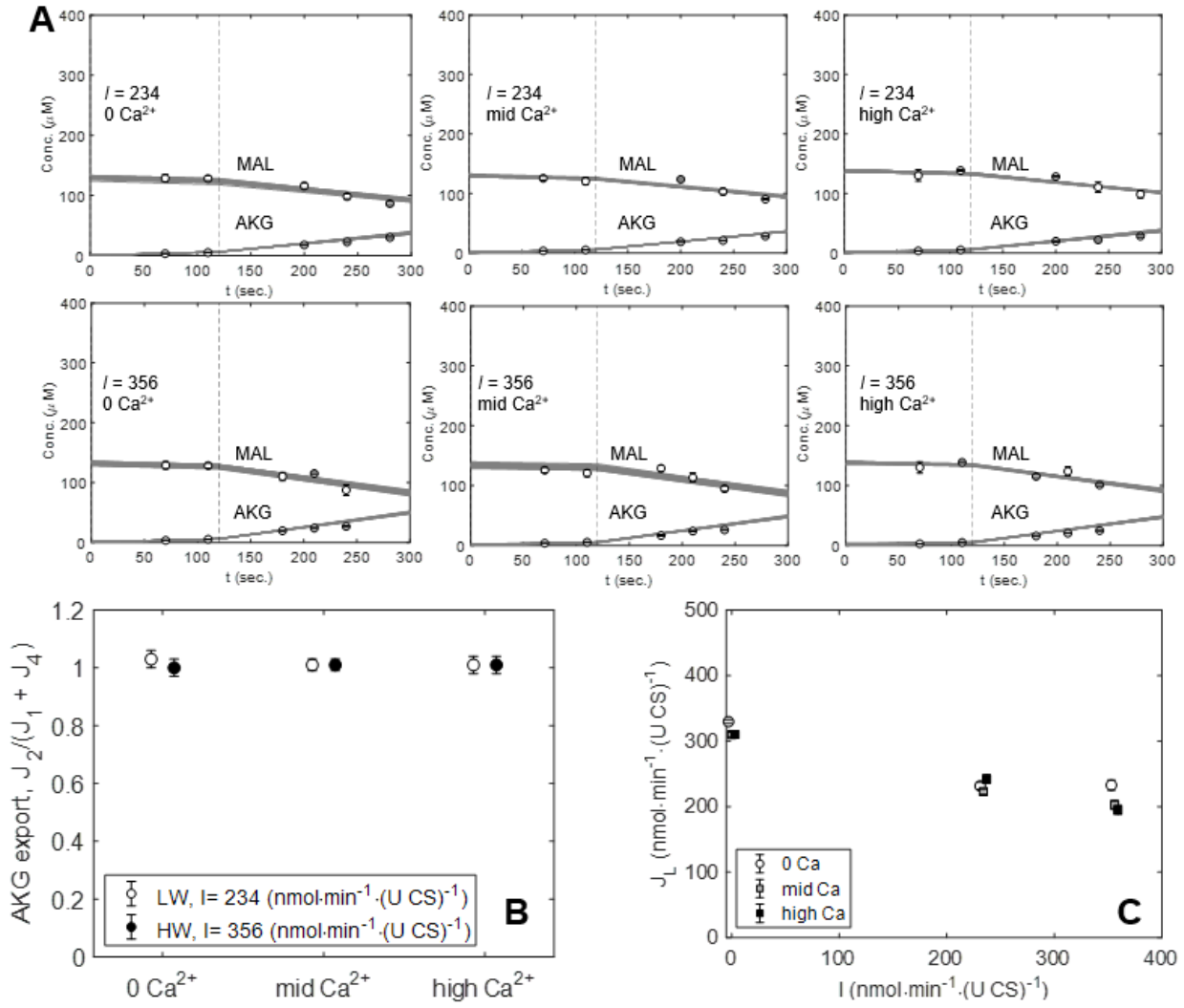

Figure 4.4 Time courses of malate and α-ketoglutarate during leak and OXPHOS states for PCM (palmitoyl-carnitine + malate) substrate conditions. Straight lines are 25 Monte-Carlo samples representing uncertainty of fits of Eqs. 4.14, 4.15, 4.16, 4.17and 4.18 to the concentration and J_{O2} data. A. Data and model fits are shown for the $[Ca^{2+}]$ = 0, 300 μM and 400 μM conditions, with low ATP demand (I = 234 nmol min^{-1} (UCS)$^{-1}$) and high ATP demand (I = 356 nmol min^{-1} (UCS)$^{-1}$). B. Estimated α-ketoglutarate (J_2/J_1+J_4) export for the $[Ca^{2+}]$ = 0, 300 μM and 400 μM conditions, with low ATP demand (I = 234 nmol min^{-1} (UCS)$^{-1}$) and high ATP demand (I = 356 nmol min^{-1} (UCS)$^{-1}$). C. Estimated leak current. The leak current J_L is plotted as a function of ATP demand. Estimates are obtained by combining data for all substrate conditions. (No substrate-dependent differences in J_L were detected.)

Under mixed (MIX) substrate conditions (Fig. 5A), the pyruvate consumption rate is much lower than observed with PM. Although the pyruvate consumption rates are lower than in the PM condition, the α-ketoglutarate production rates are similar to those observed under PM, indicating that a similarly low fraction of the citrate to α-ketoglutarate flux is continuing on to complete the cycle through α-ketoglutarate dehydrogenase, succinyl-CoA synthetase, succinate dehydrogenase, and fumarase reactions.

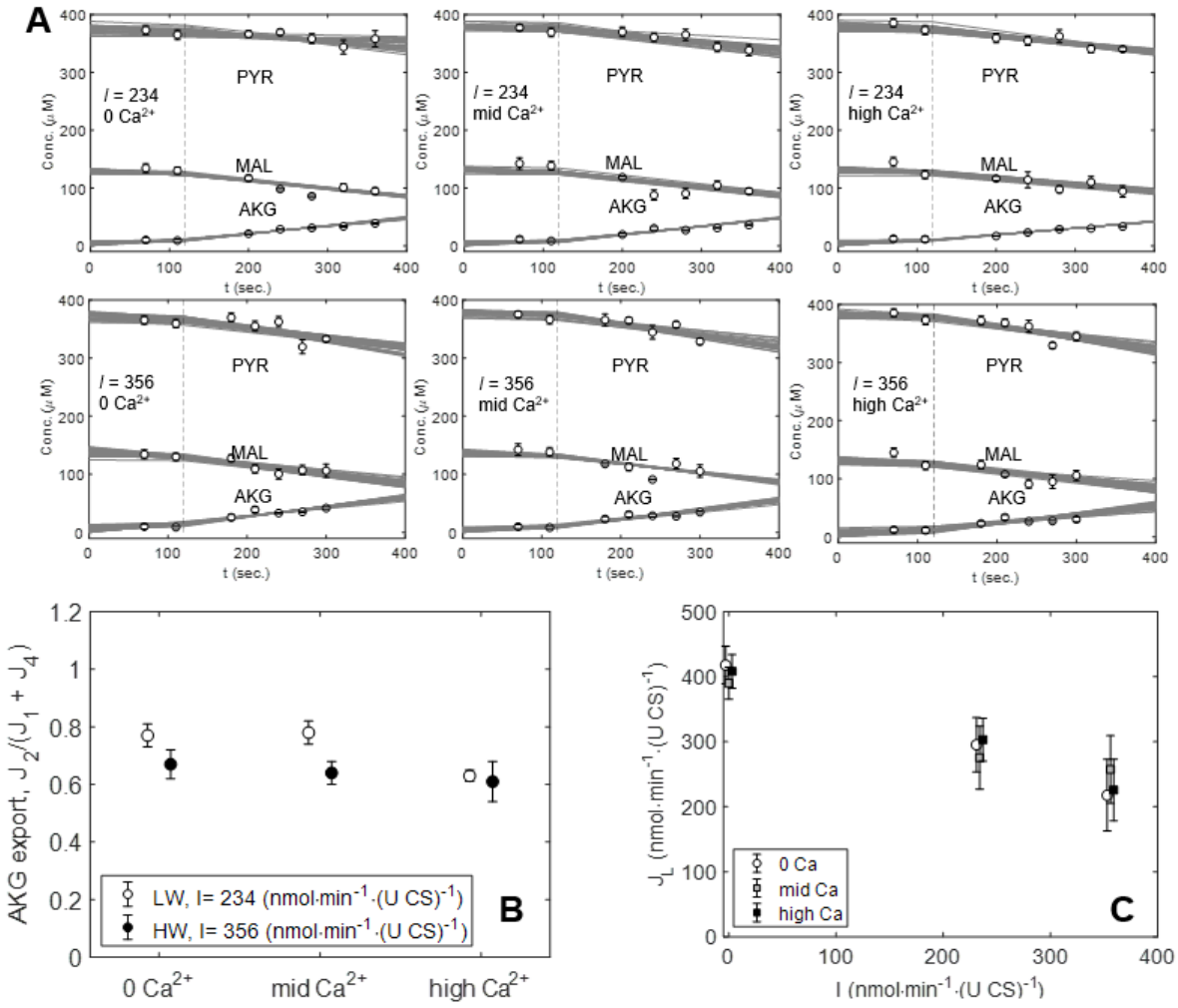

Figure 4.5 Time courses of pyruvate, malate and α-ketoglutarate during leak and OXPHOS states for MIX (pyruvate + palmitoyl-carnitine + malate) substrate conditions. Straight lines are 25 Monte-Carlo samples representing

uncertainty of fits of Eqs. 4.20,4.21,4.22, 4.23, 4.24, 4.26, 4.27 to the concentration and J_{O2} data. A. Data and model fits are shown for the $[Ca^{2+}]$ = 0, 300 μM and 400 μM conditions, with low ATP demand (I = 234 nmol min^{-1} $(UCS)^{-1}$) and high ATP demand (I = 356 nmol min^{-1} $(UCS)^{-1}$). B. Estimated α-ketoglutarate (J_2/J_1+J_4) export for the $[Ca^{2+}]$ = 0, 300 μM and 400 μM conditions, with low ATP demand (I = 234 nmol min^{-1} $(UCS)^{-1}$) and high ATP demand (I = 356 nmol min^{-1} $(UCS)^{-1}$). C. Estimated leak current. The leak current J_L is plotted as a function of ATP demand. Estimates are obtained by combining data for all substrate conditions. (No substrate-dependent differences in J_L were detected.)

4.5.3 Fuel Utilization in Vitro

Table 4.2 lists the estimated fluxes and uncertainties for each condition. Uncertainties are indicated as ± 1 SD confidence range. The estimates for J_{O2} in **Table 4.2**, which arise from the fits of the appropriate set of governing equations to the data, can be compared directly to the direct measurements in **Table 4.1**. The close correspondence between the measurements in **Table 4.1** and the estimates in **Table 4.2** (that are based on fitting both the data in **Table 4.1** and the concentration data) provides an independent validation of the steady-state analysis.

Table 4.2 Estimated steady-state fluxes

	$CaCl_2$ (μM)	J_1	J_2	J_4	J_{O2}	J_1	J_2	J_4	J_{O2}	J_1	J_2	J_4	J_{O2}
PM	0	11.2±2.01	11.4±5.02	0	16.6±0.20	33.6±1.48	28.2±3.60	0	55.7±0.84	46.6±2.50	37.5±6.22	0	79.0±0.77
	300	9.6±1.31	7.1±3.24	0	17.0±0.50	37.8±1.45	36.2±3.43	0	58.3±1.21	50.3±1.57	48.3±3.56	0	77.6±1.80
	400	9.8±1.30	7.6±3.24	0	17.0±0.15	39.0±1.45	38.8±3.57	0	58.8±0.58	51.7±1.00	50.0±2.45	0	79.3±0.45
MIX	0	6.8±2.86	11.1±3.82	5.5±2.38	22.3±.59	13.6±1.37	24.3±1.37	18.0±5.76	63.7±0.29	32.5±6.15	28.4±2.44	10.0±5.17	82.7±1.02
	300	6.0±2.51	8.38±3.05	4.9±2.09	21.3±.42	23.3±5.47	25.5±1.19	9.4±4.56	61.1±1.08	32.6±5.81	27.6±2.15	10.5±4.88	85.3±1.36
	400	6.6±2.73	9.7±2.73	5.1±2.24	22.0±.45	26.9±3.73	20.43±.53	5.43±3.11	63.1±1.27	36.4±5.15	26.2±3.96	6.14±4.27	83.3±.20
PCM	0	0	8.2±0.59	8.9±0.27	18.4±0.54	0	31.5±1.09	30.6±.53	60.2±1.18	0	43.0±1.44	42.8±0.80	85.3±1.94
	300	0	7.1±0.89	8.2±0.31	17.3±0.26	0	30.3±.77	30.1±.41	60.0±.98	0	42.3±1.25	42.0±0.69	83.9±0.69
	400	0	6.7±1.17	8.1±0.41	17.7±.40	0	31.2±1.49	31.0±.56	61.8±.77	0	42.5±1.47	41.9±0.62	83.2±1.16

All fluxes reported in units of nmol min^{-1} $(UCS)^{-1}$.

Representative piecewise linear fits to the concentration data are shown in **Figure 4.3** (PM substrate), **Figure 4.4** (PCM substrate), and **Figure 4.5** (MIX substrate) for all three $[Ca^{2+}]$ conditions. For clarity of presentation only 25 of the 10,000 independent fits are shown. The piecewise linear steady-state model effectively matches the data, and the Monte-Carlo sampling effectively matches to the uncertainty in the data, illustrated as mean ± SEM.

The flux estimates are used to estimate the fractional production of α-ketoglutarate under different OXPHOS loads and Ca^{2+} concentrations. Despite the sensitivity of α-ketoglutarate to [Ca^{2+}] (Qi *et al.*, 2011), for PM substrate the fractional export of α-ketoglutarate, $J_2/(J_1 + J_4)$, does not increase with increasing [Ca^{2+}] (**Figure 4.3** and **Table 4.3**). Analysis of the data from PCM substrate experiments yields estimates of α-ketoglutarate export that are effectively 100% of acetyl-CoA production and do not depend on ATP production/demand rate or [Ca^{2+}] (**Figure 4.4B** and **Table 4.3**). With mixed substrate (**Figure 4.5B** and **Table 4.3**) the fractional α-ketoglutarate export is in the range of 60- 80% and does not show a clear dependency on demand or [Ca^{2+}].

Table 4.3 Estimated fluxes ratios

		Leak state fluxes			OXPHOS I = 234 nmol min^{-1} $(UCS)^{-1}$			OXPHOS I = 356 nmol min^{-1} $(UCS)^{-1}$		
	$CaCl_2$	$J_2/(J_1+J_4)$	$J_1/(J_1+J_4)$	$J_4/(J_1+J_4)$	$J_2/(J_1+J_4)$	$J_1/(J_1+J_4)$	$J_4/(J_1+J_4)$	$J_2/(J_1+J_4)$	$J_1/(J_1+J_4)$	$J_2/(J_1+J_4)$
	(μM)	Fractional AKG efflux	Fractional PM use	Fractional FA use	Fractional AKG efflux	Fractional PM use	Fractional FA use	Fractional AKG efflux	Fractional PM use	Fractional AKG efflux
PM	0	0.91±0.29	--	--	0.83±0.07	--	--	0.80±0.09	--	--
	300	0.67±0.24	--	--	0.95±0.06	--	--	0.96±0.05	--	--
	400	0.71±0.24	--	--	0.99±0.06	--	--	0.97±0.03	--	--
MIX	0	0.85±0.23	0.54±0.20	0.46±0.20	.77±0.04	0.42±0.20	0.58±0.20	0.67±0.05	0.76±0.13	0.24±0.13
	300	0.72±0.22	0.54±0.20	0.46±0.20	.78±0.04	0.71±0.15	0.29±0.15	0.64±0.04	0.75±0.12	0.25±0.12
	400	0.78±0.23	0.55±0.20	0.45±0.20	.63±0.02	0.83±0.10	0.17±0.10	0.61±0.07	0.85±0.10	0.15±0.10
PCM	0	0.92±0.05	--	--	1.03±0.03	--	--	1.00±0.03	--	--
	300	0.87±0.08	--	--	1.01±0.02	--	--	1.01±0.02	--	--
	400	0.81±.012	--	--	1.01±0.03	--	--	1.01±0.03	--	--

Estimated fuel utilization (pyruvate versus fatty acid) fractions are reported in **Table 4.3** and plotted in **Figure 4.6** at nominally zero [Ca^{2+}], approximately 40% of acetyl-CoA is supplied to the TCA cycle from pyruvate oxidation, with the rest supplied via β-oxidation for the low ATP demand conditions. A significant difference (p = 0.033) in increased fractional pyruvate utilization

is observed as calcium concentration increases under the low ATP demand rate condition (Fig. **Figure 4.6B**).

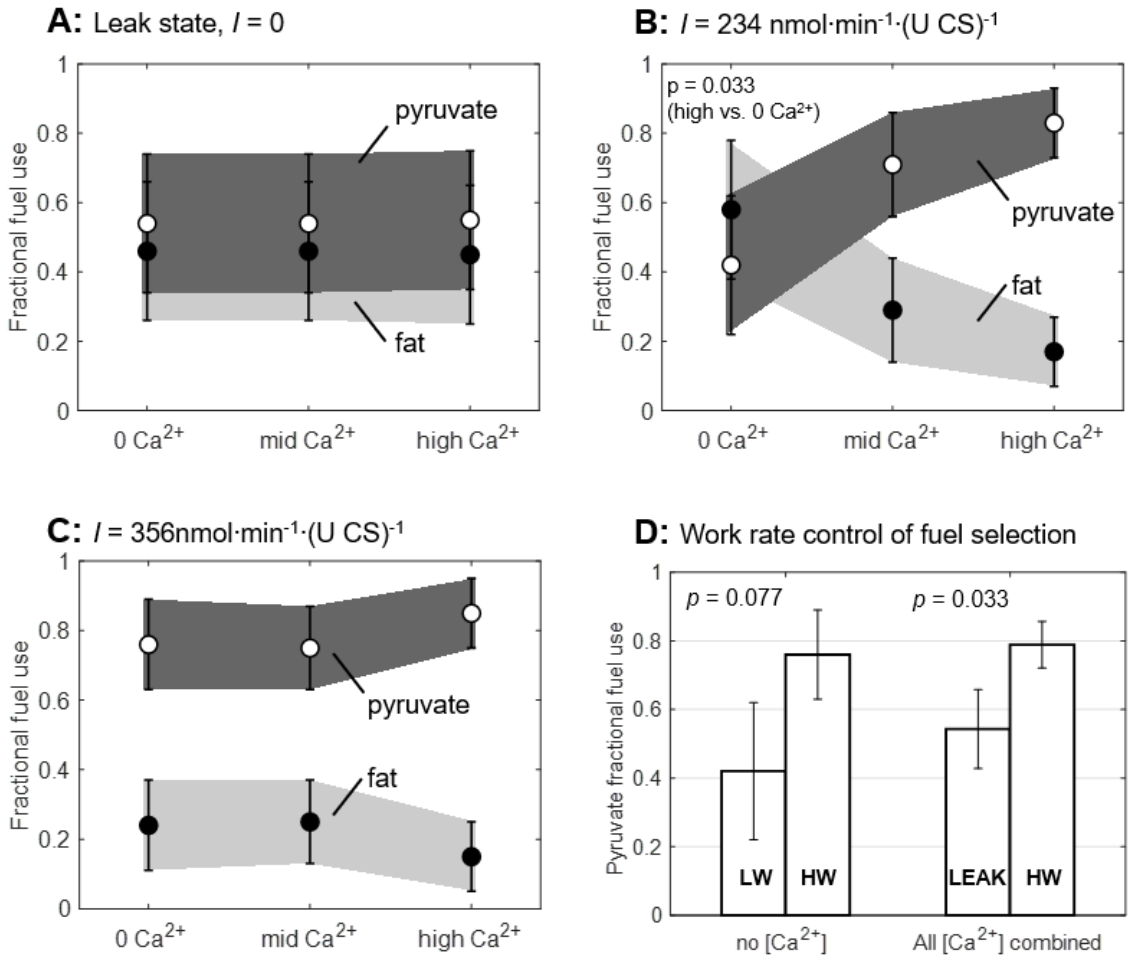

Figure 4.6 Mitochondrial fuel selection. Fractional oxidation of pyruvate versus palmitoyl-carnitine is plotted as a function of total [Ca^{2+}] under (A) Leak state (I = 0 nmol min^{-1} $(UCS)^{-1}$)), (B) low ATP demand (I = 234 nmol min^{-1} $(UCS)^{-1}$) condition and (C) high ATP demand (I = 356 nmol min^{-1} $(UCS)^{-1}$) condition. The observed trend of increasing fractional utilization of pyruvate with increasing [Ca^{2+}] is statistically significant, with estimated p = 0.033 in the low ATP demand state when comparing the highest calcium vs. no calcium present (B). D. Work rate control of mitochondrial fuel selection. Increasing fractional utilization of pyruvate dependent on work rate alone is below statistical significance, with estimated p = 0.077 when comparing low vs high ATP demand. Increased fractional utilization of pyruvate independent of calcium concentration is observed to be statistically significant, with estimated p = 0.033 when comparing the leak state vs high ATP demand conditions.

Under high demand conditions (**Figure 4.6C**) the fractional utilization of pyruvate is 76% at zero Ca^{2+}. Under this condition, addition of calcium causes a small but not significant increase in the fractional contribution from pyruvate to 85 ± 10%. These results indicate that nearly all of the acetyl-CoA is being produced by pyruvate dehydrogenase in steady-state conditions under high-demand and/or high [Ca^{2+}]. The ATP demand dependency is summarized in **Figure 4.6D**. With zero added Ca^{2+} the difference in fractional fuel utilization between the low (LW) and high (HW) demand conditions of 42% versus 76% is below statistical significance, with estimated p = 0.077. Since the uncertainty on the estimates for the leak states is relatively high, statistically significant comparison between leak state and other conditions are possible only by combining all of the calcium conditions together. With all calcium conditions combined, the fractional pyruvate utilization for the leak state is 54 ± 12% and 79 ± 7% for the HW OXPHOS state (p = 0.033). We conclude that both ATP demand and [Ca^{2+}] can independently influence the fractional fuel utilization.

4.5.4 Estimated Leak Current (J_L)

As mentioned in the methods section, the contributions of leak current (J_L) to the overall oxidative flux were estimated for the various experimental conditions probed based on the flux estimates reported in **Table 4.2**. Equation 4.37 estimates, J_L as the difference between the total rate of charge pumping via the respiratory chain and the rate of charge consumption for ATP synthesis. This expression is based on the following stoichiometric assumptions: (1.) each Complex I donor (NADH) generated is associated with 10 charges pumped across the inner membrane; (2.) each Complex II donor ($FADH_2$ and QH_2) generated is associated with 6 charged pumped; (3.) Each ATP generated is associated with a current of 11/3 charges. The 11/3

stoichiometric coefficient for ATP generation assumes an 8/3 stoichiometry for the ATPase(Nicholls *et al.*, 2013), and 1 charge transferred by the adenine nucleotide translocase.

Values of J_L estimated using these assumptions are plotted for the three different substrate conditions in **Figure 4.3**, **Figure 4.4** and **Figure 4.5**. This current is expected to be primarily composed of H^+ ions, with secondary contributions associated with calcium cycling and other ionic currents. In the leak state (I = 0), the estimated leak currents are approximately 400 nmol min^{-1} (U CS)$^{-1}$. Since slightly fewer than 20 charges are pumped by the respiratory complexes per O_2 molecule consumed, the leak current in the leak state may be alternatively estimated as slightly less than 20 times J_{O2} under pyruvate substrate conditions. Indeed, 20 times the average leak state J_{O2} (from Table 1) is 391 nmol min^{-1} (U CS)$^{-1}$. As demand is increased (I = 234 and 356 nmol min^{-1} (U CS)$^{-1}$), the estimated leak current decreases, presumably due to a decrease in magnitude of the mitochondrial membrane potential. Under OXPHOS conditions J_L is estimated to be approximately 200-300 nmol min^{-1} (U CS)$^{-1}$ for all substrate conditions. Since the ATP-producing current is 11/3 times I, the ratios of ATP-producing current to leak current are approximately 3:1 at I = 1/3 of V_{max}, and 7:1 at I = 1/2 of V_{max}.

4.6 Discussion

This study was designed to determine if and how fuel selection *in vitro* in cardiac mitochondria is affected by ATP demand and Ca^{2+} concentration, and to test the specific hypothesis that increases in mitochondrial Ca^{2+} can cause a shift to using relatively more carbohydrate and relatively less fatty acid substrate to fuel oxidative ATP synthesis in cardiac mitochondria.

Our results demonstrate that increasing calcium concentration does affect a switch in fuel utilization under mixed substrate conditions from primarily fatty acid at nominally zero calcium to primarily pyruvate with nonzero added calcium. Furthermore, our results demonstrate that this calcium-dependent fuel selection switch is also dependent on ATP demand. At the highest added calcium employed, the relative contribution of pyruvate to oxidative metabolism in mixed substrate conditions increases from 55 ± 20% at the leak state (ADP infusion rate of I = 0 nmol min^{-1} $(U\ CS)^{-1}$) to 83 ± 10% at an ADP infusion rate of I = 234 nmol min^{-1} $(U\ CS)^{-1}$ (approximately 1/3 V_{max}) to 85 ± 10% at I = 356 nmol min^{-1} $(U\ CS)^{-1}$ (approximately 1/2 V_{max}). These findings may be compared to the trend of increasing fraction of pyruvate utilization with increasing demand observed by Kuzmiak-Glancy and Willis (Kuzmiak-Glancy & Willis, 2014) in skeletal muscle mitochondrial from rat and sparrow.

The trend of increasing relative contribution of pyruvate with increasing Ca^{2+} is apparent at the moderate ATP demand level. But as the ATP demand level increases from moderate to high, fuel selection switches towards pyruvate utilization regardless of the calcium concentration. Thus, the effects of Ca^{2+} and increasing ATP demand on substrate switching appear to be additive. Furthermore, our data suggest that, at least under the *in vitro* conditions probed in this study, the primary regulator of Ca^{2+}-dependent fuel selection is pyruvate dehydrogenase. Fluxes through downstream dehydrogenases do not show clear dependencies on Ca^{2+} concentration under any of the substrates employed here.

Based on these observations we speculate that a physiological nonzero calcium concentration is necessary for cardiac mitochondria to effectively switch from a low-capacity fuel (fats) to a high-capacity fuel (carbohydrates) in response to acute increases in workload. This mechanism may help explain observations that deletion of the cardiac mitochondrial calcium

uniporter is associated with an impaired ability of the heart to acutely match ATP production to demand(Kwong *et al.*, 2015; Luongo *et al.*, 2015).

The AKG/malate exchange has been reported to be sensitive to calcium levels in brain as well as muscle and heart mitochondria from rats(Eigentler & et al., 2015). But in our results, regardless of the absence or presence of calcium, the AKG and malate exchange rate remained consistent regardless of the substrate and work rate conditions used across our experimental design with constant α-ketogluterate efflux from 80%-100%. These results were unexpected as we hypothesized that if calcium enhances the substrate affinity of α-ketogluterate dehydrogenase (Williamson & Corkey, 1979), α-ketogluterate dehydrogenase flux would be increased as calcium concentration increased. The findings that fluxes through downstream dehydrogenases do not show strong dependencies on Ca^{2+} concentration supports a model in which the primary regulator of Ca^{2+}-dependent fuel selection is pyruvate dehydrogenase.

In summary, our results show that a fuel selection switch from fatty acids to greater fractional utilization of pyruvate occurs with increasing ATP demand rate and calcium in cardiac mitochondria *in vitro*. These results mirror a previous observation obtained using isolated skeletal muscle mitochondria(Kuzmiak-Glancy & Willis, 2014). Finally, these observations are consistent with our hypothesis that calcium contributes to modulating the switch from fatty acid to carbohydrate oxidation with increasing ATP demand *in vivo*. This interpretation is consistent with the observations that mitochondrial calcium import is important in maintaining ATP production in acute stress responses(Kwong *et al.*, 2015; Luongo *et al.*, 2015). Namely, the steady-state results indicate that changes in work rate alone are enough to affect a switch to carbohydrate use. *In vivo*, the rate at which this switch happens may depend on mitochondrial calcium.

4.7 Conclusions

1. An open-loop control hypothesis stating that ATP supply is matched to ATP demand via mitochondrial Ca^{2+} acting as a mediator is broadly invoked.
2. Despite its ability to affect mitochondrial TCA cycle dehydrogenases, [Ca^{2+}] does not substantially alter mitochondrial ATP synthesis *in vitro* under physiological substrate conditions.
3. To determine if [Ca^{2+}] affects the relative use of carbohydrates versus fatty acids *in vitro*, we measured oxygen consumption and TCA cycle intermediate concentrations in suspensions of purified rat ventricular mitochondria with carbohydrate, fatty acid, and mixed substrates at various [Ca^{2+}] and ATP demand rates.
4. Our results suggest that changes in work rate alone are enough to affect a switch to carbohydrate use *in vitro*, whereas *in vivo* the rate at which this switch happens may depend on mitochondrial calcium.

Chapter 5 Concluding Remarks

5.1 Conclusions

As stated in this dissertation, HFpEF is increasing in prevalence and is associated with poor clinical outcomes and quality of life. Although many therapies exist for the homogenous HFrEF, it is more difficult to treat HFpEF. This may be because unlike HFrEF, HFpEF is represented by heterogeneous patient phenotypes. Classical, the HFrEF and HFpEF classifications are based on EF, a metric of the LV systolic capability. While EF seems to be a good enough marker to identify HFrEF patients whose pathology is mostly driven by cardiac dysfunction during systole (Murphy *et al.*, 2020), placing all patients with HFpEF in a single category of patients might be over simplistic approach. Advancement in our understanding of HFpEF demonstrates that disease progression is driven by more than cardiac dysfunction. Clearly, metabolic, systemic, and pulmonary circulation comorbidities play a big role in disease development and progression in HFpEF patients (Zile *et al.*, 2004; Tartière-Kesri *et al.*, 2012; Little & Zile, 2012; Lindman *et al.*, 2014; Kitzman & Lam, 2017).

Standard clinical measurements such as quantifying hemodynamics through RHC and obtaining cardiac volume assessment though TTE does not sufficiently discriminate HFpEF phenotypes to inform patient management. Part of this problem is that these measurements are taken at rest when many HFpEF are asymptomatic (Borlaug *et al.*, 2022). It has been suggested that exercise intolerance, impairment of recruitable oxygen reserve and cardiac power, which

consider peripheral factors contributing to the development of HF, may be of considerable importance in describing the clinical phenotype of HF patients (Beard *et al.*, 2021). A recent NHLBI working group emphasized this unmet need for robust phenotyping in HFpEF and its potential to improve care and outcomes for this population. The group specifically recommended systems biology-based computer modeling approaches that can incorporate the modeling of exercise responses in a patient group that has difficulty exercising (Shah et al., 2020). The computational modeling and ML tools that are developed in this dissertation may help in classifying HFpEF patients with respect to underlying dysfunction of the entire cardiovascular system, rather than merely relying on EF, will result in a more individually targeted treatment strategy for this patient population. Using model-based analysis and physiology-informed ML we demonstrate an approach to take standard RHC and TTE data from HFrEF and HFpEF patients obtained during resting conditions and derive important patient specific cardiovascular functional parameters. We then used a ML workflow to identify distinct HFpEF phenotypes and classifies patients with HFpEF into three distinct groups: systolic dysfunction (SD), mixed dysfunction (MD) and diastolic dysfunction (DD). SD HFpEF is a 'HFrEF-like' HFpEF group, DD HFpEF represents the 'classical' HFpEF patients, and MD HFpEF is a group that exhibits characteristics of both types of dysfunctions. This approach is unique and innovative compared to the standard ML approaches that use clinical data alone because it utilizes additional cardiovascular parameters derived from the model that are not available as direct clinical measures. After distinguishing these subgroups, our data reveals potential biomarkers readily available from routine clinical data for identifying SD HFpEF patients are elevated LV systolic and diastolic volumes. Interestingly, these biomarker differences necessary to determine HFpEF subgroups could not be distinguished based on the clinical data alone. Ultimately, the combination of mathematical modeling analysis and ML

techniques provides immense insight into the classifications of subpopulations of HF. We have found using patient specific clinical data to feed the computational model allows us to derive explicit physiological data that enhances the HFpEF phenotyping methodology in terms of accuracy, performance, and validity. Our hope is that future work and application of our model-based analysis and physiology-informed ML tool for precision phenotyping in HF would result in a more individually targeted treatment strategy for HFpEF patients.

5.2 Future Work

5.2.1 University of Michigan and Peking University Third Hospital Collaboration

For follow-up work we will increase our HF data set pool and have proposed studies in collaboration with the University of Michigan and Peking University Third Hospital. Through this collaboration, the lab will refine and train this novel approach using a retrospective HF dataset drawn from the two institutions. We will then conduct a prospective study obtaining the same measures used previously at baseline to validate our approach and expand upon it by gathering non-routine clinical measures during exercise. With this prospective dataset we will construct parallel model-based analysis and physiology-informed methods to compare the baseline and exercise analyses. Finally, additional plasma protein profiles and metabolomic measures will be obtained to see if biomarkers for each HFpEF subgroup can be identified. We will determine if and how the functional subgroups identified in these preliminary studies are sufficient to represent the broader patient population and are predictive of clinical outcomes, thus providing a powerful new diagnostic tool to inform future HFpEF clinical trial design.

5.2.2 Follow up Work With the IASD and TMZ Clinical Trials

Surprisingly our preliminary work retrospectively analyzing HFpEF patients selected for two clinical trials showed a bias in HFpEF patient selection that was characterized by systolic dysfunction more than diastolic dysfunction. These are interesting findings but more follow up work is needed. Our model captures the mechanical characteristics of the cardiovascular system during rest and currently is not adapted to capture the hemodynamic response during exercise. At least for HFpEF patients, many symptoms only manifest during exercise. Thus, modifying our model to simulate exercise and derive cardiovascular parameters, and then conducting unsupervised ML, would be of interest to test whether HFpEF patient subgroups are affected differently by exercise. Whether exercise derived parameters also lead to classification of additional subgroups of HFpEF or changes in classification would also be of interest.

Because we examined only small subset of patients for an IASD clinical trial, we had a very limited amount of clinical data available to parameterize our simulations in a patient specific manner. For future work, we will plan to share our preliminary work with the clinicians overseeing the IASD clinical trials and propose a collaboration to explore the effect of the shunt on hemodynamic parameters at rest and during exercise in the expanded data set of their clinical trials.

For the TMZ study, our preliminary work showed that HFpEF patients selected for this study were classed mostly systolic dysfunction (SD) or mixed dysfunction (MD) at rest. We do have MRI and RHC data available both at rest and during different exercise stress tests for patients in the placebo and pos-TMZ treatment state. We hope to either adapt our current model to capture exercise hemodynamics or use a more thorough model to capture patients' mechanics and bioenergetics in response to drug treatment. These patient data could also be very important

validation data for our computational modelling where we try to simulate exercise from resting patient data.

5.2.3 Calcium Role in Mitochondrial Fuel Selection

During HF, the heart undergoes changes in fuel selection, through induction of a neonatal gene program leading to the preferential use of carbohydrates over fatty acids like the developing heart (Taegtmeyer *et al.*, 2010). Because the failing heart is thought to be in a metabolically compromised state, understanding the mechanisms behind cardiac fuel selection is of importance in understanding cardiovascular disease as well as possible treatment mechanisms. There is some evidence that besides modulating contractility, calcium may play a role in modulating cardiac fuel selection. Yet, even during a healthy state our understanding of how cardiac mitochondrial fuel selection is modulated is very limited. In Chapter 4, we showed evidence that the relationship between increasing relative contribution of carbohydrates (pyruvate) with increasing cytoplasmic Ca^{2+} is apparent at a moderate ATP demand level. However, as the ATP demand level increases from moderate to high, fuel selection switches towards pyruvate utilization regardless of the cytoplasmic calcium concentration. Thus, the effects of Ca^{2+} and increasing ATP demand on substrate switching appear to be additive. Furthermore, our data suggest that, at least under the *in vitro* conditions probed in this study, the primary regulator of Ca^{2+}-dependent fuel selection is pyruvate dehydrogenase. Fluxes through downstream dehydrogenases do not show clear dependencies on Ca^{2+} concentration under any of the substrates employed here. One important piece of missing data raised by reviewers of our manuscript, is to determine whether the different bath Ca^{2+} concentrations tested were indeed sufficient to alter matrix calcium content via uptake through MCU or other pathways. We also will need to measure mitochondrial membrane potential

to explain changes in leak current at different work rates and verify the altered mitochondrial Ca^{2+} effect is acting through pyruvate dehydrogenase. Future work will address these concerns and hopes to elucidate the role of calcium in regulation of fuel selection of the healthy heart, as well as its role in the pathophysiology of the failing heart.

Bibliography

Anon (1999*a*). The Cardiac Insufficiency Bisoprolol Study II (CIBIS-II): a randomised trial. *Lancet* **353,** 9–13.

Anon (1999*b*). Effect of metoprolol CR/XL in chronic heart failure: Metoprolol CR/XL Randomised Intervention Trial in Congestive Heart Failure (MERIT-HF). *Lancet* **353,** 2001–2007.

Bache R, Zhang J, Murakami Y, Zhang Y, Cho YK, Merkle H, Gong G, From AH & Ugurbil K (1999). Myocardial oxygenation at high workstates in hearts with left ventricular hypertrophy. *Cardiovasc Res* **42,** 616–626.

Bakermans AJ, Bazil JN, Nederveen AJ, Strijkers GJ, Boekholdt SM, Beard DA & Jeneson JAL (2017). Human Cardiac 31P-MR Spectroscopy at 3 Tesla Cannot Detect Failing Myocardial Energy Homeostasis during Exercise. *Front Physiol*; DOI: 10.3389/fphys.2017.00939.

Balaban RS (2002). Cardiac Energy Metabolism Homeostasis: Role of Cytosolic Calcium. *J Mol Cell Cardiol* **34,** 1259–1271.

Barreras A & Gurk-Turner C (2003). Angiotensin II receptor blockers. *Proc (Bayl Univ Med Cent)* **16,** 123–126.

Beard DA (2011). Simulation of cellular biochemical system kinetics. *WIREs Systems Biology and Medicine* **3,** 136–146.

Beard DA, Hummel SL & Jezek F (2021). Heart Failure as a Limitation of Cardiac Power Output. *Function*; DOI: 10.1093/function/zqab066.

Beard DA & Kushmerick MJ (2009). Strong Inference for Systems Biology. *PLoS Comput Biol* **5,** e1000459.

Beneken JEW & DeWit B (1967). A physical approach to hemodynamic aspects of the human cardiovascular system. In *Physical Bases of Circulatory Transport: Regulation and Exchange*, pp. 1–45.

Borlaug BA et al. (2022). Latent Pulmonary Vascular Disease May Alter the Response to Therapeutic Atrial Shunt Device in Heart Failure. *Circulation* **145,** 1592–1604.

Borlaug BA, Chen H, Lin G, Redfield MM, Lewis GD, Semigran MJ, McNulty SE, LeWinter M, Deswal A & Margulies KB (2015). Response to Letter Regarding Article, "Effects of Sildenafil on Ventricular and Vascular Function in Heart Failure With Preserved Ejection Fraction." *Circ Heart Fail* **8,** 840-undefined.

Borlaug BA, Melenovsky V, Russell SD, Kessler K, Pacak K, Becker LC & Kass DA (2006). Impaired Chronotropic and Vasodilator Reserves Limit Exercise Capacity in Patients With Heart Failure and a Preserved Ejection Fraction. *Circulation* **114,** 2138–2147.

Borlaug BA, Olson TP, Lam CSP, Flood KS, Lerman A, Johnson BD & Redfield MM (2010). Global Cardiovascular Reserve Dysfunction in Heart Failure With Preserved Ejection Fraction. *J Am Coll Cardiol* **56,** 845–854.

van de Bovenkamp AA, Bakermans AJ, Allaart CP, Nederveen AJ, Kok WEM, van Rossum AC & Handoko ML (2020). TrimetaziDine as a Performance-enhancING drug in heart failure with preserved ejection fraction (DoPING-HFpEF): rationale and design of a placebo-controlled cross-over intervention study. *Netherlands Heart Journal* **28,** 312–319.

Bright RA, Lima F v., Avila C, Butler J & Stergiopoulos K (2021). Maternal Heart Failure. *J Am Heart Assoc*; DOI: 10.1161/JAHA.121.021019.

Campia U, Nodari S & Gheorghiade M (2010). Acute Heart Failure With Low Cardiac Output: Can We Develop a Short-term Inotropic Agent That Does Not Increase Adverse Events? *Curr Heart Fail Rep* **7,** 100–109.

Carlson BC & Jones E (n.d.). HFpEF Phenotyping Simulation Code (Version 1.1).

Chait A, Cohen HE, Meltzer LE & VanDurme J-P (1972). The Bedside Chest Radiograph in the Evaluation of Incipient Heart Failure. *Radiology* **105,** 563–566.

Chamsi-Pasha MA, Zhan Y, Debs D & Shah DJ (2020). CMR in the Evaluation of Diastolic Dysfunction and Phenotyping of HFpEF. *JACC Cardiovasc Imaging* **13,** 283–296.

Chance B, Leigh JS, Clark BJ, Maris J, Kent J, Nioka S & Smith D (1985). Control of oxidative metabolism and oxygen delivery in human skeletal muscle: a steady-state analysis of the work/energy cost transfer function. *Proceedings of the National Academy of Sciences* **82,** 8384–8388.

Chance B, Leigh JS, Kent J, McCully K, Nioka S, Clark BJ, Maris JM & Graham T (1986). Multiple controls of oxidative metabolism in living tissues as studied by phosphorus magnetic resonance. *Proceedings of the National Academy of Sciences* **83,** 9458–9462.

Chance B & Williams GR (2006). The Respiratory Chain and Oxidative Phosphorylation. In, pp. 65–134.

Chemla D, Lau EMT, Papelier Y, Attal P & Hervé P (2015). Pulmonary vascular resistance and compliance relationship in pulmonary hypertension. *European Respiratory Journal* **46,** 1178–1189.

Cohen JB, Schrauben SJ, Zhao L, Basso MD, Cvijic ME, Li Z, Yarde M, Wang Z, Bhattacharya PT, Chirinos DA, Prenner S, Zamani P, Seiffert DA, Car BD, Gordon DA, Margulies K, Cappola T & Chirinos JA (2020). Clinical Phenogroups in Heart Failure With Preserved Ejection Fraction. *JACC Heart Fail* **8,** 172–184.

Colunga AL, Kim KG, Woodall NP, Dardas TF, Gennari JH, Olufsen MS & Carlson BE (2020). Deep phenotyping of cardiac function in heart transplant patients using cardiovascular system models. *J Physiol* **598,** 3203–3222.

Corral-Acero J et al. (2020). The "Digital Twin" to enable the vision of precision cardiology. *Eur Heart J* **41,** 4556-4564B.

Cristianini N & Ricci E (2008). Support Vector Machines. In *Encyclopedia of Algorithms*, pp. 928–932. Springer US, Boston, MA.

Denton RM (2009). Regulation of mitochondrial dehydrogenases by calcium ions. *Biochimica et Biophysica Acta (BBA) - Bioenergetics* **1787,** 1309–1316.

Dunlay SM, Roger VL & Redfield MM (2017). Epidemiology of heart failure with preserved ejection fraction. *Nat Rev Cardiol* **14,** 591–602.

Dwivedi AK, Mallawaarachchi I & Alvarado LA (2017). Analysis of small sample size studies using nonparametric bootstrap test with pooled resampling method. *Stat Med*; DOI: 10.1002/sim.7263.

Edelmann F, Wachter R, Schmidt AG, Kraigher-Krainer E, Colantonio C, Kamke W, Duvinage A, Stahrenberg R, Durstewitz K, Löffler M, Düngen H-D, Tschöpe C, Herrmann-Lingen C, Halle M, Hasenfuss G, Gelbrich G, Pieske B & Aldo-DHF Investigators for the (2013). Effect of Spironolactone on Diastolic Function and Exercise Capacity in Patients With Heart Failure With Preserved Ejection Fraction. *JAMA* **309,** 781–791.

Eigentler A & et al. (2015). Laboratory protocol: citrate synthase a mitochondrial marker enzyme. In *Mitochondrial Physiology Network*, pp. 1–11.

Eisen MB, Spellman PT, Brown PO & Botstein D (1998). Cluster analysis and display of genome-wide expression patterns. *PNAS* **95,** 14863–14868.

Fallick C, Sobotka PA & Dunlap ME (2011). Sympathetically Mediated Changes in Capacitance. *Circ Heart Fail*; DOI: 10.1161/CIRCHEARTFAILURE.111.961789.

Feldman T, Mauri L, Kahwash R, Litwin S, Ricciardi MJ, van der Harst P, Penicka M, Fail PS, Kaye DM, Petrie MC, Basuray A, Hummel SL, Forde-McLean R, Nielsen CD, Lilly S, Massaro JM, Burkhoff D & Shah SJ (2018). Transcatheter Interatrial Shunt Device for the Treatment of Heart Failure With Preserved Ejection Fraction (REDUCE LAP-HF I [Reduce Elevated Left Atrial Pressure in Patients With Heart Failure]). *Circulation* **137,** 364–375.

Fincke R, Hochman JS, Lowe AM, Menon V, Slater JN, Webb JG, LeJemtel TH & Cotter G (2004). Cardiac power is the strongest hemodynamic correlate of mortality in cardiogenic shock: A report from the SHOCK trial registry. *J Am Coll Cardiol* **44,** 340–348.

Franssen C, Chen S, Unger A, Korkmaz HI, de Keulenaer GW, Tschöpe C, Leite-Moreira AF, Musters R, Niessen HWM, Linke WA, Paulus WJ & Hamdani N (2016). Myocardial Microvascular Inflammatory Endothelial Activation in Heart Failure With Preserved Ejection Fraction. *JACC Heart Fail* **4,** 312–324.

Fudim M, Hernandez AF & Felker GM (2017). Role of Volume Redistribution in the Congestion of Heart Failure. *Am Heart J* **6,** 1–10.

Gertz EW, Wisneski JA, Stanley WC & Neese RA (1988). Myocardial substrate utilization during exercise in humans. Dual carbon-labeled carbohydrate isotope experiments. *Journal of Clinical Investigation* **82,** 2017–2025.

Gong G, Liu J, Liang P, Guo T, Hu Q, Ochiai K, Hou M, Ye Y, Wu X, Mansoor A, From AHL, Ugurbil K, Bache RJ & Zhang J (2003). Oxidative capacity in failing hearts. *American Journal of Physiology-Heart and Circulatory Physiology* **285,** H541–H548.

Gong G, Uğurbil K & Zhang J (1999). Transmural metabolic heterogeneity at high cardiac work states. *American Journal of Physiology-Heart and Circulatory Physiology* **277,** H236–H242.

Griffiths EJ & Rutter GA (2009). Mitochondrial calcium as a key regulator of mitochondrial ATP production in mammalian cells. *Biochimica et Biophysica Acta (BBA) - Bioenergetics* **1787,** 1324–1333.

Guazzi M (2014). Pulmonary Hypertension in Heart Failure Preserved Ejection Fraction. *Circ Heart Fail* **7,** 367–377.

Guazzi M, Vicenzi M, Arena R & Guazzi MD (2011). Pulmonary Hypertension in Heart Failure With Preserved Ejection Fraction. *Circulation* **124,** 164–174.

Hahn VS, Knutsdottir H, Luo X, Bedi K, Margulies KB, Haldar SM, Stolina M, Yin J, Khakoo AY, Vaishnav J, Bader JS, Kass DA & Sharma K (2021). Myocardial Gene Expression Signatures in Human Heart Failure With Preserved Ejection Fraction. *Circulation* **143,** 120–134.

Heidenreich PA et al. (2022). 2022 AHA/ACC/HFSA Guideline for the Management of Heart Failure: A Report of the American College of Cardiology/American Heart Association Joint Committee on Clinical Practice Guidelines. *Circulation*; DOI: 10.1161/CIR.0000000000001063.

Hoendermis ES, Liu LCY, Hummel YM, van der Meer P, de Boer RA, Berger RMF, van Veldhuisen DJ & Voors AA (2015). Effects of sildenafil on invasive haemodynamics and exercise capacity in heart failure patients with preserved ejection fraction and pulmonary hypertension: a randomized controlled trial. *Eur Heart J* **36,** 2565–2573.

Hummel SL, DeFranco AC, Skorcz S, Montoye CK & Koelling TM (2009). Recommendation of Low-Salt Diet and Short-term Outcomes in Heart Failure with Preserved Systolic Function. *Am J Med* **122,** 1029–1036.

Jeneson JAL, Westerhoff H v. & Kushmerick MJ (2000). A metabolic control analysis of kinetic controls in ATP free energy metabolism in contracting skeletal muscle. *American Journal of Physiology-Cell Physiology* **279,** C813–C832.

Jeneson JeroenAL, Wiseman RW, Westerhoff H v. & Kushmerick MJ (1996). The Signal Transduction Function for Oxidative Phosphorylation Is at Least Second Order in ADP. *Journal of Biological Chemistry* **271,** 27995–27998.

Jezek F, Randall EB, Carlson BE & Beard DA (2022). Systems analysis of the mechanisms governing the cardiovascular response to changes in posture and in peripheral demand during exercise. *J Mol Cell Cardiol* **163,** 33–55.

Jolliffe IT (1986). *Principal Component Analysis*, 2nd Edition. Springer-Verlag, New York.

Jones E, Randall EB, Hummel SL, Cameron DM, Beard DA & Carlson BE (2021). Phenotyping heart failure using model-based analysis and physiology-informed machine learning. *J Physiol* **599,** 4991–5013.

Kao DP, Lewsey JD, Anand IS, Massie BM, Zile MR, Carson PE, McKelvie RS, Komajda M, McMurray JJ & Lindenfeld J (2015). Characterization of subgroups of heart failure patients with preserved ejection fraction with possible implications for prognosis and treatment response. *Eur J Heart Fail* **17,** 925–935.

Kemp GJ, Meyerspeer M & Moser E (2007). Absolute quantification of phosphorus metabolite concentrations in human musclein vivo by31P MRS: a quantitative review. *NMR Biomed* **20,** 555–565.

Kitzman DW & Lam CSP (2017). Obese Heart Failure With Preserved Ejection Fraction Phenotype. *Circulation* **136,** 20–23.

Kraskov A, Stögbauer H, Andrzejak RG & Grassberger P (2005). Hierarchical clustering using mutual information. *EPL*; DOI: 10.1209/epl/i2004-10483-y.

Kushmerick MJ, Meyer RA & Brown TR (1992). Regulation of oxygen consumption in fast- and slow-twitch muscle. *American Journal of Physiology-Cell Physiology* **263,** C598–C606.

Kuzmiak-Glancy S & Willis WT (2014). Skeletal Muscle Fuel Selection Occurs at the Mitochondrial Level. *Journal of Experimental Biology*; DOI: 10.1242/jeb.098863.

Kwong JQ, Huo J, Bround MJ, Boyer JG, Schwanekamp JA, Ghazal N, Maxwell JT, Jang YC, Khuchua Z, Shi K, Bers DM, Davis J & Molkentin JD (2018). The mitochondrial calcium uniporter underlies metabolic fuel preference in skeletal muscle. *JCI Insight*; DOI: 10.1172/jci.insight.121689.

Kwong JQ, Lu X, Correll RN, Schwanekamp JA, Vagnozzi RJ, Sargent MA, York AJ, Zhang J, Bers DM & Molkentin JD (2015). The Mitochondrial Calcium Uniporter Selectively Matches Metabolic Output to Acute Contractile Stress in the Heart. *Cell Rep* **12,** 15–22.

Landaw EM & DiStefano JJ (1984). Multiexponential, multicompartmental, and noncompartmental modeling. II. Data analysis and statistical considerations. *American Journal of Physiology-Regulatory, Integrative and Comparative Physiology* **246,** R665–R677.

Lang RM, Badano LP, Mor-Avi V, Afilalo J, Armstrong A, Ernande L, Flachskampf FA, Foster E, Goldstein SA, Kuznetsova T, Lancellotti P, Muraru D, Picard MH, Rietzschel ER, Rudski L, Spencer KT, Tsang W & Voigt JU (2016). Recommendations for Cardiac Chamber Quantification by Echocardiography in Adults: An Update from the American Society of Echocardiography and the European Association of, Cardiovascular Imaging. *Eur Heart J Cardiovasc Imaging* **17,** 1-39.e14.

LaNoue K, Nicklas WJ & Williamson JR (1970). Control of citric acid cycle activity in rat heart mitochondria. *J Biol Chem* **245,** 102–111.

Lassers BW, Kaijser L, Wahlqvist ML & Carlson LA (1971). RELATIONSHIP IN MAN BETWEEN PLASMA FREE FATTY ACIDS AND MYOCARDIAL METABOLISM OF CARBOHYDRATE SUBSTRATES. *The Lancet* **298,** 448–450.

Lee JF, Barrett-O'Keefe Z, Garten RS, Nelson AD, Ryan JJ, Nativi JN, Richardson RS & Wray DW (2016). Evidence of microvascular dysfunction in heart failure with preserved ejection fraction. *Heart* **102,** 278–284.

Levrero-Florencio F, Margara F, Zacur E, Bueno-Orovio A, Wang ZJ, Santiago A, Aguado-Sierra J, Houzeaux G, Grau V, Kay D, Vázquez M, Ruiz-Baier R & Rodriguez B (2020). Sensitivity analysis of a strongly-coupled human-based electromechanical cardiac model: Effect of mechanical parameters on physiologically relevant biomarkers. *Comput Methods Appl Mech Eng* **361,** 112762.

Lilly LS (2016). *Pathophysiology of heart disease: a collaborative project of medical students and faculty*, 6th edn. Wolters Kluwer, Philadelphia, PA, USA.

Lindman BR, Dávila-Román VG, Mann DL, McNulty S, Semigran MJ, Lewis GD, de las Fuentes L, Joseph SM, Vader J, Hernandez AF & Redfield MM (2014). Cardiovascular Phenotype in HFpEF Patients With or Without Diabetes. *J Am Coll Cardiol* **64,** 541–549.

Little WC & Zile MR (2012). HFpEF: Cardiovascular Abnormalities Not Just Comorbidities. *Circ Heart Fail* **5,** 669–671.

Liu LCY, Hummel YM, van der Meer P, Berger RMF, Damman K, van Veldhuisen DJ, Voors AA & Hoendermis ES (2017). Effects of sildenafil on cardiac structure and function, cardiopulmonary exercise testing and health-related quality of life measures in heart failure patients with preserved ejection fraction and pulmonary hypertension. *Eur J Heart Fail* **19,** 116–125.

Lopez R, Marzban B, Gao X, Lauinger E, van den Bergh F, Whitesall SE, Converso-Baran K, Burant CF, Michele DE & Beard DA (2020). Impaired Myocardial Energetics Causes

Mechanical Dysfunction in Decompensated Failing Hearts. *Function*; DOI: 10.1093/function/zqaa018.

Luongo TS, Lambert JP, Yuan A, Zhang X, Gross P, Song J, Shanmughapriya S, Gao E, Jain M, Houser SR, Koch WJ, Cheung JY, Madesh M & Elrod JW (2015). The Mitochondrial Calcium Uniporter Matches Energetic Supply with Cardiac Workload during Stress and Modulates Permeability Transition. *Cell Rep* **12,** 23–34.

Maréchaux S, Samson R, van Belle E, Breyne J, de Monte J, Dédrie C, Chebai N, Menet A, Banfi C, Bouabdallaoui N, le Jemtel TH & Ennezat P-V (2016). Vascular and Microvascular Endothelial Function in Heart Failure With Preserved Ejection Fraction. *J Card Fail* **22,** 3–11.

Marian AJ & Braunwald E (2017). Hypertrophic Cardiomyopathy. *Circ Res* **121,** 749–770.

Marinho-Carvalho MM, Costa-Mattos PV, Spitz GA, Zancan P & Sola-Penna M (2009). Calmodulin upregulates skeletal muscle 6-phosphofructo-1-kinase reversing the inhibitory effects of allosteric modulators. *Biochimica et Biophysica Acta (BBA) - Proteins and Proteomics* **1794,** 1175–1180.

Marinho-Carvalho MM, Zancan P & Sola-Penna M (2006). Modulation of 6-phosphofructo-1-kinase oligomeric equilibrium by calmodulin: Formation of active dimmers. *Mol Genet Metab* **87,** 253–261.

Murphy SP, Ibrahim NE & Januzzi JL (2020). Heart Failure With Reduced Ejection Fraction. *JAMA* **324,** 488.

Nadler SB, Hidalgo JU & Bloch T (1962). Prediction of blood volume in normal human adults. *Surgery* **51,** 224–232.

Narang N, Thibodeau JT, Levine BD, Gore MO, Ayers CR, Lange RA, Cigarroa JE, Turer AT, de Lemos JA & McGuire DK (2014). Inaccuracy of Estimated Resting Oxygen Uptake in the Clinical Setting. *Circulation* **129,** 203–210.

Nassif ME et al. (2021). The SGLT2 inhibitor dapagliflozin in heart failure with preserved ejection fraction: a multicenter randomized trial. *Nat Med* **27,** 1954–1960.

Nicholls DG, Ferguson SJ & ScienceDirect (2013). Bioenergetics.

Nylin G (1933). The relation between heart volume and cardiac output per beat as a measure of cardiac activity. *Sven Lakartidn*.

Obokata M, Reddy YNV, Shah SJ, Kaye DM, Gustafsson F, Hasenfuβ G, Hoendermis E, Litwin SE, Komtebedde J, Lam C, Burkhoff D & Borlaug BA (2019). Effects of Interatrial Shunt on Pulmonary Vascular Function in Heart Failure With Preserved Ejection Fraction. *J Am Coll Cardiol* **74,** 2539–2550.

Ochiai K, Zhang J, Gong G, Zhang Y, Liu J, Ye Y, Wu X, Liu H, Murakami Y, Bache RJ, Ugurbil K & From AHL (2001). Effects of augmented delivery of pyruvate on myocardial high-energy phosphate metabolism at high workstate. *American Journal of Physiology-Heart and Circulatory Physiology* **281,** H1823–H1832.

Opotowsky AR, Hess E, Maron BA, Brittain EL, Barón AE, Maddox TM, Alshawabkeh LI, Wertheim BM, Xu M, Assad TR, Rich JD, Choudhary G & Tedford RJ (2017). Thermodilution vs Estimated Fick Cardiac Output Measurement in Clinical Practice. *JAMA Cardiol*; DOI: 10.1001/jamacardio.2017.2945.

Orphanou N, Papatheodorou E & Anastasakis A (2022). Dilated cardiomyopathy in the era of precision medicine: latest concepts and developments. *Heart Fail Rev* **27,** 1173–1191.

Owan TE, Hodge DO, Herges RM, Jacobsen SJ, Roger VL & Redfield MM (2006). Trends in Prevalence and Outcome of Heart Failure with Preserved Ejection Fraction. *N Engl J Med* **355,** 251–259.

Packer M, Coats AJ, Fowler MB, Katus HA, Krum H, Mohacsi P, Rouleau JL, Tendera M, Castaigne A, Roecker EB, Schultz MK, DeMets DL & Carvedilol Prospective Randomized Cumulative Survival Study Group (2001). Effect of carvedilol on survival in severe chronic heart failure. *N Engl J Med* **344,** 1651–1658.

Palau P, Seller J, Domínguez E, Gómez I, Ramón JM, Sastre C, Espriella R, Santas E, Miñana G, Chorro FJ, González-Juanatey JR & Núñez J (2020). Beta-blockers withdrawal in patients with heart failure with preserved ejection fraction and chronotropic incompetence: Effect on functional capacity rationale and study design of a prospective, randomized, controlled trial (The Preserve-HR trial). *Clin Cardiol* **43,** 423–429.

Panov A v. & Scaduto RC (1996). Substrate specific effects of calcium on metabolism of rat heart mitochondria. *American Journal of Physiology-Heart and Circulatory Physiology* **270,** H1398–H1406.

Pepper GS & Lee RW (1999). Sympathetic Activation in Heart Failure and Its Treatment With β-Blockade. *Arch Intern Med* **159,** 225.

Pinilla-Vera M, Hahn VS & Kass DA (2019). Leveraging Signaling Pathways to Treat Heart Failure With Reduced Ejection Fraction. *Circ Res* **124,** 1618–1632.

Qi F, Pradhan RK, Dash RK & Beard DA (2011). Detailed kinetics and regulation of mammalian 2-oxoglutarate dehydrogenase. *BMC Biochem* **12,** 53.

Randall E. B., Randolph N. Z., Alexanderian A. & Olufsen M.S. (2021). Global sensitivity analysis informed model reduction and selection applied to a Valsalva maneuver model.

Redfield MM, Anstrom KJ, Levine JA, Koepp GA, Borlaug BA, Chen HH, LeWinter MM, Joseph SM, Shah SJ, Semigran MJ, Felker GM, Cole RT, Reeves GR, Tedford RJ, Tang WHW, McNulty SE, Velazquez EJ, Shah MR & Braunwald E (2015). Isosorbide Mononitrate in Heart Failure with Preserved Ejection Fraction. *N Engl J Med* **373,** 2314–2324.

Richard E. Klabunde (2015). Cardiovascular Physiology Concepts. *Richard E Klabunde, all rights reserved*.

Rumindo GK, Ohayon J, Croisille P & Clarysse P (2020). In vivo estimation of normal left ventricular stiffness and contractility based on routine cine MR acquisition. *Med Eng Phys* **85,** 16–26.

Russo V, Lovato L & Ligabue G (2020). Cardiac MRI: technical basis. *Radiol Med* **125,** 1040–1055.

Said Hajouli & Dipesh Ludhwani (2022). Heart Failure And Ejection Fraction. *StatPearls [Internet]*.

Senni M et al. (2014). New strategies for heart failure with preserved ejection fraction: the importance of targeted therapies for heart failure phenotypes. *Eur Heart J* **35,** 2797–2815.

Serenelli M, Jackson A, Dewan P, Jhund PS, Petrie MC, Rossignol P, Campo G, Pitt B, Zannad F, Ferreira JP & McMurray JJV (2020). Mineralocorticoid Receptor Antagonists, Blood Pressure, and Outcomes in Heart Failure With Reduced Ejection Fraction. *JACC Heart Fail* **8,** 188–198.

Shah AM, Claggett B, Sweitzer NK, Shah SJ, Anand IS, Liu L, Pitt B, Pfeffer MA & Solomon SD (2015). Prognostic Importance of Impaired Systolic Function in Heart Failure With Preserved Ejection Fraction and the Impact of Spironolactone. *Circulation* **132,** 402–414.

Shah SJ (2019). 20th Annual Feigenbaum Lecture: Echocardiography for Precision Medicine—Digital Biopsy to Deconstruct Biology. *J Am Soc Echocardiogr* **32,** 1379-1395.e2.

Shah SJ et al. (2022). Atrial shunt device for heart failure with preserved and mildly reduced ejection fraction (REDUCE LAP-HF II): a randomised, multicentre, blinded, sham-controlled trial. *The Lancet* **399,** 1130–1140.

Shah SJ, Borlaug BA, Kitzman DW, McCulloch AD, Blaxall BC, Agarwal R, Chirinos JA, Collins S, Deo RC, Gladwin MT, Granzier H, Hummel SL, Kass DA, Redfield MM, Sam F, Wang TJ, Desvigne-Nickens P & Adhikari BB (2020). Research Priorities for Heart Failure With Preserved Ejection Fraction. *Circulation* **141,** 1001–1026.

Shah SJ, Kitzman DW, Borlaug BA, van Heerebeek L, Zile MR, Kass DA & Paulus WJ (2016). Phenotype-Specific Treatment of Heart Failure With Preserved Ejection Fraction. *Circulation* **134,** 73–90.

Shao C, Wang J, Tian J & Tang Y (2020). Coronary Artery Disease: From Mechanism to Clinical Practice. In, pp. 1–36.

Sica DA (2005). Pharmacokinetics and Pharmacodynamics of Mineralocorticoid Blocking Agents and their Effects on Potassium Homeostasis. *Heart Fail Rev* **10,** 23–29.

Smith BW, Chase JG, Nokes RI, Shaw GM & Wake G (2004). Minimal haemodynamic system model including ventricular interaction and valve dynamics. *Med Eng Phys* **26,** 131–139.

Sobol′ IM (2001). Global sensitivity indices for nonlinear mathematical models and their Monte Carlo estimates. *MATH COMPUT SIMULAT*; DOI: 10.1016/S0378-4754(00)00270-6.

Solomon SD et al. (2019). Angiotensin–Neprilysin Inhibition in Heart Failure with Preserved Ejection Fraction. *N Engl J Med* **381,** 1609–1620.

Taegtmeyer H, Sen S & Vela D (2010). Return to the fetal gene program. *Ann N Y Acad Sci* **1188,** 191–198.

Taqueti VR, Solomon SD, Shah AM, Desai AS, Groarke JD, Osborne MT, Hainer J, Bibbo CF, Dorbala S, Blankstein R & di Carli MF (2018). Coronary microvascular dysfunction and future risk of heart failure with preserved ejection fraction. *Eur Heart J* **39,** 840–849.

Tartière-Kesri L, Tartière J-M, Logeart D, Beauvais F & Cohen Solal A (2012). Increased Proximal Arterial Stiffness and Cardiac Response With Moderate Exercise in Patients With Heart Failure and Preserved Ejection Fraction. *J Am Coll Cardiol* **59,** 455–461.

Teichholz LE, Kreulen T, Herman M v. & Gorlin R (1976). Problems in echocardiographic volume determinations: Echocardiographic-angiographic correlations in the presence or absence of asynergy. *Am J Cardiol* **37,** 7–11.

Vanderbilt University Medical Center (2020). Commodore Compendium RHC.

Vinnakota KC, Dash RK & Beard DA (2011). Stimulatory Effects of Calcium on Respiration and NAD(P)H Synthesis in Intact Rat Heart Mitochondria Utilizing Physiological

Substrates Cannot Explain Respiratory Control in Vivo. *Journal of Biological Chemistry* **286,** 30816–30822.

Vinnakota KC, Singhal A, Van den Bergh F, Bagher-Oskouei M, Wiseman RW & Beard DA (2016). Open-Loop Control of Oxidative Phosphorylation in Skeletal and Cardiac Muscle Mitochondria by Ca2+. *Biophys J* **110,** 954–961.

Wachtell K, Gerdts E, Palmieri V, Olsen MH, Nieminen MS, Papademetriou V, Boman K, Dahlöf B, Aurigemma GP, Rokkedal JE & Devereux RB (2010). In-treatment midwall and endocardial fractional shortening predict cardiovascular outcome in hypertensive patients with preserved baseline systolic ventricular function: the Losartan Intervention For Endpoint reduction study. *J Hypertens* **28,** 1541–1546.

Wan B, LaNoue KF, Cheung JY & Scaduto RC (1989). Regulation of citric acid cycle by calcium. *J Biol Chem* **264,** 13430–13439.

Wang ZJ, Santiago A, Zhou X, Wang L, Margara F, Levrero-Florencio F, Das A, Kelly C, Dall'Armellina E, Vazquez M & Rodriguez B (2021). Human biventricular electromechanical simulations on the progression of electrocardiographic and mechanical abnormalities in post-myocardial infarction. *Europace* **23,** i143–i152.

Wang ZJ, Wang VY, Bradley CP, Nash MP, Young AA & Cao JJ (2018). Left Ventricular Diastolic Myocardial Stiffness and End-Diastolic Myofibre Stress in Human Heart Failure Using Personalised Biomechanical Analysis. *J Cardiovasc Transl Res* **11,** 346–356.

Ward JH (1963). Hierarchical Grouping to Optimize an Objective Function. *J Am Stat Assoc*; DOI: 10.1080/01621459.1963.10500845.

Wilkin GA & Huang X (2008). A practical comparison of two K-Means clustering algorithms. *BMC Bioinformatics* **9,** S19-undefined.

Williams GSB, Boyman L & Lederer WJ (2015). Mitochondrial calcium and the regulation of metabolism in the heart. *J Mol Cell Cardiol* **78,** 35–45.

Williamson JR & Corkey BE (1979). Assay of citric acid cycle intermediates and related compounds—Update with tissue metabolite levels and Intracellular Distribution. In, pp. 200–222.

Wu F & Beard DA (2009). Roles of the creatine kinase system and myoglobin in maintaining energetic state in the working heart. *BMC Syst Biol* **3,** 22.

Wu F, Jeneson JAL & Beard DA (2007). Oxidative ATP synthesis in skeletal muscle is controlled by substrate feedback. *American Journal of Physiology-Cell Physiology* **292,** C115–C124.

Wu F, Zhang EY, Zhang J, Bache RJ & Beard DA (2008). Phosphate metabolite concentrations and ATP hydrolysis potential in normal and ischaemic hearts. *J Physiol* **586,** 4193–4208.

Wu F, Zhang J & Beard DA (2009). Experimentally observed phenomena on cardiac energetics in heart failure emerge from simulations of cardiac metabolism. *Proceedings of the National Academy of Sciences* **106,** 7143–7148.

Wyatt HL, Heng MK, Meerbaum S, Hestenes JD, Cobo JM, Davidson RM & Corday E (1979). Cross-sectional echocardiography. I. Analysis of mathematic models for quantifying mass of the left ventricle in dogs. *Circulation* **60,** 1104–1113.

Yancy CW et al. (2013). 2013 ACCF/AHA Guideline for the Management of Heart Failure. *Circulation* **128,** 240–327.

Yancy CW, Jessup M, Bozkurt B, Butler J, Casey DE, Colvin MM, Drazner MH, Filippatos GS, Fonarow GC, Givertz MM, Hollenberg SM, Lindenfeld J, Masoudi FA, McBride PE, Peterson PN, Stevenson LW & Westlake C (2017). 2017 ACC/AHA/HFSA Focused Update of the 2013 ACCF/AHA Guideline for the Management of Heart Failure. *J Am Coll Cardiol* **70,** 776–803.

Yancy CW, Lopatin M, Stevenson LW, de Marco T & Fonarow GC (2006). Clinical Presentation, Management, and In-Hospital Outcomes of Patients Admitted With Acute Decompensated Heart Failure With Preserved Systolic Function. *J Am Coll Cardiol* **47,** 76–84.

Yusuf S, Pfeffer MA, Swedberg K, Granger CB, Held P, McMurray JJ, Michelson EL, Olofsson B & Östergren J (2003). Effects of candesartan in patients with chronic heart failure and preserved left-ventricular ejection fraction: the CHARM-Preserved Trial. *The Lancet* **362,** 777–781.

Zhang J, Gong G, Ye Y, Guo T, Mansoor A, Hu Q, Ochiai K, Liu J, Wang X, Cheng Y, Iverson N, Lee J, From AHL, Ugurbil K & Bache RJ (2005). Nitric oxide regulation of myocardial O 2 consumption and HEP metabolism. *American Journal of Physiology-Heart and Circulatory Physiology* **288,** H310–H316.

Zile MR, Baicu CF & Gaasch WH (2004). Diastolic Heart Failure — Abnormalities in Active Relaxation and Passive Stiffness of the Left Ventricle. *New England Journal of Medicine* **350,** 1953–1959.